The Stochastic Laplacian Heaviside Method in Lattice QCD and its First Applications to Hadron Spectroscopy

by

Chik Him Wong

Submitted in partial fulfillment of the
requirements for the degree of
Doctor of Philosophy
at
Carnegie Mellon University
Department of Physics
Pittsburgh, Pennsylvania, USA

Advisor: Professor Colin Morningstar

August 26, 2011

Abstract

Currently, the best way to extract the low-energy predictions of quantum chromodynamics (QCD) is by estimating the QCD path integrals using the Monte Carlo method formulated on a space-time lattice. Determining the hadron mass spectrum is one of the major applications of such an approach. To study a particular state of interest, the energies of all states lying below that state must first be extracted, and many of the levels lying below the masses of the excited resonances are multi-hadron states. Reliably extracting multi-hadron energies is challenging since quark propagators that begin and end on the same final time-slice are essential. A novel method of estimating such quark propagators is proposed. This method, known as the 'stochastic Laplacian Heaviside' algorithm, combines Laplacian-Heaviside quark smearing with a new stochastic estimator of quark propagators. The method works well even in large spatial volumes. The implementation of the method is discussed in detail and its effectiveness is demonstrated in various systems, such as in determining the isovector and isoscalar meson energies, and calculating the energies of two-pion states. The inclusion of the scalar glueball is also studied.

Acknowledgements

I wish to express my sincerest appreciation to the following people. This work would not have been possible without their valuable input and advice, in both academic and personal aspects. I especially thank my supervisor, Colin Morningstar, as well as collaborators John Bulava, Justin Foley, Keisuke Jimmy Juge, Mike Peardon, David Richards, Balint Joo, and fellow graduate students David Lenkner and You-Chuan Jhang. In addition, I thank my family and friends for their endless support.

Contents

List of Tables

List of Figures

Chapter 1

Introduction

Quantum Chromodynamics (QCD) has been established as the gauge theory of the strong interactions. Being an important part of the Standard Model of particle physics, it describes the interactions among quarks and gluons as an SU(3) Yang-Mills theory with color-charged fermions. There are 6 flavors of quarks known so far, namely 'up' (u), 'down' (d), 'strange' (s), 'charm' (c), 'bottom' (b) and 'top' (t) in the order of increasing masses. Together with the gauge boson, gluons (g), they form composite particles known as hadrons. Only color-singlet hadrons have been observed experimentally. They are classified into two categories, baryons and mesons. Baryons have half-integral spins, while mesons have integral spin. Exotic mesons are currently of great interest. These hadrons have quantum numbers that cannot be obtained from a quark-antiquark pair with some orbital angular momentum. Hybrid hadrons are expected to exist. They are composed of constituent quarks and antiquarks bound by an excited gluon field. Exotic hadrons which are predominantly tetraquarks systems may also be found in nature, and bound states of gluons known as glueballs may be possible. There are candidates of the latter two categories but not confirmed yet.

QCD is a very successful theory in the sense that it has accumulated a lot of experimental support. Perturbative expansions in the gauge coupling at high energy ($q^2 \approx M_Z^2$) and chiral effective theories at low energy ($q^2 \approx m_\pi^2$) have successfully reproduced numerous experimental data. For example, the running of the QCD coupling $\alpha_s(\mu)$ with scale μ may be calculated perturbatively as well as measured experimentally for many different processes at different scales. Such comparison is thus a stringent test of our knowledge of perturbative QCD, as the behaviour of the running coupling depends specifically on many aspects of the QCD Lagrangian. These results

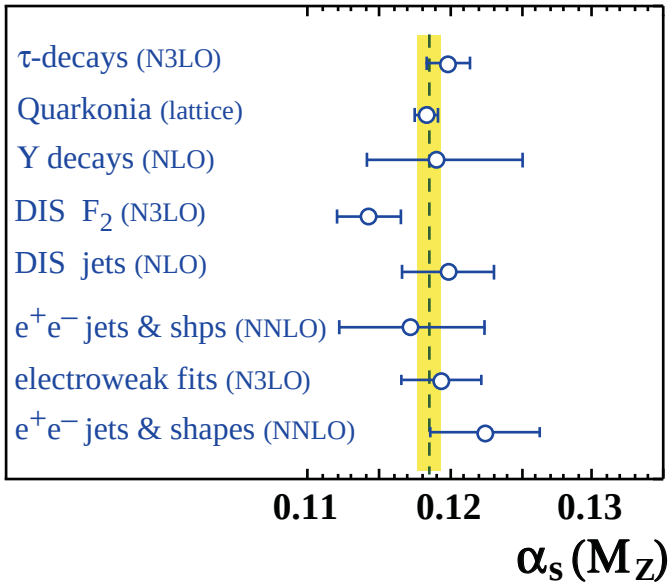

Figure 1.1: The value of the QCD coupling constant α_s at the scale $\mu = M_Z$ calculated from various experimental inputs at different scales. The error displayed here is the combined error from theoretical and experimental uncertainties. [1]

are shown in Fig. 1.1. Nearly all experimental data predict consistent values for $\alpha_s(M_Z)$, giving tremendous support to perturbative QCD. However, in the medium energy regime ($q^2 \approx \Lambda^2_{\rm QCD} \approx 1$ GeV^2), perturbative techniques are not applicable. In such a regime, the QCD coupling is too large to admit a perturbative solution, but the energy is high enough that many different hadrons can be created. The only first-principles, model-independent, non-perturbative approach to calculation in this regime is Lattice QCD, which computationally simulates the dynamics of the color gauge field and quark fields on Euclidean spacetime lattices.

One of the theoretical challenges of QCD in the medium energy regime is the calculation of the excited hadron spectra. Constituent quark models and chiral symmetry considerations can explain the properties of ground state hadrons reasonably well. However, agreement is less apparent for the description of excited states. Fig. 1.2 shows an isovector meson spectrum from one of our Lattice QCD simulations. It is presented in terms of lattice symmetry groups. The large shaded regions indicate multi-hadron thresholds. There are also exotic channels that cannot be explained by quark models. Information about these low-lying excited states and their properties may lead to the identification of the relevant degrees of freedom of medium energy

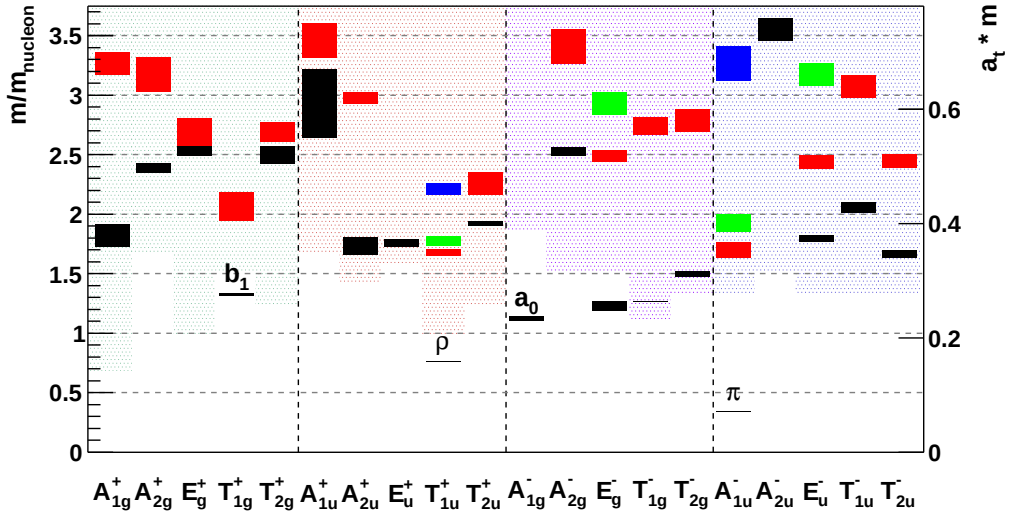

Figure 1.2: Isovector Meson Spectrum using 170 configurations of $\{24^3; 860\}$ ensemble in Table 2.4 (Refer to Ch. 2 for details of the ensemble). The energy levels shown are computed using single-hadron operators. The error estimations are statistical. The shaded regions indicate the multi-hadron thresholds. Within the shaded regions, the states are expected to be mostly multi-hadron in nature. Therefore single-hadron operators cannot capture these levels well. Multi-hadron operators will be included to extract the levels more reliably in future calculations.

QCD. Once these degrees of freedom are identified, perhaps a rigorous, systematically-improvable effective theory of medium energy QCD can be formulated. Lattice QCD is therefore in a position to contribute to these discussions by computing the single- and multi-hadron energies non-perturbatively. To do so, the masses of these excitations need not be determined to high precision, but the general pattern of excited states and their properties should be the goal of an exploratory calculation.

All Lattice QCD calculations are necessarily performed at finite lattice spacing, spatial volume, and temporal extent. While improved actions may be used to mitigate discretization errors, special attention must be paid to finite volume effects. Ch. 2 of this work discusses this in more detail. In finite volume with periodic boundary conditions, the spectrum of QCD consists of only discrete stationary states. The relationship of these finite-box states with infinite-volume scattering states and resonances has been studied in Ref. [2, 3]. For a sufficiently large volume, the mass of a narrow resonance is usually well approximated by its finite-volume mass, away from thresholds. Scattering states can usually be associated with finite-box stationary

states whose energies vary in inverse proportion to the volume.

Near a decay threshold, a resonance and its decay product states undergo significant mixing and their energies are somewhat distorted [2]. The resonance position and decay width may be extracted via a fit to the 'avoided level-crossing' behavior [4], which is demonstrated in Fig. 1.3 .

In Lattice QCD, finite box energies may be extracted from the temporal fall-off of correlation functions between suitable interpolating fields. In order to reliably extract resonance energies above decay thresholds, both single- and multi-hadron interpolators must be included. The evaluation of correlation functions containing these multi-hadron operators necessitates the calculation of the lattice quark propagator starting from all spatial sites on an initial time-slice t_0 to all spatial sites on a final time-slice t_1 , as spatial sums over the initial site are required to create single-hadron states with definite momenta to be combined into multi-hadron operators. More importantly, quark propagators that connect sites within the same time-slice are also required to evaluate correlation functions involving multi-hadron and isoscalars operators. Direct calculation of such quark propagators turns out to be computationally unfeasible, so alternative algorithms must be used. The algorithm developed in this work is called the Stochastic Laplacian Heaviside (Stochastic LapH) algorithm. It combines Laplacian Heaviside quark-field smearing [5] with stochastic estimations using 'dilution' variance reduction [6] to give a practical approach to compute all types of quark propagators, particularly same-time quark lines. Ch. 3 of this work discusses this algorithm and demonstrates its effectiveness.

In Ch. 4, some basic calculations are performed on realistic lattices as the first applications of the algorithm. The simulations mainly focus on mesons, $\rho - \pi\pi$ and two-pion systems. This is not only because these calculations involve a lot of same-time quark propagators at which the algorithm aims, but also these systems on their own play important roles in non-perturbative physical predictions of QCD.

The light isoscalar meson channel is particularly interesting and challenging to study. The ground state of the isoscalar scalar sector is known as σ or f_0. It is suspected to mix largely or entirely with a two-pion bound state. Therefore, multi-hadron operators are especially important in this channel. Isoscalar mesons can be constructed from quark-antiquark pairs of any flavor or even from states of pure gluons (glueballs). In general, the QCD eigenstates will be superpositions of all of these states. Experimentally, the GlueX collaboration [7, 8] aims at the discovery

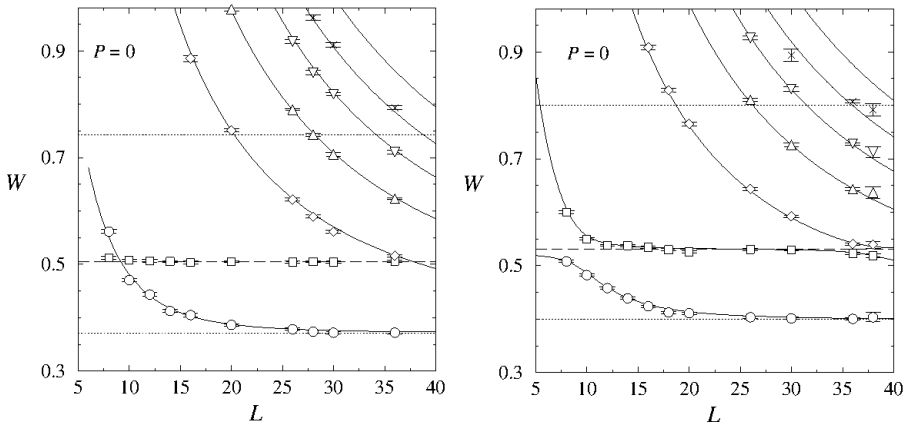

Figure 1.3: The avoided level-crossing behavior is illustrated. Calculations were perform in a ϕ^4 theory with two scalar fields (ϕ and ρ, with $m_\phi < m_\rho$) which interact via a three-point coupling, $\frac{g}{2}\rho\phi^2$. Energies of zero total momentum decay products and resonances are plotted for varying spatial box size. The horizontal dashed line is the resonance position (m_ρ), while the lower and upper dotted lines indicate $2m_\phi$ and $4m_\phi$, respectively. The boxes indicate the resonance (ρ) energies while the circles are the lowest two-ϕ states. Other symbols represent higher lying two-ϕ states. The left plot is the $g = 0$ case while the right is $g = 0.008$. The left plot shows the non-interacting case. Here the two-particle states follow the expected free-particle dispersion relation, while the resonance energy is constant as a function of box size. In the right plot, the interaction is turned on and free particle energies are distorted such that the energies of the lowest two-particle state and the resonance never intersect. The avoided level crossing is clearly visible on the right plot. Both resonance as well as multi-particle energies must be measured to map out the excitation spectrum in a finite box. [4]

of the spectrum of gluonic excitations, the largely unknown sector of the Standard Model of Particle Interactions. In order to fully decode such spectra, a good understanding of QCD predictions in the isoscalar channel spectra has to be obtained non-perturbatively. The QCD vacuum structure can also be studied via the lowest energy levels of isoscalar pseudoscalar channel, experimentally known as η and η', the masses of which are associated with the $U(1)$ problem [9] and the anomaly of the axial current.

The ρ meson is known to decay into two pions with a broad decay width. In finite volume, it is therefore expected to be largely mixed with a two-pion state. The ρ-$\pi\pi$ system is the easiest resonance to study and so, is one of the first applications of the Stochastic LapH method.

It is important to be able to treat the two-pion system well since it is involved in many channels. As mentioned above, the ground state of the isoscalar scalar channel is believed to couple heavily to an $I = 0$ bound state of two pions. A complete determination of ρ meson energy and decay width involves the $I = 1$ 4-point function of pions. Also the phase shift in the $I = 2$ channel pion scattering is one of the observables that can be compared with experimental data.

In Ch. 5, the summary of this work is given and an outlook into the future plans is presented. Much of the work presented here has already been published in Ref. [10] and is an extension of previous works in Refs. [5, 6, 11–21]. The use of interlaced time dilution to handle sink-to-sink quark lines in multi-hadron and isoscalar meson correlators is the main new contribution of this work.

Chapter 2

Lattice QCD

Lattice QCD [22] is a computation method in which QCD is regulated in a way that numerical evaluation is possible. It is done via the introduction of an ultraviolet cut-off arising from the discretization of spatial and temporal coordinates at lattice sizes a_μ. In other words, the maximum magnitude of (discrete) momentum allowed is $\sim \frac{1}{a}$. The discretized Lagrangian is therefore no longer invariant under the full Poincaré group of rotations, translations and boosts, but is invariant under the subgroup corresponding to the allowed rotations, translations and boosts on a hyper-cubic lattice. The discretization also produces artifacts that have to be fixed by introducing extra correction terms in the Lagrangian. It turns out that some more desired symmetries have to be broken explicitly to solve the so-called fermion doubling problem. It will be discussed in more detail in this section.

Lattice QCD is formulated in terms of imaginary time, which is analytically continued, or so-called Wick rotated, from Minkowski time. Since the fermion fields appear quadratically in the action, they can be integrated out exactly. This results in a path integral with a gauge field only. In imaginary time, the weighting function in such path integral is real and positive definite, allowing a probability interpretation. Hence Monte Carlo Integration with importance sampling can then be applied to evaluate quantities of interest. In this work the Metropolis-Hastings algorithm [23, 24] is used, in which an ensemble of gauge field configurations is obtained by updating along a Markov chain [25]. Since it is expensive to compute the determinant of the discretized Dirac Matrix coming from the fermion Grassmann integration, one has to come up with an efficient global updating algorithm. In this work, the RHMC algorithm [26], which is based on the HMC algorithm [27], is used (see later).

2.1 QCD Path Integrals

In the path integral formulation of quantum field theory, the vacuum expectation value of a functional F of operators O_i,i.e. $\langle F[O_0, O_1, O_2, \ldots, O_{\max}]\rangle$, is expressed as a sum over field configurations, each weighted by an exponential factor with the exponent being the action obtained from that configuration. In QCD, these fields are the N_f quark fields $\psi_f, f = u, d, s \ldots$ and the gluon field A_μ. Therefore a 2-point correlation function between operators O_i at time t and O_j at time t_0, $C_{ij}(t; t_0)$, can be expressed as

$$\begin{aligned} C_{ij}(t;t_0) =& \frac{\langle 0|O_i(t)\bar{O}_j(t_0)|0\rangle}{\langle 0|0\rangle} \\ =& \frac{\int D\psi D\bar{\psi} DA\ O_i[\psi,\bar{\psi},A](t)\bar{O}_j[\psi,\bar{\psi},A](t_0)\exp(iS_{\rm QCD}[\psi,\bar{\psi},A])}{\int D\psi D\bar{\psi} DA\ \exp(iS_{\rm QCD}[\psi,\bar{\psi},A])}, \end{aligned} \tag{2.1}$$

in which $S_{\rm QCD}$ is the QCD action in the continuum. In the continuum, such an integral is an infinite-dimensional functional integral. Regulating the theory by placing it on a spacetime lattice reduces it into one with finite number of dimensions. On a lattice, $S_{\rm QCD}$ has to be constructed to have terms that differ from $S_{\rm QCD}$ but diminish with powers of the lattice spacing a. Before discussing the explicit expression of the lattice action, Eq. 2.1 has to be transformed into a convenient form suitable for numerical computations, in addition to the discretization.

Local gauge invariance requires that the gluon field A_μ in the discretized version of Eq.2.1 is expressed by another quantity U_μ, the link variable [22], defined as follows:

$$\begin{aligned} [U_\mu]_{ab}(x) \equiv& \exp[\ ig\int_{\mathcal{C}} dx' A^m_\mu(x')T^m_{ab}\ ] \\ \approx& \exp[\ iga_\mu A^m_\mu(x+\frac{a_\mu}{2}\hat{\mu})T^m_{ab}\ ], \end{aligned} \tag{2.2}$$

in which T^m_{ab} are the 8 generators of SU(3) and $\mathcal{C}$ is a straight line connecting x and $x+a_\mu\hat{\mu}$. U themselves are also SU(3) matrices. To facilitate the Monte Carlo method that will be discussed in Sec. 2.3, the exponential factor has to be real and positive definite. This can be achieved by performing a Wick rotation that brings the theory

from Minkowski spacetime into Euclidean spacetime:

$$\begin{aligned} x_i^E &= x_i^M, i = 1, 2, 3, & x_4^E &= -ix_4^M \\ \gamma^4 &= \gamma_4 = \gamma_M^0 = \gamma_0^M, & \gamma_k &= \gamma^k = -i\gamma_M^k = i\gamma_k^M, \\ \{\gamma_\mu, \gamma_\nu\} &= 2\delta_{\mu\nu}, & \gamma_\mu^\dagger &= \gamma_\mu, \quad \gamma^5 = \gamma_5 = \gamma_4\gamma_1\gamma_2\gamma_3 = \gamma_M^5, \end{aligned} \tag{2.3}$$

in which x^E and x^M are Euclidean and Minkowski spacetime coordinates, and γ^μ and γ_M^μ are Euclidean and Minkowski Dirac-γ matrices, respectively. Now Eq. 2.1 becomes

$$\begin{aligned} C_{ij}(t; t_0) =& \frac{\langle 0|O_i(t)\bar{O}_j(t_0)|0\rangle}{\langle 0|0\rangle} \\ =& \frac{\int D\psi D\bar{\psi} DU \; O_i[\psi, \bar{\psi}, U](t)\bar{O}_j[\psi, \bar{\psi}, U](t_0) \exp(-S[\psi, \bar{\psi}, U])}{\int D\psi D\bar{\psi} DU \; \exp(-S[\psi, \bar{\psi}, U])}, \end{aligned} \tag{2.4}$$

where S is the Euclidean version of S_{QCD} expressed in terms of the link variables. If the Euclidean correlation functions obey reflection positivity, it can be shown [28] that they can be rotated back to their Minkowski spacetime counterparts. After the Wick rotation, the exponential factor is real and positive definite. Normalized by the denominator, it can be interpreted as a probability density. This fact becomes obvious if one notices the resemblance between the mathematical form of the Wick-rotated Eq. 2.4 with that of the expectation value of an 'observable' $O_i\bar{O}_j$, expressed in terms of Boltzmann factor e^{-S} and partition function $Z \equiv \int e^{-S}$ in the context of Statistical Mechanics. This feature is crucial for the application of the Monte Carlo algorithm.

The anti-commuting Grassmann-valued fermion fields ψ and $\bar{\psi}$ are integrated out before applying the Monte Carlo Method. To do this, the action S is split into two terms. The first one involves only U, while the other one can be expressed as a bilinear form of Grassmann-valued quark fields:

$$\begin{aligned} S[\psi, \bar{\psi}, U] &\equiv S_g[U] + S_f[\psi, \bar{\psi}, U] \\ S_f[\psi, \bar{\psi}, U] &\equiv \sum_{x,y} \bar{\psi}_{a\alpha}(x) M_{a\alpha|b\beta}[U](x, y)\psi_{b\beta}(y), \end{aligned} \tag{2.5}$$

in which S_g and S_f are the gauge action and fermion action respectively. Integrating

the fermion fields, Eq. 2.4 becomes

$$\begin{aligned} C_{ij}(t;t_0) =& \frac{\langle 0|O_i(t)\bar{O}_j(t_0)|0\rangle}{\langle 0|0\rangle} \\ =& \frac{\int DU\ \mathcal{F}[M^{-1}[U],U]\det M[U]\exp(-S[U])}{\int DU'\ \det M[U']\exp(-S[U'])}, \end{aligned} \tag{2.6}$$

in which $\mathcal{F}$ is the result of the Wick contraction of $O_i(t)$ and $\bar{O}_j(t_0)$. It is observed that the cost of getting rid of the fermion fields is the introduction of $\det M$ in the probability density and the occurrence of M^{-1} in the integrand. This determinant is non-local and computationally expensive. Moreover, one must ensure that the determinant is real and positive, otherwise the probability interpretation of the factor will become problematic and, as a result, Monte Carlo simulation will become non-applicable. It should be noted that although the above discussion was based on a 2-point correlation function, Eq. 2.6 is applicable to any quantities such as 3-point correlator, 4-point correlator or even the vacuum expectation value(VEV) of O, i.e. $\langle O\rangle \equiv \langle 0|\bar{O}|0\rangle$, by defining the corresponding $\mathcal{F}$'s that are in terms of M^{-1} after the Wick contractions of the fermion fields.

2.2 QCD Action Discretization

In the previous section, the discretized version of the Wick-rotated QCD action $\mathcal{S}_{\text{QCD}} \equiv \int d^4x\mathcal{L}_{\text{QCD}}$, $S \equiv \int d^4x\mathcal{L}$, was not yet defined. In the continuum, the QCD Lagrangian $\mathcal{L}_{QCD}$ is given by

$$\mathcal{L}_{\text{QCD}} = \frac{1}{4}F^a_{\mu\nu}(x)F^a_{\mu\nu}(x) + \sum_{f=1}^{N_f}\bar{\psi}^f_{a\alpha}(x)([D_\mu]_{ab}\gamma^\mu_{\alpha\beta} + m_f)\psi^f_{b\beta}(x), \tag{2.7}$$

in which

$$\begin{aligned} F^a_{\mu\nu}(x) &\equiv \partial_\mu A^a_\nu(x) - \partial_\nu A^a_\mu(x) + g f_{abc}A^b_\mu(x)A^c_\nu(x), \\ [D_\mu]_{ab} &\equiv \delta_{ab}\partial_\mu - igT^m_{ab}A^m_\mu(x), \end{aligned} \tag{2.8}$$

N_f is the number of quark flavors and m_f is the mass of the quark with flavor f. In the medium energy regime, c, b and t are not directly produced because their masses

are heavier than typical energy scales. Therefore in this work, only u, d and s are considered, i.e. $N_f = 2 + 1$. The masses of u and d are set to be identical so that isospin symmetry can be exploited.

It is tempting to naively discretize S_{QCD} into S by replacing partial differentials with finite differences without any further modifications. However it is known that such so-called 'Naïve Action' suffers from the problem of fermion doubling, in which additional low-lying fermionic degrees of freedom absent in the continuum arise on the lattice. This can be solved by introducing correction terms in the action that vanish in the continuum limit. However, according to the Nielson-Ninomiya theorem [29], it is not possible to remove this degeneracy while keeping Hermiticity, locality, lattice translational invariance and chiral symmetry at vanishing bare light quark mass. Therefore one has to choose an action that breaks at least one of those desirable symmetries on the lattice.

Although adding correction terms into the action cannot solve the doubling problem while keeping all desired symmetries, it is still possible to make use of this freedom to reduce the effects of lattice artifacts. Additional terms are added to the action via the Symanzik improvement procedure [30], stout-smearing [31] of the gauge links in the quark action and scaling of the gauge links by tadpole improvement factors [32]. During these procedures, the positivity of the lattice transfer matrix has to be maintained so that highly excited hadron states can still be extracted. [33] This would mean that the action should not contain terms that extend more than one time slice (the clover term is an exception). Therefore the Symanzik improvement procedures [30] are restricted not to produce such terms and only the spatial gauge links are stout-smeared.

Since the information carried by the correlation function will be extracted by analysing its temporal evolution, it is important to increase its temporal resolution and it would be desirable to further reduce the temporal artifacts while maintaining positivity. This can be achieved by simulating on an anisotropic lattice [33], in which the temporal lattice spacing a_t is smaller than the spatial directions $a_s \equiv \xi a_t$, $\xi > 1$ being the anisotropy parameter. The temporal lattice artifacts which are of orders of powers of a_t are suppressed because of the reduced a_t, while a higher temporal resolution also allows more accurate extraction of the temporal evolutionary behaviors of the correlation functions. In this work, $a_s \approx 0.12$ fm and $\xi \approx 3.5$.

2.2.1 The Quark Action

Because of the fermion doubling problem discussed before, there are many ways of discretizing the quark action. Several popular formulations are clover-Wilson [34], staggered [35–37], domain-wall [38,39] and overlap [40,41]. Each of them has different pros and cons. The list is still expanding nowadays. In this work, the clover-Wilson type is employed. The justification is the following.

The staggered formulation preserves chiral symmetry at finite lattice spacing, at the expense that the effect of the degeneracy due to fermion doubling remains, causing each fermion to have four degenerate partners. These extra 'tastes' impose difficulties on the extraction and identification of low-lying excited states. Moreover, the positivity of the transfer matrix is spoiled by the temporal non-locality in the staggered fermion action. Such violation causes oscillatory behavior in effective masses (defined in Sec. 2.5.1) at small temporal intervals, which further complicates the extraction of higher-lying excited states.

The domain-wall formulation introduces an additional spacetime dimension of length L_d. Although the chiral symmetry violation in this case is suppressed exponentially with L_d [38], the computational cost of this extra dimension is very significant. The positivity of the transfer matrix is also violated. Moreover, chiral symmetry is never restored exactly since any simulation must use a finite L_d. The overlap formulation tackles this issue by analytically integrating over an infinite L_d instead of direct simulation in that dimension, so that chirality is restored exactly at finite lattice spacing. The non-locality and the presence of a square root in the overlap Dirac operator which is computationally expensive in the resultant action is not preferred here compared with the Wilson one.

The clover-Wilson formulation gives all doubler states masses of an order of the inverse lattice spacing, so that they do not have any significant effects in the simulation at small lattice spacings. It is numerically demonstrated that the positivity in transfer matrix is not violated. Furthermore, recent algorithmic techniques [42] have greatly reduced the computational cost for this formulation. The main problem of using the Wilson-type fermion discretization is the broken chiral symmetry at finite lattice spacing. This, along with other lattice artifacts, can be systematically reduced by the Symanzik improvement [30] and by the use of stout links [31].

The Wilson formulation with clover improvement satisfies most of the needs of this work and is thus employed. The Wilson action S_f^W is composed of the 'Naïve'

action and the 'Wilson' term that lifts the masses of the doubler states:

$$S_f^W[\psi,\bar{\psi},U] \equiv \sum_{x,y} \bar{\psi}_{a\alpha}(x) \left[m_0 \delta_{ab}\delta_{\alpha\beta}\delta_{xy} + \frac{1}{u_t}\left([\gamma_t]_{\alpha\beta} [\nabla_t]_{ax|by} - \frac{1}{2} r_r a_t [\Delta_t]_{ax|by} \delta_{\alpha\beta} \right) \right. \tag{2.9}$$

$$\left. + \frac{1}{\nu \tilde{u}_s} \sum_k \left([\gamma_k]_{\alpha\beta} [\nabla_k]_{ax|by} - \frac{1}{2} r_s a_s [\Delta_k]_{ax|by} \delta_{\alpha\beta} \right) \right] \psi_{b\beta}(y),$$

$$[\nabla_\mu]_{ax|by} \equiv \frac{1}{2a_\mu} \left[[U_\mu]_{ab}(x) \delta_{x+\hat{\mu},y} - \left[U_\mu^\dagger\right]_{ab}(x-\hat{\mu}) \delta_{x-\hat{\mu},y} \right],$$

$$[\Delta_\mu]_{ax|by} \equiv \frac{1}{a_\mu^2} \left[[U_\mu]_{ab}(x) \delta_{x+\hat{\mu},y} + \left[U_\mu^\dagger\right]_{ab}(x-\hat{\mu}) \delta_{x-\hat{\mu},y} - 2\delta_{ab}\delta_{x,y} \right],$$

in which u_t is the temporal tadpole factor, $\tilde{u}_s$ is the tadpole factor for the smeared spatial links, ν is the fermion anisotropy parameter, r_t is the temporal Wilson parameter and r_s is the spatial Wilson parameter.

If $r_s = r_t = 1$ is imposed, the action can be shown to have the desirable property of reflection positivity. The lattice artifacts of order $\mathcal{O}(a_s, a_t)$ can be reduced by the introduction of correction terms via the Symanzik procedures [30]. At $\mathcal{O}(a_s)$, such procedure produces the 'clover' term:

$$S_f^C[\psi,\bar{\psi},U] \equiv \sum_{x,y} \bar{\psi}_{a\alpha}(x) \left[\frac{c_t a_s}{2\tilde{u}_s^2 u_t^2} \sum_k [\sigma_{tk}]_{\alpha\beta} [F_{tk}]_{ab} \delta_{xy} \right. \tag{2.10}$$

$$\left. + \frac{c_s a_s}{2\tilde{u}_s^4} \sum_{k<l} [\sigma_{kl}]_{\alpha\beta} [F_{kl}]_{ab}(x) \delta_{xy} \right] \psi_{b\beta}(y)$$

$$[F_{\mu\nu}]_{ab}(x) \equiv \frac{1}{8 i a_\mu a_\nu} \left[[L_{\mu\nu}]_{ab}(x) - [L_{\mu\nu}^\dagger]_{ab}(x) \right]$$

$$\begin{aligned}
[L_{\mu\nu}]_{ab}(x) \equiv\ & [U_\mu]_{ad}(x) [U_\nu]_{de}(x+\hat{\mu}) [U_\mu^\dagger]_{ef}(x+\hat{\nu}) [U_\nu^\dagger]_{fb}(x) \\
& + [U_\nu]_{ad}(x) [U_\mu^\dagger]_{de}(x-\hat{\mu}+\hat{\nu}) [U_\nu^\dagger]_{ef}(x-\hat{\mu}) [U_\mu]_{fb}(x-\hat{\mu}) \\
& + [U_\mu^\dagger]_{ad}(x-\hat{\mu}) [U_\nu^\dagger]_{de}(x-\hat{\mu}-\hat{\nu}) [U_\nu]_{fb}(x-\hat{\nu}) \\
& + [U_\nu^\dagger]_{ad}(x-\hat{\nu}) [U_\mu]_{de}(x-\hat{\nu}) [U_\nu]_{ef}(x+\hat{\mu}-\hat{\nu}) [U_\mu^\dagger]_{fb}(x),
\end{aligned}$$

in which c_t is the temporal clover coefficient, $\sigma_{\mu\nu} = \frac{1}{2i}[\gamma_\mu, \gamma_\nu]$. For simplicity, we use a definition of $F_{\mu\nu}$ which is not color traceless. The full fermion action we use is thus $S_f[\psi,\bar{\psi},U] \equiv S_f^W[\psi,\bar{\psi},U] + S_f^C[\psi,\bar{\psi},U]$. In this work, $c_s = 1$ and $c_t = \frac{1}{2}(1+\xi^{-1})$ according to tree-level lattice perturbation theory. These values are consistent with the

non-perturbative tuning of these parameters [43]. Although the reflection positivity of the clover-Wilson action has not been proven, we have numerically demonstrated positivity for the lattice spacings and quark masses that we use.

The spatial gauge links in S_f have been stout-smeared. A single iteration of stout-smearing transforms the link in this way:

$$\begin{aligned} U_\mu^{(n+1)}(x) &\equiv \exp\left(iQ_\mu^{(n)}(x)\right) U_\mu^{(n)}(x) \\ Q_\mu(x) &\equiv \frac{1}{2}(\Omega_\mu^\dagger(x) - \Omega_\mu(x)) - \frac{i}{6}\mathrm{Tr}(\Omega_\mu^\dagger(x) - \Omega_\mu(x)) \\ \Omega_\mu(x) &\equiv C_\mu(x)U_\mu^\dagger(x) \\ C_\mu(x) &\equiv \sum_{\nu\neq\mu} \rho_{\mu\nu}\left(U_\nu(x)U_\mu(x+\hat{\mu})U_\nu^\dagger(x+\hat{\mu}) + U_\nu^\dagger(x-\hat{\nu})U_\mu(x-\hat{\nu})U_\nu(x-\hat{\nu}+\hat{\mu})\right). \end{aligned} \tag{2.11}$$

In this work, two such iterations are employed with $\rho_{ij} \equiv \rho = 0.14$ and $\rho_{it} = 0$, i.e. the temporal links are not smeared to ensure positivity.

After these improvements, the leading discretization errors of S_f have become $\mathcal{O}(g^2a_s, g^2a_t, a_s^2, a_t^2)$.

2.2.2 The Gauge Action

We use the gauge action in Ref. [33] given by $S_g[U] = S_g^W[U] + S_g^{SZ}[U]$, where the plaquette term is

$$\begin{aligned} S_g^W[U] &\equiv \frac{5\beta}{3\xi_0 u_s^4}\Omega_s + \frac{4\beta\xi_0}{3u_s^2u_t^2}\Omega_t \\ \Omega_s &\equiv \sum_{x,i<j} 1 - P_{ij}(x) \\ \Omega_t &\equiv \sum_{x,i} 1 - P_{it}(x) \\ P_{\mu\nu}(x) &\equiv \frac{1}{3}\mathrm{Re\ Tr}\left[U_\mu(x)U_\nu(x+\hat{\mu})U_\mu^\dagger(x+\hat{\nu})U_\nu^\dagger(x)\right] \\ \beta &\equiv 2N_c/g^2, \end{aligned} \tag{2.12}$$

in which g is the gauge coupling and the correction term containing 2×1 rectangle is

$$
\begin{aligned}
S_g^{SZ}[U] &\equiv \frac{\beta}{12\xi_0 u_s^6}\Omega_s^R + \frac{\beta\xi_0}{12u_s^4 u_t^2}\Omega_t^R \\
\Omega_s^R &\equiv \sum_{x,i\neq j} 1 - R_{ij}(x) \\
\Omega_t^R &\equiv \sum_{x,i} 1 - R_{it}(x) \\
R_{\mu\nu}(x) &\equiv \frac{1}{3}\mathrm{Re\ Tr}[U_\mu(x)U_\mu(x+\hat{\mu})U_\nu(x+2\hat{\mu})U_\mu^\dagger(x+\hat{\mu}+\hat{\nu})U_\mu^\dagger(x+\hat{\nu})U_\nu^\dagger(x)].
\end{aligned}
\tag{2.13}
$$

The leading lattice artifacts of this action are $\mathcal{O}(a_t^2, g^2a_s^2, a_s^4)$ and the positivity is maintained by the temporal locality of S_g^{SZ}.

2.3 Monte Carlo Integration Methods

Equipped with the discretized actions, one is able to compute Eq. 2.6 numerically using Monte Carlo algorithms. Such algorithms exploit the fact that an integral $I \equiv \int dx f(x)p(x)$, in which the integrand can be expressed as a product of a positive definite function $p(x)$ and another function $f(x)$ of argument x, can be numerically evaluated by averaging $f(x)$ on a sufficiently large number N_{cfg} of x's sampled from the 'configuration' space $\mathscr{S}_{x|p}$ in which x follows the probability density $P(x)$ defined as the normalized $p(x)$, i.e.

$$
\begin{aligned}
\frac{I}{\int dx\ p(x)} &= \frac{\int dx\ f(x)p(x)}{\int dx\ p(x)} \\
&\equiv \int dx\ f(x)P(x) \\
&\approx \left[\frac{1}{N_{\mathrm{cfg}}}\sum_{i=0}^{N_{\mathrm{cfg}}-1} f(x_i)\right]_P \\
&= \mathrm{E}[f]_{\mathscr{S}_{x|p},N_{\mathrm{cfg}}}, \\
P(x) &\equiv \frac{p(x)}{\int dx\ p(x)}.
\end{aligned}
\tag{2.14}
$$

As mentioned in Sec. 2.1, Eq. 2.6 can be treated as an ensemble average of the observable $\mathcal{F}[M^{-1}[U], U]$ over configurations U in the same way, replacing the numbers

x with the links U :

$$\begin{aligned}
&\frac{\int DU\ \mathcal{F}[M^{-1}[U],U]\det M[U]\exp(-S[U])}{\int DU'\ \det M[U']\exp(-S[U'])} \\
\equiv&\int DU\ \mathcal{F}[M^{-1}[U],U]P[U] \\
\approx&\left[\frac{1}{N_{\text{cfg}}}\sum_{i=0}^{N_{\text{cfg}}-1}\mathcal{F}[M^{-1}[U^{(i)}],U^{(i)}]\right]_P \\
=&\mathrm{E}[\mathcal{F}]_{\mathscr{S}_{U|P},N_{\text{cfg}}}, \\
P[U]\equiv&\frac{\det M[U]\exp(-S[U])}{\int DU'\ \det M[U']\exp(-S[U'])}.
\end{aligned} \tag{2.15}$$

Due to the previous construction requirement that $\det M[U]$ must be real and positive definite, one can always make such a correspondence with well-behaved $P[U]$. $P[U]$ can be interpreted as a probability density only if such condition is satisfied. As a result, any kind of correlation function can be, in principle, numerically evaluated by sampling in a sufficiently large ensemble of U with probability density $P[U]$. In this way, the problem of computing the path integral is transformed into a problem of generating such an ensemble of U with the desired distribution and evaluation of the corresponding $\mathcal{F}[M^{-1}[U],U]$ on it.

It turns out that this process is a difficult task. In the case of a usual simple low-dimensional integral I in Eq. 2.14, the x ensemble can be generated by a simple transformation of uniformly generated random numbers into $P(x)$. However, it is not possible for an ensemble of complicated many-dimensional gluon field U with probability density $P[U]$ to be generated in the same way for Eq. 2.15. Thus, a Markov process [25] is employed instead. A Markov process is a stochastic process in which the current configuration is obtained from a random change of the previous one, resulting in a collection of configurations that are linked like a chain, the so-called Markov chain. If the chain is irreducible, aperiodic and ergodic, it can be shown (see, for example, Ref. [44]) that, in the limit of a long chain, the configurations approach a unique stationary distribution. The desired ensemble of U can therefore be generated by a Markov process that has $P[U]$ as the stationary distribution.

The simplest implementation of a Markov process with stationary distribution ρ is the Metropolis-Hasting algorithm [23, 24]. In this method, a change from the current configuration U into a new configuration U' is proposed according to an arbitrary

proposal probability density $R(U' \leftarrow U)$, which is not related to $P[U]$ in general. The proposed new configuration is then accepted according to the acceptance probability P_{acc} defined as follows:

$$P_{\text{acc}} \equiv \min\left(1, \frac{R(U \leftarrow U')P[U']}{R(U' \leftarrow U)P[U]}\right). \tag{2.16}$$

The above scheme would have been straightforward, if the computational cost were not an issue. It is known that $\det M$ in P is computationally too expensive to be evaluated directly for each U because of its huge dimensionality. Therefore one has to come up with a feasible way to evaluate it. $R(U' \leftarrow U)$ should also be chosen cleverly so that the correlation between configurations can be minimized, which implies an efficient way of exploring the configuration space, while keeping an acceptable acceptance rate so that computational resources are not wasted on proposing changes that keep being rejected. In this work, the RHMC (Rational Hybrid Monte Carlo) algorithm [26], which is an improved version of Metropolis algorithm, is employed.

2.3.1 The RHMC Algorithm

Before going into the details of RHMC algorithm, it would be useful to have an overview of the process first. It is illustrated in Fig. 2.1. The main process is still a Metropolis updating [23, 24], which produces the link $U^{(n)}$ at step n. Each new link is proposed by a process called Molecular Dynamics Evolution. Two additional ingredients are introduced. One is a set of scalar fields $\phi_l^{(l)}(x), \phi_h^{(l)}(x), \phi^{(s)}(x)$ calculated from corresponding pseudo-fermions $\eta_l^{(l)}(x), \eta_h^{(l)}(x), \eta^{(s)}(x)$ drawn from independent Gaussian $\eta^{(f)}$ distribution, which take care of the $\det M$ issue. The other is a fictitious 'momentum' π conjugate to $U^{(n)}$, which is drawn from a π distribution as well. These two fields, together with $U^{(n)}$, generates a new proposed link $U^{(n)\prime}$ by an algorithm called Molecular Dynamic Evolution, in which $U^{(n)}$ and π evolve into $U^{(n)\prime}$ and π' respectively as if U were a classical field with conjugate momentum π, which itself evolves according to $U^{(n)}$, ϕ and $S_g[U]$. This calculation is sped up by making use of tricks such as the Hasenbusch Preconditioning [45], Multiple Timescale Integration [46] and Deflation [47]. The newly proposed link is then dictated by the $(n+1)^{\text{th}}$ Metropolis step. U' becomes $U^{(n+1)}$ if it is accepted, otherwise the procedure goes on without changes. The process is then repeated. It should be noted that only

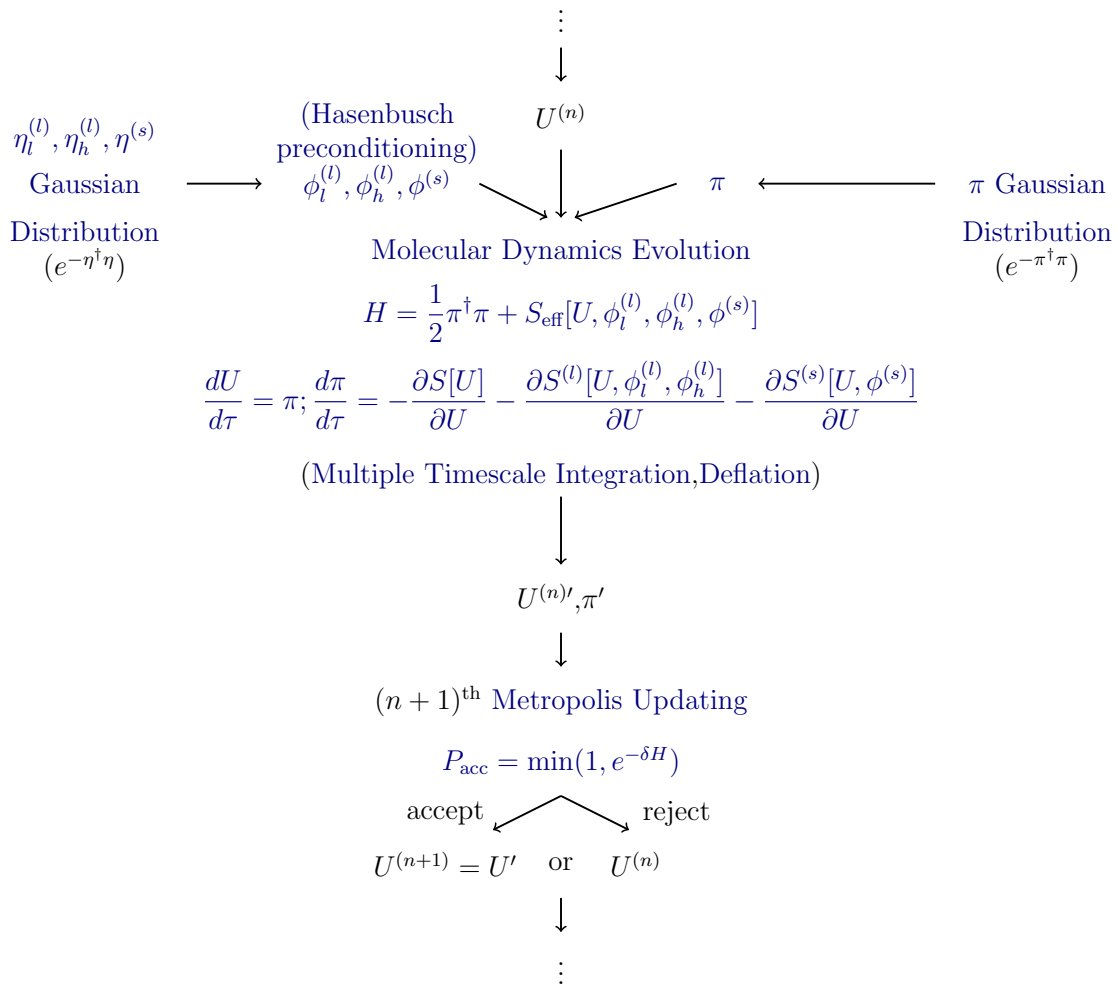

Figure 2.1: An overview of RHMC algorithm

U is iterated in this process, while π and ϕ are not. The details of these steps are depicted as follows.

Pseudo-Fermions

As mentioned before, it is computationally expensive to calculate the determinant of M in Eq. 2.15. To overcome this, a pseudo-fermion method is employed. In general, there are N_f factors of $\det M^{(f)}$ for N_f flavors with degenerate masses m_f. Due to the γ^5-hermiticity, $M = \gamma^5 M^\dagger \gamma^5$, $(\det M^{(f)})^{N_f} = \det(M^{(f)\dagger} M^{(f)})^{N_f/2}$. Moreover, it is known that

$$\det(M^{(f)\dagger} M^{(f)})^{N_f/2} \propto \int D\phi^{(f)} e^{-\phi^{(f)\dagger}(M^{(f)\dagger} M^{(f)})^{-N_f/2}\phi^{(f)}}, \tag{2.17}$$

for some complex non-Grassmann field $\phi^{(f)}(x)$, with an additional requirement that $\det M^{(f)} > 0$ if N_f is odd. Therefore one can trade the determinants with an additional term, a Gaussian functional of the 'pseudo-fermion' field $\phi^{(f)}$, in S. In this work, u and d quarks are treated as degenerate in 'bare' masses m_l, while s quark has a different heavier 'bare' mass m_s. (More details on the tuning of these parameters are available in Sec. 2.4). Therefore $N_l = 2$ for the light quarks and $N_s = 1$ for s quark. Since $M^{(s)}$ is supposed to be better conditioned due to the heavy mass m_s, $\det M^{(s)}$ is believed to be (practically) always positive. Therefore the effective action S_{eff} becomes

$$\begin{aligned} S_{\text{eff}}[U, \phi^{(f)}] &\equiv S[U] + \phi^{(l)\dagger}(M^{(l)\dagger}[U] M^{(l)}[U])^{-1}\phi^{(l)} + \phi^{(s)\dagger}(M^{(s)\dagger}[U] M^{(s)}[U])^{-1/2}\phi^{(s)} \\ &\equiv S[U] + S^{(l)}[U, \phi^{(l)}] + S^{(s)}[U, \phi^{(s)}]. \end{aligned} \tag{2.18}$$

If only $S^{(l)}[U, \phi^{(l)}]$ were taken into account in the Monte Carlo process, one only needs to draw random fields $\eta^{(l)}$ from a Gaussian distribution, obtain $\phi^{(l)} = M^{(l)\dagger}\eta^{(l)}$, use $S[U] + S^{(l)}[U, \phi^{(l)}]$ as the effective action and update $\eta^{(l)}$ for each Metropolis step. The whole U-updating algorithm that deals with such simpler situation is called Hybrid Monte Carlo (HMC) method. It becomes more complicated when $S^{(s)}[U, \phi^{(s)}]$ is also considered, due to the fact that $\phi^{(s)}$ is now $\phi^{(s)} = (M^{(s)\dagger} M^{(s)})^{\frac{1}{4}}\eta^{(s)}$. One way to

approximate $(M^{(s)\dagger}M^{(s)})^{\frac{1}{4}}$ is to approximate it with a sum of rational functions:

$$(M^{(s)\dagger}M^{(s)})^{\frac{1}{4}} \approx \alpha_0 I + \sum_k \frac{\alpha_k}{M^{(s)\dagger}M^{(s)} + \beta_k}, \tag{2.19}$$

in which α_k and β_k are constants generated by the Remez algorithm [48]. $(M^{(s)\dagger}M^{(s)} + \beta_k)^{-1}\eta$ can be computed simultaneously for all k by a multiple-shift conjugate gradient solver, and thus is not too computationally expensive. The HMC algorithm that includes s quarks in this way is called the RHMC (Rational Hybrid Monte Carlo) algorithm. An alternative is called PHMC(Polynomial Hybrid Monte Carlo) algorithm. However it is not as suitable for the purpose of this work because it is computationally more expensive and multiple-shift solvers are not applicable in it.

Molecular Dynamics Evolution

Since the computational cost of each Metropolis step is high, it is crucial to explore the configuration space efficiently, while keeping the correlation of U's between steps acceptably small and the acceptance rate reasonable. This can be achieved by making a clever choice in the proposal algorithm. Given the non-locality of $M^{-1}[U]$, it is obvious that a trivial local updating proposal algorithm is not feasible. The RHMC algorithm adopts a proposing method called Molecular Dynamics Evolution.

In this algorithm, a fictitious 'momentum' $[\pi_\mu]_{ab}(x)$ canonically conjugate to U is introduced, as if U were a classical field. It has to be introduced in a fashion that does not ruin the desired distribution. In other words, its distribution should be totally irrelevant to that of U or $\phi^{(f)}$, so that any physical quantities of interest do not depend on the distribution of π. It turns out that Eq. 2.17 has already provided a solution for such distribution. By setting $N_f = 2$ and substituting M with $\sqrt{2}$ times the identity, one obtains

$$2 \propto \int D\pi e^{-\frac{1}{2}\pi^\dagger\pi}. \tag{2.20}$$

Therefore, it is acceptable to introduce a π field which follows the Gaussian distribution. This, again, implies an additional term in S_{eff}, resulting in a 'Hamiltonian' H:

$$H[U, \phi^{(f)}] = \frac{1}{2}\pi^\dagger\pi + S_{\text{eff}}[U, \phi^{(f)}]. \tag{2.21}$$

It should be noted that such a 'Hamiltonian' is not at all a physical quantity. It

does not include the momenta of $\phi^{(f)}$ and U does not 'evolve' physically according to H nor π. However, H plays the same role as the Hamiltonian in the Boltzmann factor (at 'Temperature' $T = 1$) in the analogy made in Sec. 2.1 between Wick-rotated Path Integral formulation and Partition Function formulation of Statistical Mechanics. Since U is not physically 'evolving' along any parameter, there is no physical consequence of claiming π to be the canonical conjugate, i.e. canonical momentum, of U that 'evolve' in some artificial time τ. In this sense, H is really the Hamiltonian that governs such evolution in τ via classical equations of motion:

$$\begin{aligned}
\frac{dU}{d\tau} =& \{U, H\} = \frac{\partial H}{\partial \pi} = \pi \\
\frac{d\pi}{d\tau} =& \{\pi, H\} = -\frac{\partial H}{\partial U} = -\frac{\partial S_{\text{eff}}[U, \phi^{(f)}]}{\partial U} \\
=& -\frac{\partial S[U]}{\partial U} - \phi^{(l)\dagger} \left[\frac{\partial}{\partial U} (M^{(l)\dagger}[U] M^{(l)}[U])^{-1} \right] \phi^{(l)} \\
& - \phi^{(s)\dagger} \left[\frac{\partial}{\partial U} (M^{(s)\dagger}[U] M^{(s)}[U])^{-1} \right] \phi^{(s)}.
\end{aligned} \tag{2.22}$$

These equations are solved numerically using a symplectic (area-preserving) and reversible integration scheme with a finite step size $\delta\tau$. The scheme used in this work is the second order Omelyan integrator [49]. As a result, U and π 'evolve' into U' and π' after the amount of 'time' τ, but H is only approximately conserved due to the finiteness of $\delta\tau$. The difference $\delta H = H_{\text{new}} - H_{\text{old}}$ can be used in the Metropolis step. The proposed new link U' is then dictated in the Metropolis accept-reject step with the acceptance probability

$$P_{\text{acc}} = \min\left(1, e^{-\delta H}\right). \tag{2.23}$$

Effectively this 'evolution' plays the role of the proposal probability $R(U' \leftarrow U)$ that provides a U' that is globally updated from U. This algorithm ensures that δH is such that the acceptance probability is not small. As usual, U' becomes $U^{(n+1)}$ if accepted, otherwise the π and ϕ fields are redrawn without updating $U^{(n)}$. The process is repeated and the ensemble of U with desired distribution can then be obtained.

There are a few improvements in this evolution algorithm. They are discussed briefly below.

Hasenbusch Preconditioning [45]

It is noted that in Eq. 2.22, an expensive $(M^{(l)})^{-1}$ is required in order to solve it for each step of size $\delta\tau$. Therefore if one can use a larger $\delta\tau$, the number of such inversions can be reduced and performance can be improved. The size of $\delta\tau$ required to solve Eq. 2.22 at a certain level of accuracy and at a certain finite τ depends on the size of the 'force' term of the equations($\frac{d\pi}{d\tau}$). The smaller this term is, the larger $\delta\tau$ can be, and in turn the lower computational cost it requires. It is therefore desirable to reduce $\frac{\partial}{\partial U}(M^{(l)\dagger}[U]M^{(l)}[U])^{-1}$ in some way. It turns out the Hasenbusch Preconditioning techniques can improve this situation, at the expense of introducing yet another independent fictitious pseudo-fermion field $\phi_h^{(l)}$, which has a heavier 'mass' $m_h > m_l$. Since

$$\begin{aligned}\det(M^{(l)\dagger}M^{(l)}) &= \left(\frac{\det M^{(l)\dagger}M^{(l)}}{\det M_h^{(l)\dagger}M_h^{(l)}}\right)\det(M_h^{(l)\dagger}M_h^{(l)}) \\ &= \det\left(M^{(l)\dagger}M^{(l)}(M_h^{(l)\dagger}M_h^{(l)})^{-1}\right)\det(M_h^{(l)\dagger}M_h^{(l)}),\end{aligned} \tag{2.24}$$

in which $M_h^{(l)}$ represents the Dirac matrix of $\phi_h^{(l)}$, $S^{(l)}$ can now be split into two parts:

$$\begin{aligned}S^{(l)}[U,\phi_h^{(l)},\phi_l^{(l)}] &= S_l^{(l)}[U,\phi_l^{(l)}] + S_h^{(l)}[U,\phi_h^{(l)}] \\ S_l^{(l)}[U,\phi_l^{(l)}] &\equiv (\phi_l^{(l)\dagger}M_h^{(l)}[U])(M^{(l)\dagger}[U]M^{(l)}[U])^{-1}(M_h^{(l)\dagger}[U]\phi_l^{(l)}) \\ S_h^{(l)}[U,\phi_h^{(l)}] &\equiv \phi_h^{(l)\dagger}(M_h^{(l)}[U]M_h[U])^{-1}\phi_h^{(l)}.\end{aligned} \tag{2.25}$$

In this way, the fictitious 'force' term arising from the light quark is given by

$$\begin{aligned}\frac{\partial S^{(l)}[U,\phi_h^{(l)},\phi_l^{(l)}]}{\partial U} =& \phi_l^{(l)\dagger}\frac{\partial}{\partial U}\left[M_h^{(l)}[U](M^{(l)\dagger}[U]M^{(l)}[U])^{-1}M_h^{(l)\dagger}[U]\right]\phi_l^{(l)} \\ &+\phi_h^{(l)\dagger}\left[\frac{\partial}{\partial U}(M_h^{(l)\dagger}[U]M_h^{(l)}[U])^{-1}\right]\phi_h^{(l)}.\end{aligned} \tag{2.26}$$

Since the first term now consists of the derivative of a ratio between Dirac matrices of two similar masses with respect to U, this term tends to be smaller than the corresponding original 'force' term. This achieves the aim that the size of $\delta\tau$ can be increased. This is done at the cost of computing an additional inversion of $M_h^{(l)}$ in the second term. Therefore there are two competing requirements for the choice of m_h. It must be large enough so that $(M_h^{(l)})^{-1}$ is cheap to obtain, while m_h must also

be close enough to m_l so that the 'force' term is small enough.

Multiple Timescale Integration [46]

When there is an anisotropy in the lattice, i.e. $\xi \equiv a_s/a_t \neq 1$, the 'force' in the temporal direction is typically large due to the smallness of a_t. Instead of using a smaller $\delta\tau$ for the whole lattice, one may adopt an integration scheme of smaller $\delta\tau$ in the temporal direction than that in the spatial ones to save some computation of the spatial ones, resulting in a multiple timescale integration scheme.

Deflation [47]

As the mass of a quark decreases, its corresponding M becomes increasingly ill-conditioned. This requires more conjugate-gradient iterations to the inversion of M, resulting in an increased computational cost. The low-eigenmode deflation scheme is able to improve this scaling behavior. This scheme forms a Krylov subspace of M using the intermediate vectors generated by the conjugate-gradient algorithm. The low-lying modes can then be calculated using an Arnoldi-type iteration. Such deflated inversions do not significantly depend on quark masses, and therefore are considerably cheaper.

2.4 Scale Setting and Lagrangian Parameters

In order to interpret the lattice results in terms of physical units, it is essential to assign physical scales to quantities that define the lattice, such as lattice sizes, lattice spacings and pion masses. It is also necessary to tune the bare anisotropy parameters in the actions of gauge (ξ_0 in Eq. 2.12) and that of quarks (ν in Eq. 2.9) on the lattice to obtain the desired renormalized anisotropy ξ (which is 3.5 in this work). This is done as follows [43, 50].

The l and s quark masses, m_l and m_s respectively, are tuned using ratios of dimensionless quantities

$$\begin{aligned} l_\Omega &\equiv \frac{9m_\pi^2}{4m_\Omega^2} \\ s_\Omega &\equiv \frac{9(m_K^2 - m_\pi^2)}{4m_\Omega^2}, \end{aligned} \tag{2.27}$$

in which m_K,m_π and m_Ω are the masses of kaon, pion and omega baryon respectively. l_Ω and s_Ω are proportional to m_l and m_s in leading order in chiral effective theory. The bare s quark mass which corresponds to the physical value of s_Ω is found to be $m_s = -0.0743$. Since at present time, simulation at physical pion mass is still not reachable, the pion masses are chosen to be $m_\pi \approx 390$ MeV and $m_\pi \approx 240$ MeV, giving $m_l = -0.0840$ and $m_l = -0.0860$ respectively in this work. The spatial lattice spacing a_s is set by relating lattice m_Ω with the physical value, resulting in $a_s \approx 0.12$ fm.

The anisotropy is tuned non-perturbatively by varying bare parameters in the action to achieve the associated physical results. For the gauge anisotropy, ξ_0,the following Wilson loop ratios are considered

$$\begin{aligned} R_{ss}(x,y) &\equiv \frac{W_{ss}(x,y)}{W_{ss}(x+1,y)} \equiv e^{-a_s V_s(y a_s)} \\ R_{st}(x,t) &\equiv \frac{W_{st}(x,t)}{W_{st}(x+1,t)} \equiv e^{-a_s V_s(t a_t)} \\ W_{\mu\nu}(x_\mu, x_\nu) &\equiv \langle 0|\mathrm{Tr}\left[\sum_x U_\mu(x) U_\nu(x+x_\mu\hat{\mu}) U_{-\mu}(x+x_\mu\hat{\mu}+x_\nu\hat{\nu}) U_{-\nu}(x+x_\nu\hat{\nu})\right]|0\rangle. \end{aligned} \tag{2.28}$$

Imposing the condition $R_{ss}(x,y) = R_{st}(x,\xi y)$, $\xi = 3.5$ leads to $\xi_0 = 4.3$. The fermion anisotropy ν is obtained by requiring the dispersion relations of pseudoscalar and vector mesons to satisfy:

$$a_t^2 E^2(\vec{p}) = a_t^2 m^2 + \frac{1}{\xi^2} a_s^2 |\vec{p}|^2, \tag{2.29}$$

giving $\nu = 3.4$ for $\xi = 3.5$. It is observed that the anisotropy parameters weakly depend on the quark masses.

Table 2.4 shows the relevant lattices that are used in this work. The relevant parameters to specify them are the spatial lattice spacing a_s, spatial lattice size N_s, temporal lattice size N_t and bare light quark mass $m_u = m_d = m_l$. All other parameters are common in all the lattices, with values specified in the previous paragraphs. These lattices are referred to using the labels assigned in the table throughout this work.

Label	m_l	Lattice Size($N_s^3 \times N_t$)
$\{12^3; 743\}$	-0.0743	$12^3 \times 96$
$\{16^3; 840\}$	-0.0840	$16^3 \times 128$
$\{20^3; 840\}$	-0.0840	$20^3 \times 128$
$\{24^3; 840\}$	-0.0840	$24^3 \times 128$
$\{24^3; 860\}$	-0.0860	$24^3 \times 128$
$\{32^3; 860\}$	-0.0860	$32^3 \times 256$

Table 2.1: Relevant lattices used in this work

2.5 Data Analysis Methods

There are three main stages in the simulations of Lattice QCD. An ensemble of gauge configurations has to be first generated. The process used is described in Sec. 2.3.1. The second stage is to obtain the observables from the ensemble, which will be discussed in Ch. 3. The third stage is to extract the physics of interest. In this work, the energy levels are the physical quantities to be extracted.

2.5.1 Extraction of Excited-State Energies

Correlator Matrix

The purpose of simulating QCD on a lattice is to compute quantities that can only be obtained non-perturbatively from the theory. The hadron spectrum is one of such quantities. The energies of the hadrons can be extracted from the temporal correlators computed on the lattice. In principle, one can perform a spectral decomposition of the correlator $C(t)$ of a particular operator O onto normalized energy eigenstates $|n\rangle$ with energies E_n to fit individual energy levels:

$$C(t) \equiv \langle 0|O(t_0+t)\bar{O}(t_0)|0\rangle = \sum_n \langle O|n\rangle\langle n|O\rangle e^{-E_n t}, \tag{2.30}$$

in which $|O\rangle \equiv \bar{O}|0\rangle$ and $t > 0$. However, in practice, the signal is dominated by the slowest decaying exponential. Therefore it would be too noisy to extract the energy levels above ground level using a single operator. To solve this, a correlator matrix C_{ij} is constructed from N_{op} operators $\{O_i\}$ instead:

$$C_{ij}(t) \equiv \langle 0|O_i(t_0+t)\bar{O}_j(t_0)|0\rangle. \tag{2.31}$$

Then C_{ij} is rotated in a way that it is diagonalized at a particular chosen time $t = t_*$ into C'_{ij}:

$$\begin{aligned} C'_{ij}(t) &= \langle 0|\Omega_i(t_0+t)\bar{\Omega}_j(t_0)|0\rangle \\ C'_{ij}(t_*) &= \delta_{ij}\langle 0|\Omega_i(t_0+t_*)\bar{\Omega}_j(t_0)|0\rangle, \end{aligned} \tag{2.32}$$

in which Ω's are the transformed O's via the eigenvectors of C_{ij}. In the limit of $N_{\text{op}} \to N_E$, N_E being the maximum number of energy states allowed on the lattice,

C'_{ij} will stay diagonalized for all time after t_*, since each of the diagonal elements C'_{ii} represents the correlator of a single energy eigenstate $|\Omega_i\rangle \propto |n_i\rangle$. In the usual scenario, $N_{\text{op}} \ll N_E$. Thus $|\Omega_i\rangle$ can only be an approximation of $|n_i\rangle$ due to the contamination of other energy eigenstates. As a result, $|\Omega_i\rangle$ itself evolves slowly with time after t_*, destroying the diagonalization of C'_{ij} at later time-slices. It can indeed be shown that under certain conditions, the leading order correction to the dominance of $|n_i\rangle$ is given by $e^{-(E_{N_{\text{op}}+1}-E_i)t}$. Nonetheless, the dominance of $|n_i\rangle$ for a certain range of t is all one needs to fit it to a single exponential, since the signals will be overwhelmed by the noises at later time anyways. A useful way to figure out the range of time that C'_{ij} is diagonal is to define a normalized rotated correlator matrix:

$$\tilde{C}'_{ij}(t) \equiv \frac{C'_{ij}(t)}{\sqrt{C'_{ii}(t)C'_{jj}(t)}} \tag{2.33}$$

and deduce the range from its temporal evolution plot.

Effective mass m_{eff}

How well a correlator $C(t)$ of a certain operator O is approximated by a single exponential can be visually estimated by examining its effective mass $m_{\text{eff}}(t)$, which is a function of t:

$$a_t m_{\text{eff}}(t) \equiv \frac{1}{\delta t} \ln \left[\frac{C(t)}{C(t+\delta t)} \right], \tag{2.34}$$

in which δt is some time step which is taken to be $3a_t$ in this work, to reduce the effects of uncorrelated temporally-local fluctuations resulting from the algorithm that will be discussed in Ch. 3. It is trivial from the expression that m_{eff} would have been a constant, the energy of $|O\rangle$, if it were really an energy eigenstate. Since it is actually not, m_{eff} will only decrease from a large value and approach the lowest energy $|O\rangle$ overlaps with at later time-slices, when the excited states 'die out'. Therefore by looking at the size of the range of time where m_{eff} plateaus, one can tell how well $|O\rangle$ approximates the energy state it corresponds to.

Since all simulations are done in periodic finite-sized lattices, $C(t)$ is indeed a combination of the correlators of the particle that propagates from t_0 to $t_0 + t$ and its antiparticle that travels from t_0 to $t_0 + t$, while the latter is equivalent to the particle that travels backward from $t_0 + t$ to t_0,or forward from $t_0 + t$ to $t_0 + N_t$

due to periodic boundary conditioned lattice. By temporal translational invariance of the correlator, this extra piece is the same as the particle propagator from t_0 to $t_0 + (N_t - t)$. Therefore the actual form of $C(t)$ at large t should be

$$C(t) \sim e^{-m_{\text{eff}}t} + e^{-m_{\text{eff}}(N_t - t)}, \tag{2.35}$$

in which the definition of m_{eff} is now modified to be the solution of

$$C(t)\cosh\left(m_{\text{eff}}(\frac{N_t}{2} - t - \delta t)a_t\right) = C(t+\delta t)\cosh\left(m_{\text{eff}}(\frac{N_t}{2} - t)a_t\right). \tag{2.36}$$

Since in the limit $N_t \to \infty$ this wrap-around effect diminishes, in most of the cases this definition yields practically identical result as Eq. 2.34. However, it is necessary to include this lattice artifact if the lattice is small or the particle under consideration has a small mass.

t_{min} Plots

A way to demonstrate how well a fitting value of energy estimates the true energy is to use t_{min} plots. A t_{min} plot such as Fig. 4.1(c) shows the fitted mass m_{fit} in a range of time separation t with fixed maximum value t_{max}. In other words, it is a function of minimum value t_{min}. The hollow symbols represent the fit ranges with bad quality and the solid ones represent the fit ranges with good quality. A valid fit value should acquire a stable value with good quality over a range of t_{min}, i.e. insensitive to t_{min}. The fit values are expected to be valid if the asserted fit form is correct. For single hadrons, a cosh form is a valid fit form. In general, the fit form is different from cosh for multi-hadron correlation functions due to the interaction between wrapped-around particles and non-wrapped-around particles.

Correlators with Vacuum Expectation Values (VEV)

In general, $|O\rangle$ has a non-zero projection back to the vacuum $|0\rangle$ if $|O\rangle$ attains the same values of the quantum numbers as vacuum. For single hadron operators, all isoscalar scalar mesons(σ's) at rest in the lab frame have this property. For multi-hadron operators, any combinations with isospin $I = 0$, angular momenta $J = 0$ and total momenta $\vec{P} = \vec{0}$ have such property as well. This mixing with vacuum results

in a non-zero constant in Eq. 2.30 :

$$\begin{aligned} C(t) \equiv \langle 0|O(t_0+t)\bar{O}(t_0)|0\rangle &= \sum_n \langle O|n\rangle\langle n|O\rangle e^{-E_n t} \\ &= \sum_{n\neq 0} \langle O|n\rangle\langle n|O\rangle e^{-E_n t} + \langle 0|O|0\rangle\langle 0|\bar{O}|0\rangle \\ &= \sum_{n\neq 0} \langle O|n\rangle\langle n|O\rangle e^{-E_n t} + |\langle O\rangle|^2 \\ &\equiv \hat{C}(t) + |\langle O\rangle|^2, \end{aligned} \tag{2.37}$$

assuming $E_0 = 0$. Since $E_0 = 0$, $\langle O\rangle$ is identical for all time-slices within statistical fluctuations. This extra VEV term $|\langle O\rangle|^2$ is undesirable, because $C(t)$ approaches at late time-slices to the vacuum state with $E_0 = 0$, which is usually not of interest in spectroscopy or other contexts. In other words, only $\hat{C}(t)$ is the part of the correlator of interest. This part of the correlator is equivalent to a redefinition of O:

$$\begin{aligned} \hat{C}(t) &= \langle 0|O(t_0+t)\bar{O}(t_0)|0\rangle - |\langle O\rangle|^2 \\ &= \langle 0|\left[O(t_0+t) - \langle O\rangle\right]\left[\bar{O}(t_0) - \langle\bar{O}\rangle\right]|0\rangle \\ &\equiv \langle 0|\hat{O}(t_0+t)\bar{\hat{O}}(t_0)|0\rangle, \\ \hat{O}(t) &\equiv O(t) - \langle O\rangle. \end{aligned} \tag{2.38}$$

Therefore replacing O with $\hat{O}$ in all the equations derived in the previous section gives the physically interesting quantities. In this situation, there is an additional requirement of subtracting the VEV term from $C(t)$ after each calculation. In the rest of this work, all correlators $C(t)$ refer to the VEV-subtracted correlators unless otherwise is specified.

2.5.2 Error Estimations

In any stochastic calculations, it is always important to estimate the statistical error. Given that there are vacuum expectation values involved in the definition of the correlators in general and that effective masses are functions of the mean of the correlators, it is impossible to estimate the errors by plugging the data into common autocorrelation formulas. Moreover, the correlation between successive configurations along the Markov chain is significant enough to be taken into account. Although

this can be reduced by only sampling configurations separated by a certain number of steps, it is still necessary to have a measure to estimate how significant such correlation is, in order to determine the size of separation and to make claims about the independence of configurations within the resulting ensemble. On the other hand, correlation arises between time-slices in the same configuration when averaging source times t_0 as well. In order to handle all these appropriately, the error analysis thus has to be done through resampling techniques, such as the jackknife method and the bootstrap method [51]. They will be discussed in the following parts, keeping the VEV subtraction explicit to illustrate the ideas.

Jackknife Method

Given a collection of non-VEV-subtracted correlators $C[U](t)$ and their corresponding VEV, $V[U] \equiv \langle O[U] \rangle$, on an ensemble of U of size N_{cfg}, i.e.

$$\mathscr{C} = \{\{C[U^{(r)}](t), V[U^{(r)}]\}, r = 0, 1, \cdots, N_{\text{cfg}} - 1\}, \tag{2.39}$$

a 'Jackknife ensemble' $\mathscr{C}_{\text{Jac}} = \{\{C^{(r)}_{\text{Jac}}(t), V^{(r)}_{\text{Jac}}\}, r = 0, 1, \cdots, N_{\text{cfg}} - 1\}$ can be constructed as follows:

$$\begin{aligned} C^{(r)}_{\text{Jac}}(t) &\equiv \frac{1}{N_{\text{cfg}} - 1} \sum_{r'=0, r' \neq r}^{N_{\text{cfg}}-1} C[U^{(r')}](t), r = 0, 1, \cdots, N_{\text{cfg}} - 1 \\ V^{(r)}_{\text{Jac}} &\equiv \frac{1}{N_{\text{cfg}} - 1} \sum_{r'=0, r' \neq r}^{N_{\text{cfg}}-1} V[U^{(r')}], r = 0, 1, \cdots, N_{\text{cfg}} - 1. \end{aligned} \tag{2.40}$$

For any quantity f in terms of $C[U](t)$ and $V[U]$, such as $\hat{C}(t)$ or $m_{\text{eff}}(t)$, it can be evaluated on either $\mathscr{C}$ or $\mathscr{C}_{\text{Jac}}$, giving respectively collections of f's $\mathscr{F} = \{f[C, V], \{C, V\} \in \mathscr{C}\}$ and $\mathscr{F}_{\text{Jac}} = \{f[C_{\text{Jac}}, V_{\text{Jac}}], \{C_{\text{Jac}}, V_{\text{Jac}}\} \in \mathscr{C}_{\text{Jac}}\}$. The variance of f can then be found by

$$\begin{aligned} \sigma^2_{\text{Jac}}[f] &= \frac{N_{\text{cfg}}}{N_{\text{cfg}} - 1} \sum_{r=0}^{N_{\text{cfg}}-1} (f[C^{(r)}_{\text{Jac}}, V^{(r)}_{\text{Jac}}] - \langle f \rangle_{\mathscr{C}})^2, \\ \langle f \rangle_{\mathscr{C}} &\equiv \frac{1}{N_{\text{cfg}}} \sum_{r=0}^{N_{\text{cfg}}-1} f[C[U^{(r)}](t), V[U^{(r)}]]. \end{aligned} \tag{2.41}$$

Note that the mean of f is the one taken in the original ensemble. It can be shown that if f does not depend on V's, $\sigma^2_{\rm Jac}[f]$ coincides with the standard expression of a usual variance obtained from Central Limit Theorem. Although the jackknife method is easy to implement and clear in concepts, it has its limitations. It is based on the assumption that the U's in the ensemble are independent from one another. If the U's are correlated to one another, $\sigma^2_{\rm Jac}$ underestimates the true variance. This can be avoided by rebinning $\mathscr{C}$. [52] One can construct a new collection of C's and V's, $\mathscr{C}_b$, based on the original one:

$$C_b(t)^{(r)} \equiv \frac{1}{b}\sum_{r'=rb}^{(r+1)b-1} C[U^{(r')}](t), r = 0, 1, \cdots, N_{\rm cfg}/b - 1 \tag{2.42}$$
$$V_b^{(r)} \equiv \frac{1}{b}\sum_{r'=rb}^{(r+1)b-1} V[U^{(r')}], r = 0, 1, \cdots, N_{\rm cfg}/b - 1,$$

in which b is some integer that governs the degree of rebinning (and preferably a factor of $N_{\rm cfg}$). It can be shown that the mean of f on $\mathscr{C}_b$ remains the same as the original ensemble, while its variance would be significantly larger than the original one if the original ensemble contains correlated elements. Therefore the independence of U's (and the corresponding f's) can be examined by varying b and looking for a range in which the variance remains unchanged within statistical fluctuations. The variance found in this range is the uncorrelated estimate of the variance of f.

Bootstrap Method

An alternative method of error estimation is the bootstrap method. This method is very similar to the jackknife method, but it resamples the ensemble randomly with replacement:

$$C^{(r)}_{\rm Boo}(t) \equiv \frac{1}{N_{\rm cfg}}\sum_{s=0}^{N_{\rm cfg}-1} C[U^{m_{r,s}}](t), r = 0, 1, \cdots, N_{Boo} - 1 \tag{2.43}$$
$$V^{(r)}_{\rm Boo} \equiv \frac{1}{N_{\rm cfg}}\sum_{s=0}^{N_{\rm cfg}-1} V[U^{m_{r,s}}], r = 0, 1, \cdots, N_{Boo} - 1$$

in which $m_{r,s}$ is a random integer in the range of $[0, 1, \cdots, N_{\rm cfg} - 1]$. Since repeated use of U's is allowed, the resampled set can be of any size $N_{\rm Boo}$. The variance can

then be computed as follows:

$$\sigma^2_{\rm Boo}[f] \equiv \frac{1}{N_{\rm Boo}} \sum_{r=0}^{N_{\rm Boo}-1} (f[C^{(r)}_{\rm Boo}, V^{(r)}_{\rm Boo}] - \langle f \rangle_{\mathscr{C}})^2. \tag{2.44}$$

In this work, Jackknife method is used for most quantities but bootstrap method is used for fitted values of the particle masses.

Chapter 3

Methodology

In Ch. 2, the lattice formulation of QCD was presented. The algorithms of numerically generating the link variables and the analysis methods were introduced. In this chapter, the methodology of obtaining the required N-point correlation functions from gauge ensembles is discussed.

3.1 Field Smearing Schemes

The use of smeared fields is crucial for successfully extracting the spectrum of QCD in Monte Carlo computations. Hadron operators constructed out of smeared fields dramatically reduce the mixing with the highly excited states of the theory that obscure extraction of the low-lying energy eigenstates of interest. In this work, the operators are constructed using spatially-smoothed link variables $\tilde{U}_j(x)$ and spatially smeared quark fields $\tilde{\psi}(x)$.

3.1.1 Stout Link Smearing

Stout smearing [31] is employed as the smearing of the links $U_\mu(x)$. It is achieved via the weighted sum of 'staple' terms Σ_μ defined as follows:

$$\Sigma_\mu[U] = \sum_{\nu \neq \mu} \rho_{\mu\nu}[U_\nu(x)U_\mu(x+\hat{\nu})U_\nu^\dagger(x+\hat{\mu}) + U_\nu^\dagger(x-\hat{\nu})U_\mu(x-\hat{\nu})U_\nu(x-\hat{\nu}+\hat{\mu})], \quad (3.1)$$

in which $\rho_{\mu\nu}$ is some weighting factor. Since the temporal behavior of the correlators is crucial in energy level extractions, only spatial staples are used in the link

smoothening and temporal link variables are not smeared. For simplicity, the non-vanishing weighting factors are taken to be identical, with the value $\rho = 0.10$. In other words,

$$\rho_{ij} = \rho,\ \rho_{\mu 4} = \rho_{4\mu} = 0. \tag{3.2}$$

The links $U_\mu(x)$ are smeared iteratively by:

$$U_\mu^{(n+1)}(x) \equiv e^{iQ_\mu^{(n)}(x)} U_\mu^{(n)}(x), \tag{3.3}$$

in which

$$Q_\mu^{(n)}(x) \equiv \frac{i}{2}\left(\left(\Omega_\mu^{(n)}\right)^\dagger(x) - \Omega_\mu^{(n)}(x)\right) - \frac{i}{2N}\mathrm{Tr}\left(\left(\Omega_\mu^{(n)}\right)^\dagger(x) - \Omega_\mu^{(n)}(x)\right), \tag{3.4}$$

$$\Omega_\mu^{(n)}(x) \equiv \Sigma_\mu[U^{(n)}]U_\mu^{(n)\dagger}(\text{no sum over } \mu), \tag{3.5}$$

where (n) indicates the n^{th} iteration. Therefore the smeared link $\tilde{U_\mu}$ is defined as

$$\tilde{U}_\mu = U_\mu^{(n_\rho)}, \tag{3.6}$$

where the maximum number of iteration $n_\rho = 10$ in this work.

3.1.2 Laplacian Heaviside (LapH) Quark Smearing

The quark field of flavor A is smeared using

$$\tilde{\psi}_{a\alpha}^A(x) = S_{ab}(x,y)\psi_{b\alpha}^A(y), \tag{3.7}$$

in which x,y are lattice sites, a,b are color indices, α is a Dirac spin component, and the smearing kernel S is defined such that the smeared field behaves in exactly the same way as the original field under all time-independent symmetry transforms on a cubic lattice. Like the link smearing, only spatial smearing is adopted. In other words, $S_{ab}(x,y) \propto \delta_{x_4 y_4}$. In addition, S is independent of spin and flavor. The smearing scheme used in this work is called Laplacian Heaviside (LapH) quark-field smearing scheme. In such scheme, S is defined as

$$S \equiv \Theta\left(\sigma_S^2 + \tilde{\Delta}\right), \tag{3.8}$$

in which σ_S is the smearing cutoff parameter and $\tilde{\Delta}$ is the three-dimensional gauge-covariant Laplacian operator given by:

$$\tilde{\Delta}^{ab}(x,y;U) \equiv \sum_{k=1}^{3} \left\{ \tilde{U}_k^{ab}(x)\delta(y,x+\hat{k}) + [\tilde{U}_k^{\dagger}(y)]^{ab}\delta(y,x-\hat{k}) - 2\delta(x,y)\delta^{ab} \right\}, \quad (3.9)$$

in which x, y are lattice sites and a, b are color indices. $\tilde{\Delta}$ is a Hermitian matrix block-diagonal in time. The stout-smeared gauge links are used since it can drastically reduce the statistical error in the correlators of the hadron operators that involve covariantly-displaced quark fields, which will be discussed in Sec. 3.2. A gauge-covariant Laplacian operator is desired for smearing the quark field since it is one of the simplest operators that locally averages the field in such a way that preserves all relevant symmetry transformation properties of the original field.

The eigenvectors of $\tilde{\Delta}$ form a unitary matrix V_Δ that diagonalizes $\tilde{\Delta}$,

$$\tilde{\Delta} = V_\Delta \Lambda_\Delta V_\Delta^{\dagger}, \quad (3.10)$$

in which all eigenvalues in the diagonalized matrix Λ_Δ are real and negative. Therefore,

$$S = V_\Delta \Theta\left(\sigma_S^2 + \Lambda_\Delta\right) V_\Delta^{\dagger}. \quad (3.11)$$

The Heaviside function Θ eliminates all eigenvalues with magnitudes larger than σ_S^2. Since $\tilde{\Delta}$ is block-diagonal in x_4, one can associate each eigenpair with a corresponding time value. It is observed that among different time-slices, the numbers of eigenpairs that survive the Θ filter, N_v's, are approximately the same. It is also found that this value is not dependent significantly on pion masses. Fig. 3.1 shows the calculation based on $16^3 \times 128$ $N_f = 2+1$ lattices. It is observed that the eigenvalues do not differ significantly between pion masses ~ 0.64 GeV and ~ 0.39 GeV. In other words, S can be safely approximated by

$$S \approx V_S V_S^{\dagger}, \quad (3.12)$$

in which V_S is the unitary matrix constructed by the N_v eigenvectors for each time-slice. On a lattice with temporal size N_t, spatial size N_s and number of colors $N_c = 3$, the $N_v N_t$ eigenvectors, each having $N_t N_s^3 N_c$ components, span the so-called LapH subspace.

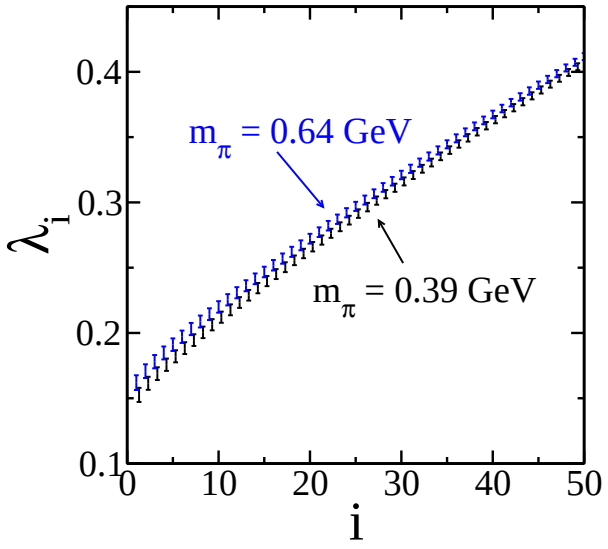

Figure 3.1: The small effect of the pion mass on the eigenvalues of the gauge-covariant Laplacian operator demonstrated on $16^3 \times 128$ $N_f = 2+1$ lattices. λ_i is the i^{th} lowest eigenvalue of $-\tilde{\Delta}$ on a given time-slice. The error bars correspond to the variation over different time-slices. [10]

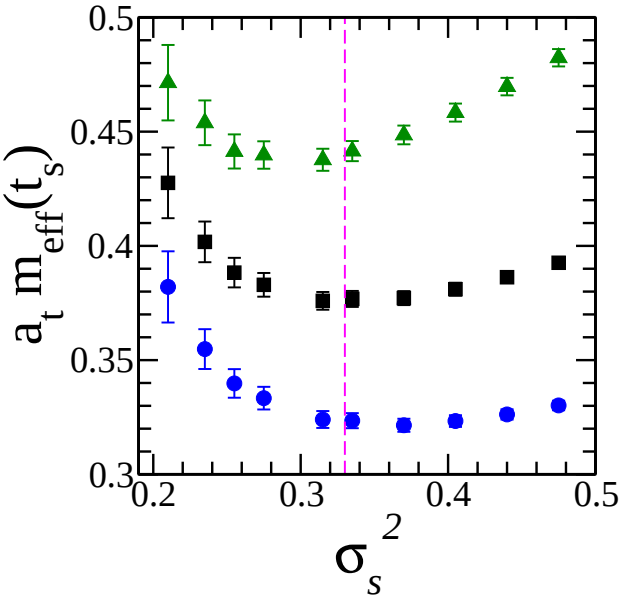

Figure 3.2: The m_{eff} for three representative nucleon operators against the LapH smearing cutoff σ_S^2 on $\{16^3; 840\}$ ensemble. The circles show results (shifted downward by 0.04) for a single-site operator. The squares correspond to a singly-displaced nucleon operator, and the triangles are the results (shifted upward by 0.04) for a triply-displaced-T operator [10]

The value of σ_S, and hence N_v, is chosen by minimizing the effective masses of some simple hadron operators at some early time separation t_S that is picked to be 1. Fig.3.2 shows how it is done. A single-site nucleon operator in which all three-quark fields are taken at the same site is shown, as well as a singly-displaced nucleon operator in which one of the quarks is displaced away from the other, and a triply-displaced-T operator in which all three quarks are displaced from the others in a T configuration. In this work, $\sigma_S^2 \approx 0.33$ is used. It is found that the choice is insensitive of the value of t_S as long as the excited states still dominate the correlator at that time.

3.2 Hadron Operators

The use of good hadron operators is crucial for extracting the mass spectrum. A 'good operator' is one that creates the states of interest out of the vacuum while suppressing the creation of unwanted higher-lying states. The construction of such operators has been discussed in Refs. [10, 12] and is not discussed here.

In the continuum, local operators which annihilate a hadron with momentum $\vec{p}$ and (anti)quarks of flavors A_f can be written as

$$\begin{aligned}
&\text{for mesons,} \\
O^{A_0A_1}(\vec{p},t) &= \delta_{ab}e^{-i\vec{p}\cdot\vec{x}}\gamma_{\alpha\beta}^{Jm_J}\bar{\psi}_{a\alpha}^{A_0}(x)\psi_{b\beta}^{A_1}(x) \\
\bar{O}^{A_0A_1}(\vec{p},t) &= \delta_{ab}e^{i\vec{p}\cdot\vec{x}}\gamma_{\alpha\beta}^{Jm_J*}\bar{\psi}_{b\beta}^{A_1}(x)\psi_{a\alpha}^{A_0}(x) \\
&\text{for baryons,} \\
O^{A_0A_1A_2}(\vec{p},t) &= \varepsilon_{abc}e^{-i\vec{p}\cdot\vec{x}}\gamma_{\alpha\beta\delta}^{Jm_J}\psi_{a\alpha}^{A_0}(x)\psi_{b\beta}^{A_1}(x)\psi_{c\delta}^{A_2}(x) \\
\bar{O}^{A_0A_1A_2}(\vec{p},t) &= \varepsilon_{abc}e^{i\vec{p}\cdot\vec{x}}\gamma_{\alpha\beta\delta}^{Jm_J*}\bar{\psi}_{c\delta}^{A_2}(x)\bar{\psi}_{b\beta}^{A_1}(x)\bar{\psi}_{a\alpha}^{A_0}(x)
\end{aligned} \tag{3.13}$$

for some spin tensors γ with spin J and spin $\hat{z}$-component m_J. A two-point function between operators O_1 and O_2 is then given by $\langle O_1\bar{O}_2\rangle$, in which the average is by Feynman integral. Similarly, it is expected that, on the lattice, O also carries the flavors and Dirac spin indices of the constituent quarks it contains and has a phase of a particular momentum. In order to construct extended operators that overlap better to non-local states, gauge-covariant displacements are also applied to the quarks in the definition of hadron operators. They are defined as follows:

$$\begin{aligned}
D^{(l_d),n}(\vec{x},\vec{x}') &\equiv \tilde{U}_n(\vec{x}')\tilde{U}_n(\vec{x}'+\hat{n})\ldots\tilde{U}_n(\vec{x}'+(l_d-1)\hat{n})\delta_{\vec{x},\vec{x}'+l_d\hat{n}}, \\
D^{(l_d),0}(\vec{x},\vec{x}') &\equiv \delta_{\vec{x},\vec{x}'}, \\
D^{(l_d),-n}(\vec{x},\vec{x}') &\equiv \tilde{U}_{-n}(\vec{x}')\tilde{U}_{-n}(\vec{x}'-\hat{n})\ldots\tilde{U}_{-n}(\vec{x}'-(l_d-1)\hat{n})\delta_{\vec{x},\vec{x}'-l_d\hat{n}},
\end{aligned} \tag{3.14}$$

in which n runs from 1 to 3 and l_d is the length of displacement taken to be 3 in this work. Such displacement combinations of the quarks for a particular hadron are denoted as D_u with collective index u that specifies the number of displacement operators applied and the values of l_d and n of each quark. Thus a hadron operator also carries displacement indices that specify how the quarks are displaced. In order to ensure the Hermiticity of correlation matrices involving baryons, it is more preferable to consider the antiquark field $\chi \equiv \bar{\psi}\gamma_4$ instead of $\bar{\psi}$. In the LapH subspace, according

to Eq. 3.7, the smeared (anti)quark fields are given by

$$\tilde{\psi}^{A}_{a\alpha}(x) = V_S(a;x)V_S^{\dagger}(b;y)\psi^{A}_{b\alpha}(y) \equiv V_S(a;x)\hat{\psi}^{A}_{\alpha} \tag{3.15}$$
$$\tilde{\chi}^{A}_{a\alpha}(x) = \chi^{A}_{b\alpha}(y)V_S(b;y)V_S^{\dagger}(a;x) \equiv \hat{\chi}^{A}_{\alpha}V_S^{\dagger}(a;x)$$

As mentioned in Ch. 2, the discretized Lagrangian is no longer invariant under the full Poincaré group of rotations, translations and boosts, but is invariant under the subgroup corresponding to the allowed rotations, translations and boosts on a hyper-cubic lattice. This means the correlation matrix should be block diagonal if the operators are constructed in a way that respects the symmetries on a lattice. It is thus important to exploit this feature to design good operators in order to efficiently obtain the hadron spectrum. The details of such construction are depicted in Appendix A. A general expression for a hadron operator O in the LapH subspace is therefore, introducing a collective index Λ which specifies the row and the ireducible representation the operator corresponds to, given by

for mesons, (3.16)

$$O^{\Lambda A_0 A_1}(\vec{p},x_4) \equiv C^{\Lambda}_{\alpha\beta;u}e^{-i\vec{p}\cdot\hat{n}_0}\Gamma^{ij}_u(\vec{p};x_4)\hat{\chi}^{A_0,i}_{\alpha}\hat{\psi}^{A_1,j}_{\beta},$$
$$\bar{O}^{\Lambda A_0 A_1}(\vec{p},x_4) \equiv C^{\Lambda *}_{\alpha\beta;u}e^{i\vec{p}\cdot\hat{n}_0}\Gamma^{ij*}_u(\vec{p};x_4)\hat{\chi}^{A_1,j}_{\beta}\hat{\psi}^{A_0,i}_{\alpha},$$
$$\Gamma_u(\vec{p};x_4) \equiv \delta_{ab}e^{-i\vec{p}\cdot\vec{x}}D_u V_S^{\dagger}(a;x)V_S(b;x)$$

for baryons,

$$O^{\Lambda A_0 A_1 A_2}(\vec{p},x_4) \equiv C^{\Lambda}_{\alpha\beta\delta;u}\Gamma^{ijk}_u(\vec{p};x_4)\hat{\psi}^{A_0,i}_{\alpha}\hat{\psi}^{A_1,j}_{\beta}\hat{\psi}^{A_2,k}_{\delta},$$
$$\bar{O}^{\Lambda A_0 A_1 A_2}(\vec{p},x_4) \equiv C^{\Lambda *}_{\alpha\beta\delta;u}\Gamma^{ijk*}_u(\vec{p};x_4)\hat{\psi}^{A_2,k}_{\delta}\hat{\psi}^{A_1,j}_{\beta}\hat{\psi}^{A_0,i}_{\alpha},$$
$$\Gamma_u(\vec{p};x_4) \equiv \varepsilon_{abc}e^{-i\vec{p}\cdot\vec{x}}D_u V_S(a;x)V_S(b;x)V_S(c;x),$$

for some coefficients C. The extra exponential factor in terms of $\hat{n}_0$, the midpoint between the displaced quark and antiquark, is inserted to ensure that the meson operators acquire G-parity symmetry. The quantities Γ are known as 'Hadron Elementals'. It is observed that Γ's are independent from the constituent quark flavors. Thus they can be recycled in the calculations of different operators that only differ by C. In this work, only correlation functions that involve two time-slices are considered. The earlier time is considered as the source time (denoted by t_0) and the later one is considered as the sink time (denoted by $t_1 \equiv t_0 + t$, t being the time separation). The

hadrons created at the source time are considered as source hadron operators while the hadrons annihilated at sink time are considered as sink hadron operators.

Since there are a lot of symmetry channels and displacement types for each hadron sector, many possible hadron operator coefficients C can be constructed. Not only it takes overwhelmingly huge resources to compute all of them, but also there is no such need. The first reason is that some operators are intrinsically too noisy to give significant signals, i.e. there is no impact on the computation by throwing them away. The second one is that not all operators are independent from one another. Actually many of them are not, indicated by the large condition numbers of the correlator matrices constructed from them. Moreover, one does not need too many independent operators to obtain the first few lowest-lying levels of the spectra. As a result, a 'pruning' has been performed to crop out optimal sets of quiet independent operators in each sector. The results are described in Appendix B.

3.2.1 Glueball Operators

Glueballs G are particles believed to be composed mainly of gluons. Pure gauge simulations [33] show that they are expected to be very heavy in mass and the lightest state is known to be the ground state of scalar sector G_S. As far as the low-lying hadron spectra are concerned, G_S is expected to be the only particle that will be needed. It has the same quantum numbers as the isoscalar scalars so it will mix with f_0, as well as any multi-hadron combinations with the same set of quantum numbers. Traditionally, G_S states are probed by the smeared plaquette operators, which consist of Wilson loops in different combinations [33]. Within the context of LapH smearing, a convenient G_S operator can be obtained immediately after the computation of the eigenpairs of $-\tilde{\Delta}$. Such an operator is

$$G_S^{\Delta}(x_4) \equiv -\operatorname{Tr}(P_{[x_4]} S\tilde{\Delta}) = -\operatorname{Tr}\left(P_{[x_4]}\Theta\left(\sigma_S^2+\tilde{\Delta}\right)\tilde{\Delta}\right) = \sum_{|\lambda_{i,x_4}|<\sigma_S^2} \lambda_{i,x_4} \approx \sum_{i=0}^{N_v-1} \lambda_{i,x_4}, \tag{3.17}$$

where

$$P^{ab}_{[x_4]}(x',y';U) \equiv \delta^{ab}\delta_{x_4,x_4'}\delta_{x',y'} \text{ (no sum over } x' \text{ or } x_4') \tag{3.18}$$

projects out the block of $S\tilde{\Delta}$ at time x_4 and λ_{i,x_4} is the i^{th} eigenvalue of $-\tilde{\Delta}$ at time x_4. $G_S^{\Delta}(x_4)$ is a valid operator because it is free from constituent quarks, gauge-invariant

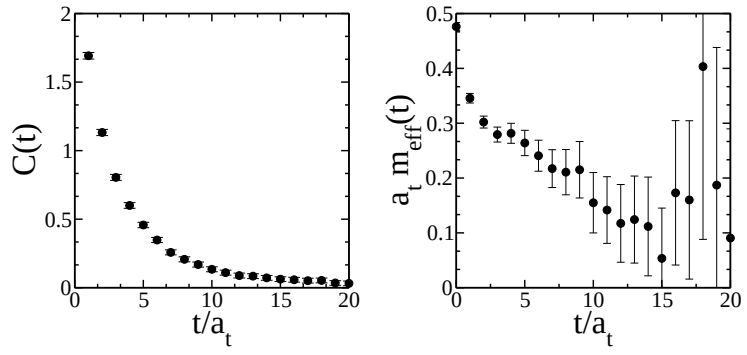

(a) Correlator of a Plaquette Operator (b) m_{eff} of a Plaquette Operator

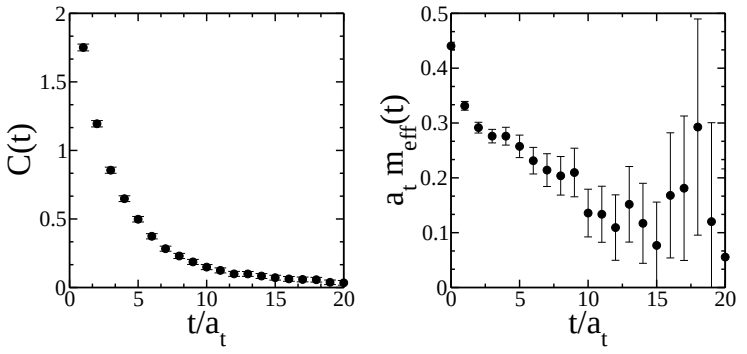

(c) Correlator of G_S^{Δ} (d) m_{eff} of G_S^{Δ}

Figure 3.3: Comparison between glueball operators on 584 configurations of $\{24^3; 860\}$ ensemble. [53] The first row shows the correlator and effective mass of a typical smeared plaquette operator, while the second row shows the correlator and effective mass of the G_S^{Δ} operator defined in Eq. 3.17. It is observed that their variances are very close to each other.

and has the same quantum numbers of G_S. Such an operator is a bonus from the LapH algorithm. It turns out that such operator gives signals of the same quality as traditional smeared plaquettes. Fig. 3.3 compares the signals between the two on the $\{24^3; 860\}$ ensemble. It is observed that they give very similar signals.

3.3 LapH Quark Propagators

As discussed in Sec. 2.1 , the Grassmann-valued (anti)quark fields $\bar{\psi}$ and ψ are not quantities obtainable directly in the Monte Carlo simulation. They are integrated out in favor of the propagator, $M^{-1} = \psi\bar{\psi}$. Due to the re-definition of $\bar{\psi}$ into χ, the propagator is now defined as $\Omega^{-1} \equiv \psi\chi$, where $\Omega \equiv \gamma_4 M$. Smearing in the LapH

subspace, using Eq. 3.7 and Eq. 3.12,

$$\tilde{\Omega}^{-1} \equiv S\Omega^{-1}S = S\psi\chi S = \tilde{\psi}\tilde{\chi} = V_S\hat{\psi}\hat{\chi}V_S^\dagger \equiv V_S K V_S^\dagger, \tag{3.19}$$

in which

$$K \equiv \hat{\psi}\hat{\chi} = V_S^\dagger \Omega^{-1} V_S. \tag{3.20}$$

The evaluation of K is computationally very expensive due to the enormous size of the matrix. A straightforward way of doing so is as follows. Let

$$v_{c\beta}^{(i,\alpha)}(x) \equiv V_S^i(c;x)\delta_{\alpha\beta}, \tag{3.21}$$

in which x is the lattice site, c is color index and α, β are spin indices. The solution of $\Omega u = v^{(i,\alpha)}$ gives

$$u_{d\gamma}^{(i,\alpha)}(y) = \Omega^{-1}_{d\gamma|c\alpha}(y,x)V_S^i(c;x), \tag{3.22}$$

which can be computed numerically using variants of common Conjugate-Gradient methods. After performing inversions for all N_v i's and $N_D = 4$ α's, $K = V_S^\dagger u$ can be obtained. Thus, for each gauge configuration and each quark mass, $N_v N_t N_D$ such inversions are required. In cases where only non-isoscalar single hadron 2-point correlators are of interest, only quark lines that start from several source times, $N_t^{(\mathrm{src})}$, are involved. Therefore the number of inversions can be reduced to $N_v N_t^{(\mathrm{src})} N_D$. In principle $N_t^{(\mathrm{src})}$ can be taken to be 1, but statistics can be boosted by increasing it. Thus the number of inversions can be as low as $N_v N_D$. However, if multi-hadron or isoscalar operators are considered, quark lines that start and end in the same time-slice are needed. These quark lines may connect between the source hadron operators or between the sink hadron operators. In particular, if it happens that such quark lines connect the sink hadron operators, the number of inversion is proportional to the number of sink time t_1's required, $N_t^{(\mathrm{snk})}$. This number can be comparable to N_t if it happens that a long range of sink time is required for energy extraction. Therefore the number of inversions needed becomes of the order of $N_v N_t N_D$ again. In small lattices, this amount of inversions can be handled at ease, so it is not really an issue. However, N_v is actually proportional to the spatial volume. The eigenvalues of $-\tilde{\Delta}$ go like $|\vec{k}|^2$ for wavevectors $\vec{k}$(suppressing other indices). It is known that $|\vec{k}| \sim n2\pi N_s^{-1}$ for some integer n. For a given cutoff σ_S, the number of eigenstates

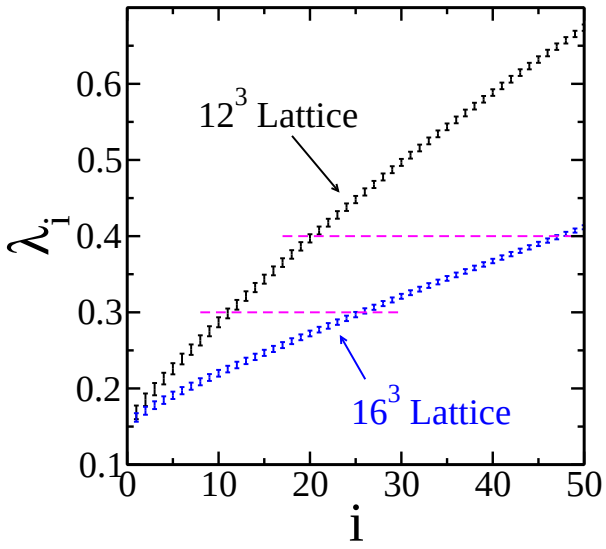

Figure 3.4: The volume dependence of the eigenvalues of the gauge-covariant Laplacian operator. λ_i is the i^{th} lowest eigenvalue of $-\tilde{\Delta}$ on a given time-slice. The error bars correspond to the variation over different time-slices. Within the region $0.3 < \lambda_i < 0.4$ there are 9 eigenstates for 12^3 Lattice while there are 22 for the 16^3 one. [10]

with $|\vec{k}|^2 \leq \sigma_S^2 \equiv |n_{\max} 2\pi N_s^{-1}|^2$, N_v, is given by:

$$\begin{aligned} N_v &= \frac{4\pi}{3} n_{\max}^3 \\ &= \frac{1}{6\pi^2} \sigma_S^3 N_s^3. \end{aligned} \tag{3.23}$$

In other words, for a fixed σ_S, $N_v \propto N_s^3$. Fig. 3.4 demonstrates this effect on spatial lattice sizes 12^3 and 16^3. Within the region $0.3 < \lambda_i < 0.4$ there are 9 eigenstates for 12^3 Lattice while there are 22 for the 16^3 one. Therefore, for larger lattices in which each individual inversion is already more expensive, the number of required inversions also increases proportionally due to the scaling of the number of eigenvectors with spatial volume in order to keep the cutoff eigenvalue σ_S unchanged. This makes the straightforward calculation of the quark lines very costly or even not feasible on larger lattices. Thus some tricks have to be employed. In this work, noises are introduced into the calculation to tackle this problem. Such an algorithm is named Stochastic LapH method [10] and is described in detail in Sec. 3.4.

3.4 Stochastic LapH Algorithm

In Sec. 3.3, it was found that straightforward calculations of quark lines are too expensive to be performed in large lattices. In this work, the technique to solve the problem is to introduce noises in the calculation of the inversions. Such an algorithm is based on the important observation that an exact calculation of K is actually unnecessary. The statistical errors in the estimation of the correlators of interest are indeed limited by the statistical fluctuations of gauge generations from Monte Carlo method. This means one cannot further improve the signals once the errors in the estimation of quark lines of each gauge configuration has reached such 'gauge noise limit'. Therefore it is wasteful to calculate the inversions at maximum accuracy, i.e. in an exact manner. This allows the notion of a stochastic estimation of the inversions at an accuracy comparable to the 'gauge noise limit' without significant increases in the variance in the correlators and consequently extracted energies. In this section, such technique is discussed and there are some small-lattice results to determine the values of stochastic parameters such as dilution schemes, to demonstrate the feasibility of the method and thus to justify its application upon larger lattices.

3.4.1 Stochastic Estimator with Dilution Enhancement

In the LapH subspace and spin space, define an evenly-random vector ρ, in which each component $\rho_{i\alpha}(x_4) \in Z_n$, where $Z_n \equiv e^{i2\pi m/n}$ for some integer n and integer m satisfying $0 < m < n$. n is taken to be 4 in this work. Consider the linear system

$$\Omega\phi = V_S\ \rho, \tag{3.24}$$

in which the solution ϕ can be numerically calculated using variants of Conjugate-Gradient methods. Suppose there are N_r such random ρ's. Since

$$1 = E(\rho\rho^\dagger) \approx \frac{1}{N_r}\sum_{r=0}^{N_r-1}\rho^{(r)}\rho^{(r)\dagger}, \tag{3.25}$$

it is expected that

$$
\begin{aligned}
K &= V_S^\dagger \Omega^{-1} V_S \\
&= V_S^\dagger E((\Omega^{-1} V_S \rho)\rho^\dagger) \\
&= V_S^\dagger E(\phi \rho^\dagger) \\
&\approx \frac{1}{N_r} \sum_{r=0}^{N_r-1} V_S^\dagger \phi^{(r)} \rho^{(r)\dagger} \\
&\equiv \frac{1}{N_r} \sum_{r=0}^{N_r-1} \varphi^{(r)} \rho^{(r)\dagger},
\end{aligned}
\tag{3.26}
$$

in which φ and ρ are defined as 'Quark Sinks' and 'Quark Sources' respectively. In principle, if N_r is large enough for averaging, K can be approximately obtained in this way. However, the statistical error can be huge. Therefore, given a target variance, namely the gauge noise limit in the current case, it is not obvious whether more or fewer inversions are needed compared with the 'exact' approach described in Sec. 3.3. In fact, according to previous experiences of the same stochastic technique applied on the lattice sites and color space instead of LapH subspace, such stochastic estimation introduces a lot of additional noises that overwhelm important signals. It is expected that this is also true in the LapH subspace. This leads to the notion of applying the 'dilution' improvement technique that was previously developed in the former situation [6].

In the stochastic estimation described above, ρ is defined on the entire LapH subspace and spin space and is inverted all at once. Actually it does not need to be the case. ρ can be projected onto different sets of indices and then inversions are performed separately on each of them. The results can then be re-combined to give an estimation of the full K. The implementation is as follows.

Denote the collection of the index values of time values by $\mathbb{T}$, that of LapH eigenvectors by $\mathbb{L}$ and that of spin values by $\mathbb{S}$. Divide these collections into disjoint subsets denoted by $\mathbb{T}^{d_T}$, $\mathbb{S}^{d_S}$ and $\mathbb{L}^{d_L}$ respectively, where d's are integers specifying the subsets. For each set, there are several ways of splitting. These schemes are known as the 'Dilution schemes' $\mathcal{D}$. In this work, 4 types of dilution schemes are studied. 'Null'(N) dilution scheme refers to the situation in which one subset contains all elements. 'Full'(F) dilution scheme refers to the situation in which there is one element in each subset. 'Interlace-q'(Id) dilution scheme refers to the situation in which each

of q subsets contains N/q elements separated by q consecutive values, where N is the total number of elements in the whole set. 'Block-q'(Bq) dilution scheme refers to the situation in which each of q subsets contains N/q consecutive values. In other words, denoting $P^{[d]}_{mn}\Big|_{\mathcal{D}}$ as the projector that projects out the indices within dilution scheme $\mathcal{D}$,

$$\begin{aligned}
P^{[d]}_{mn}\big|_{\mathrm{N}} &= \delta_{m,n}, && d = 0 \\
P^{[d]}_{mn}\big|_{\mathrm{F}} &= \delta_{m,n}\delta_{d,m}, && d = 0, 1, \cdots, N-2, N-1 \\
P^{[d]}_{mn}\big|_{\mathrm{I}q} &= \delta_{m,n}\delta_{d,m \bmod q}, && d = 0, 1, \cdots, q-2, q-1 \\
P^{[d]}_{mn}\big|_{\mathrm{B}q} &= \delta_{m,n}\delta_{d,mq/N}, && d = 0, 1, \cdots, q-2, q-1.
\end{aligned} \tag{3.27}$$

Let $P^{[d_T][d_S][d_L]}\big|_{\mathcal{D}_{TSL}}$ denote the projector that projects out indices (x_4, α, i) within the set $\mathbb{T}^{d_T} \otimes \mathbb{S}^{d_S} \otimes \mathbb{L}^{d_L}$ for dilution scheme $\mathcal{D}_{TSL}$:

$$\begin{aligned}
P^{[d_T][d_S][d_L]}_{x_4,\alpha,i|y_4,\beta,j}\Big|_{\mathcal{D}_{TSL}} &\equiv P^{[d_T]}_{x_4 y_4}\big|_{\mathcal{D}_T}\, P^{[d_S]}_{\alpha\beta}\Big|_{\mathcal{D}_S}\, P^{[d_L]}_{ij}\Big|_{\mathcal{D}_L} \\
&= \sum_{x_4' \in \mathbb{T}^{d_T}} \sum_{\alpha' \in \mathbb{S}^{d_S}} \sum_{i' \in \mathbb{L}^{d_L}} \delta_{x_4 x_4'} \delta_{x_4 y_4} \delta_{\alpha\alpha'} \delta_{\alpha\beta} \delta_{ii'} \delta_{ij} \Bigg|_{\mathcal{D}_{TSL}}.
\end{aligned} \tag{3.28}$$

Then, for a given dilution scheme, the diluted noises can be defined as

$$\rho^{[d_{TSL}](r)} \equiv P^{[d_T][d_S][d_L]} \rho^{(r)}, \tag{3.29}$$

in which d_{TSL} is the collective index for d_T , d_S and d_L. Since Eq. 3.25 is now

$$1 = \sum_{d_{TSL}} E(\rho^{[d_{TSL}]} \rho^{[d_{TSL}]\dagger}) \approx \frac{1}{N_r} \sum_{r=0}^{N_r - 1} \sum_{d_{TSL}} \rho^{[d_{TSL}](r)} \rho^{[d_{TSL}](r)\dagger}, \tag{3.30}$$

Eq. 3.26 becomes

$$K \approx \frac{1}{N_r} \sum_{r=0}^{N_r - 1} \sum_{d_{TSL}} \varphi^{[d_{TSL}](r)} \rho^{[d_{TSL}](r)\dagger}, \tag{3.31}$$

where

$$\varphi^{[d_{TSL}](r)} \equiv V_S^\dagger \Omega^{-1} V_S \rho^{[d_{TSL}](r)}. \tag{3.32}$$

With dilution, the variance can be greatly reduced by ensuring exact zeros for many of the $E(\rho_m \rho_n^*)$ elements in Eq. 3.30 due to the orthogonality of the projectors. (Illustrated in Fig. 3.5) This improvement comes at a price of an increase in the number of inversions per configuration per noise seed. Since the number of inversions per noise seed is directly proportional to the number of dilution projectors, the variance can be systematically reduced by tuning the dilution scheme until the variance is comparable to the gauge noise limit. Once this is reached, there is no way to improve further without generating more configurations. Thus it suffices to stay in such dilution scheme. The dilution scheme determined in this manner turns out to require far fewer inversions than that required by the full dilution scheme, i.e. 'Exact' calculation, while the variance is still close to the full dilution scheme. It is discussed in detail in Sec. 3.6.

Occasionally, the γ_5-Hermiticity of the Dirac Matrix can be exploited. In Euclidean spacetime,

$$\left(M^{-1}\right)^\dagger = \gamma_5 M^{-1} \gamma_5. \tag{3.33}$$

In terms of K,

$$\begin{aligned} K^\dagger &= (V_S^\dagger M^{-1} \gamma_4 V_S)^\dagger \\ &= V_S^\dagger \gamma_4 \left(M^{-1}\right)^\dagger V_S \\ &= \gamma_4 \gamma_5 V_S^\dagger M^{-1} V_S \gamma_5 \\ &= -\gamma_5 \gamma_4 K \gamma_4 \gamma_5. \end{aligned} \tag{3.34}$$

Therefore, according to Eq. 3.31, K can be estimated in a different way:

$$\begin{aligned} K &= (-\gamma_5 \gamma_4 K \gamma_4 \gamma_5)^\dagger \\ &= -\gamma_5 \gamma_4 K^\dagger \gamma_4 \gamma_5 \\ &\approx -\gamma_5 \gamma_4 \frac{1}{N_r} \sum_{r=0}^{N_r-1} \sum_{d_{TSL}} \rho^{[d_{TSL}](r)} \varphi^{[d_{TSL}](r)\dagger} \gamma_4 \gamma_5 \\ &\equiv \frac{1}{N_r} \sum_{r=0}^{N_r-1} \sum_{d_{TSL}} \bar{\rho}^{[d_{TSL}](r)} \bar{\varphi}^{[d_{TSL}](r)\dagger}, \end{aligned} \tag{3.35}$$

where

$$\bar{\rho}^{[d_{TSL}](r)} \equiv -\gamma_5\gamma_4\rho^{[d_{TSL}](r)} \qquad (3.36)$$
$$\bar{\varphi}^{[d_{TSL}](r)} \equiv \gamma_5\gamma_4\varphi^{[d_{TSL}](r)}.$$

Effectively, this algorithm is performing a Monte Carlo inside a Monte Carlo. Thus it is equivalent to a larger Monte Carlo that includes the noises as one of the random variables. Therefore in practice $N_r = 1$ will do the job most of the time. This simplification is adopted in this work unless otherwise is specified.

Quarkline End Combinations Φ

Equipped with the expressions of the stochastic estimations of K in terms of φ and ρ, one can finish the construction of O, the building blocks that would be used for the estimation of the N-point correlation functions, by replacing the fermion fields with φ and ρ. It is observed that computing the hadron operators separately is in fact not possible if K were computed in a straightforward way. The elements of K needed are diagram-dependent. Wick contraction has to be performed one diagram by another to obtain the set of K's to be generated. Unless all elements of K are generated, it is always possible that new elements of K have to be generated when the study develops from one correlation function to another. As discussed previously, it is not practical to exhaust all elements of K using current computational resources. This imposes an inconvenience of the simulation, especially multi-hadron calculations that involve a variety of diagrams. Fortunately, in the stochastic estimation, according to Eq. 3.31, the propagator is factorized back into two parts, φ and ρ:

$$\begin{aligned}\hat{\psi}\hat{\chi} &= K \qquad (3.37)\\ &\approx \frac{1}{N_r}\sum_{r=0}^{N_r-1}\sum_{d_{TSL}} \varphi^{[d_{TSL}](r)}\rho^{[d_{TSL}](r)\dagger}\\ &= \varphi^{[d_{TSL}]}\rho^{[d_{TSL}]\dagger},\ N_r = 1,\end{aligned}$$

in which the summation over d_{TSL} is implicitly implied. Alternatively, exploiting γ_5-Hermiticity (Eq. 3.35),

$$\hat{\psi}\hat{\chi} = \bar{\rho}^{[d_{LTS}]}\bar{\varphi}^{[d_{LTS}]\dagger}. \qquad (3.38)$$

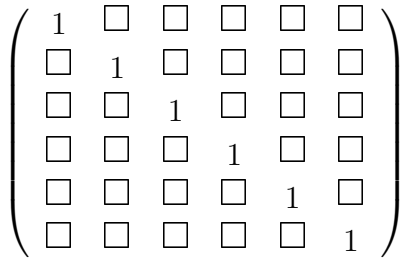

(a) N: Null Dilution, Number of Projectors=1

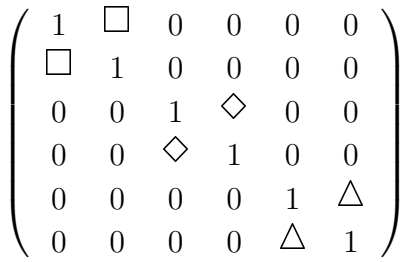

(b) B3: Block Dilution, Number of Projectors=3

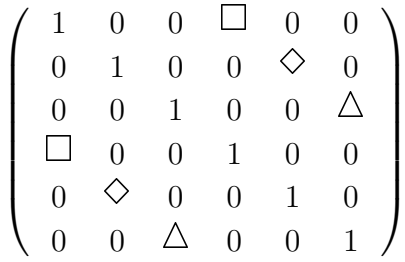

(c) I3: Interlace Dilution, Number of Projectors=3

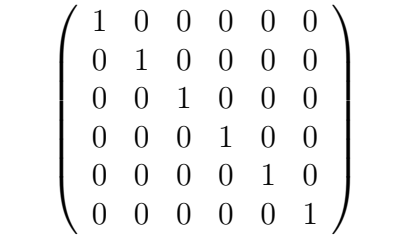

(d) F: Full Dilution, Number of Projectors=6

Figure 3.5: Illustration of Dilution Schemes on a 6-dimensional vector space. The identity is diluted in different ways. Hollow symbols average to 0. The different shapes represent three different projectors. It is observed that a lot of the off-diagonal elements are 0 due to the orthogonality of the projectors once dilution is applied.

This allows one to compute the φ and ρ separately and attach them separately to different hadron operators before Wick contractions, accomplishing a factorization in terms of O like the continuum case. This brings back the flexibility of the computation. However, it is noted that φ(or $\bar{\rho}$) and ρ(or $\bar{\varphi}$) do not correspond directly to $\hat{\psi}$ and $\hat{\chi}$. There exists some residual dependence on the kind of N-point function to be calculated, if the dilution schemes are different for different quark lines. There is also a freedom of whether γ_5-Hermiticity is employed. Moreover, the seeds of different quarks within the same hadron operator have to be different in order to avoid bias. Therefore each hadron operator is associated with a collection of combinations of 'Quarkline Ends' θ, which are either φ, ρ, $\bar{\rho}$ or $\bar{\varphi}$, with different dilution schemes $\mathcal{D}_i$ and noise seeds r_i to accommodate the needs of different diagrams and conventions, resulting in the forms Φ, $\bar{\Phi}$:

$$
\begin{aligned}
&\text{for meson operators ,} \qquad (3.39)\\
&\Phi^{\Lambda}[\theta^{A_0,\mathcal{D}_0(r_0)},\theta^{A_1,\mathcal{D}_1(r_1)}]_{d_0d_1}(\vec{p},x_4)\\
&\qquad\qquad \equiv C^{\Lambda}_{\alpha\beta;u} e^{-i\vec{p}\cdot\hat{n}_0}\Gamma^{ij}_u(\vec{p};x_4)\theta^{[d_0]A_0,\mathcal{D}_0(r_0)}_{\alpha,i}\theta^{[d_1]A_1,\mathcal{D}_1(r_1)}_{\beta,j},\\
&\bar{\Phi}^{\Lambda}[\theta^{A_0,\mathcal{D}_0(r_0)},\theta^{A_1,\mathcal{D}_1(r_1)}]_{d_0d_1}(\vec{p},x_4)\\
&\qquad\qquad \equiv \left(\Phi^{\Lambda}[\ \theta^{A_0,\mathcal{D}_0(r_0)},\theta^{A_1,\mathcal{D}_1(r_1)}]_{d_0d_1}(\vec{p},x_4)\right)^*,\\
&\text{for baryon operators ,}\\
&\Phi^{\Lambda}[\theta^{A_0,\mathcal{D}_0(r_0)},\theta^{A_1,\mathcal{D}_1(r_1)},\theta^{A_2,\mathcal{D}_2(r_2)}]_{d_0d_1d_2}(\vec{p},x_4)\\
&\qquad\qquad \equiv C^{\Lambda}_{\alpha\beta\delta;u}\Gamma^{ijk}_u(\vec{p};x_4)\theta^{[d_0]A_0,\mathcal{D}_0(r_0)}_{\alpha,i}\theta^{[d_1]A_1,\mathcal{D}_1(r_1)}_{\beta,j}\theta^{[d_2]A_2,\mathcal{D}_2(r_2)}_{\delta,k},\\
&\bar{\Phi}^{\Lambda}[\theta^{A_0,\mathcal{D}_0(r_0)},\theta^{A_1,\mathcal{D}_1(r_1)},\theta^{A_2,\mathcal{D}_2(r_2)}]_{d_0d_1d_2}(\vec{p},x_4)\\
&\qquad\qquad \equiv \left(\Phi^{\Lambda}[\theta^{A_0,\mathcal{D}_0(r_0)},\ \theta^{A_1,\mathcal{D}_1(r_1)},\theta^{A_2,\mathcal{D}_2(r_2)}]_{d_0d_1d_2}(\vec{p},x_4)\right)^*.
\end{aligned}
$$

In this work, only the quark lines that connect different time-slices and start from the sink time-slices adopt the γ_5-Hermiticity convention. It is natural that the dilution schemes should be dependent on the type of quark line to be estimated, since the quark lines starting and ending on the same time-slice (referred to as 'relative-source-time' or 'same-time') are typically noisier than those propagating across different time-slices (referred to as 'fixed-source-time'). In this work, two different dilution schemes are applied to these two types of quark lines, namely the 'Fixed Dilution Scheme' (represented by subscripts f) for fixed-source-time quark lines and 'Relative

Dilution Scheme' (represented by subscripts r) for relative-source-time quark lines. They are chosen to only differ in time dilution, since that is the only aspect that the type of quark lines really matters. For the Fixed Dilution Scheme, Full Dilution in time is preferable because the number of inversions required is proportional to $N_t^{(\mathrm{src})}$, which does not scale with volume significantly. The only effect of using non-Full dilution is just to introduce slightly more noise, which is not preferred. The number of source time-slices are taken to be 4 in this work. In contrast, the number of inversions required for the Relative Dilution Scheme is either a range of time-slices if the quark line resides on the sink time-slices, or $N_t^{(\mathrm{src})}$ if it resides on the source time-slices. Recall that if the inversions were done in an exact manner (Full Dilution), a lot of extra inversions have to be performed if the quark line resides on the sink time-slices. Even if the quark lines reside on the source time-slices, $N_t^{(\mathrm{src})}$ has to be much higher than that used in the fixed-source-time quark lines due to the fact that relative-source-time quark lines tend to be noisier. After all, this is one of the motivations to introduce noises into the calculation, especially into the time domain, in the first place. Therefore a non-Full Dilution in time is preferred in this type of quark lines. The number of source time-slices of the correlator is chosen to be the entire temporal extent N_t, since they are all available anyway after the inversions. It is more preferable to be an interlaced scheme rather than blocked one in order to minimize the noise contaminations on consecutive time-slices, since the temporal behavior of the correlator is the most important information in determination of the energy levels and it should be as clean as possible. However, it should be noted that in cases where both types of quark lines exist on the source time-slice in the same diagram, the dilution scheme is taken to be Full Dilution for both, since there are only $N_t^{(\mathrm{src})}$ source time-slices available for that diagram and there is no benefit of using non-Full Dilution Scheme, which again only introduces unnecessary noises. For simplicity, the quark line-ends and the combinations are represented as follows in the

coming figures.

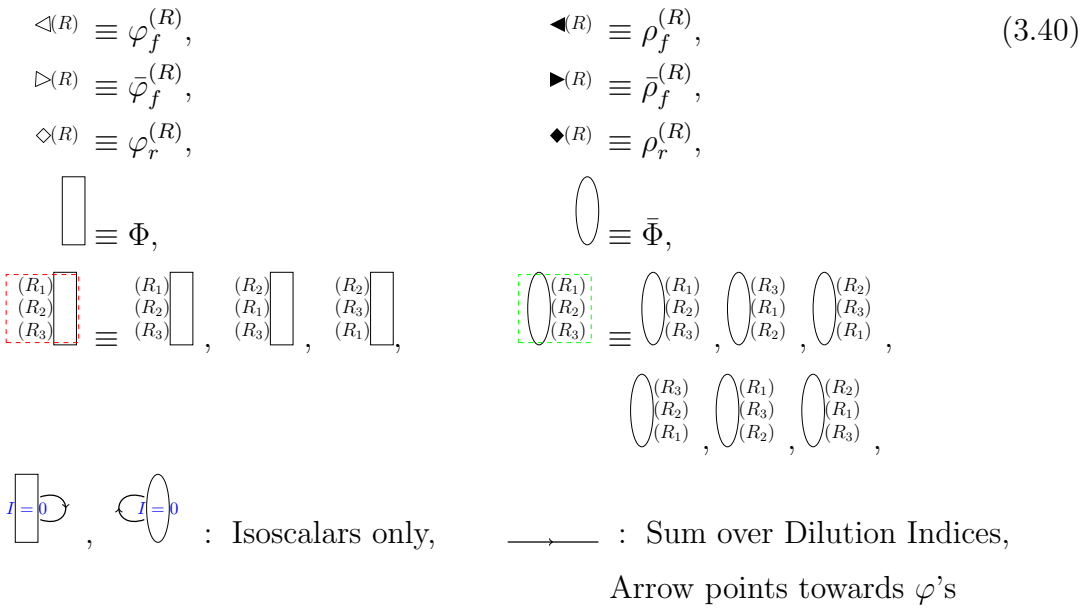

(3.40)

in which R represents the noise seeds that are labeled from 0 to 4 for Fixed Dilution Scheme(f) and a to b for Relative Dilution Scheme(r) and other indices are suppressed. The numbers of seeds used are chosen such that they satisfy the minimum requirement of computing the diagrams of interest.

For example, the single-hadron correlators at rest are computed by:

for mesons, (3.41)

$$C_{\Lambda\bar{\Lambda}}(t) = \Big\langle -\delta^{\bar{A}_0\bar{A}_1}_{A_0A_1}\Phi^{\Lambda}[\bar{\varphi}_f^{A_0(r_0)},\varphi_f^{A_1(r_1)}]_{d_0d_1}(\vec{0},t_1)\bar{\Phi}^{\bar{\Lambda}}[\bar{\rho}_f^{\bar{A}_0(r_0)},\rho_f^{\bar{A}_1(r_1)}]_{d_0d_1}(\vec{0},t_0) + \delta^{A_1\bar{A}_1}_{A_0\bar{A}_0}\Phi^{\Lambda}[\bar{\varphi}_r^{A_0(r_a)},\varphi_r^{A_1(r_a)}]_{d_0d_0}(\vec{0},t_1)\bar{\Phi}^{\bar{\Lambda}}[\bar{\rho}_r^{\bar{A}_0(r_b)},\rho_r^{\bar{A}_1(r_b)}]_{d_1d_1}(\vec{0},t_0)\Big\rangle_{U,r},$$

for baryons,

$$\begin{aligned}C_{\Lambda\bar{\Lambda}}(t) = \Big\langle &\Phi^{\Lambda}[\varphi_f^{A_0(r_0)},\varphi_f^{A_1(r_1)},\varphi_f^{A_2(r_2)}]_{d_0d_1d_2}(\vec{0},t_1)\cdot\\ &\Big(\delta^{\bar{A}_0\bar{A}_1\bar{A}_2}_{A_0A_1A_2}\bar{\Phi}^{\bar{\Lambda}}[\rho_f^{\bar{A}_0(r_0)},\rho_f^{\bar{A}_1(r_1)},\rho_f^{\bar{A}_2(r_2)}]_{d_0d_1d_2}(\vec{0},t_0)\\ &+\delta^{\bar{A}_1\bar{A}_2\bar{A}_0}_{A_0A_1A_2}\bar{\Phi}^{\bar{\Lambda}}[\rho_f^{\bar{A}_1(r_1)},\rho_f^{\bar{A}_2(r_2)},\rho_f^{\bar{A}_0(r_0)}]_{d_1d_2d_0}(\vec{0},t_0)\\ &+\delta^{\bar{A}_1\bar{A}_2\bar{A}_0}_{A_0A_1A_2}\bar{\Phi}^{\bar{\Lambda}}[\rho_f^{\bar{A}_2(r_2)},\rho_f^{\bar{A}_0(r_0)},\rho_f^{\bar{A}_1(r_1)}]_{d_2d_0d_1}(\vec{0},t_0)\\ &-\delta^{\bar{A}_0\bar{A}_2\bar{A}_1}_{A_0A_1A_2}\bar{\Phi}^{\bar{\Lambda}}[\rho_f^{\bar{A}_0(r_0)},\rho_f^{\bar{A}_2(r_2)},\rho_f^{\bar{A}_1(r_1)}]_{d_0d_2d_1}(\vec{0},t_0)\\ &-\delta^{\bar{A}_1\bar{A}_0\bar{A}_2}_{A_0A_1A_2}\bar{\Phi}^{\bar{\Lambda}}[\rho_f^{\bar{A}_1(r_1)},\rho_f^{\bar{A}_0(r_0)},\rho_f^{\bar{A}_2(r_2)}]_{d_1d_0d_2}(\vec{0},t_0)\\ &-\delta^{\bar{A}_2\bar{A}_1\bar{A}_0}_{A_0A_1A_2}\bar{\Phi}^{\bar{\Lambda}}[\rho_f^{\bar{A}_2(r_2)},\rho_f^{\bar{A}_1(r_1)},\rho_f^{\bar{A}_0(r_0)}]_{d_2d_1d_0}(\vec{0},t_0)\Big)\Big\rangle_{U,r},\end{aligned}$$

in which $\delta^{CD}_{AB} \equiv \delta^C_A\delta^D_B$ and $\delta^{DEF}_{ABC} \equiv \delta^D_A\delta^E_B\delta^F_C$. The diagrams involved are shown in Fig. 3.6.

Similar to Single-Hadron Operators, Multi-Hadron Operators can be constructed by combining the Single-Hadron Operators according to the lattice symmetries described in Appendix A. In this work, the multi-baryon operators and operators with more than 2 hadrons are ignored, since the energy states they couple to lie above the energy range of interest. After Wick contractions, the N-point correlators constructed from the Multi-Hadron operators under consideration are linear combinations of the diagrams listed in Fig. 3.7 and Fig. 3.8.

The most economical way to compute the hadron operators above is to determine the minimal set of Φ's required for the diagrams of interest with only 1 noise combination. Then, if more statistics are required, the number of noise combinations can be increased by permuting them. This leads to the need of a survey of what kind of combinations are needed in the entire intended simulation. Summarizing the previous discussion, all types of diagrams under consideration are those shown in Fig. 3.6 to Fig. 3.8. According to them, one can construct a minimal set of Φ's required. Since in the pruning of hadron operators, the list of hadron operators used in diagrams

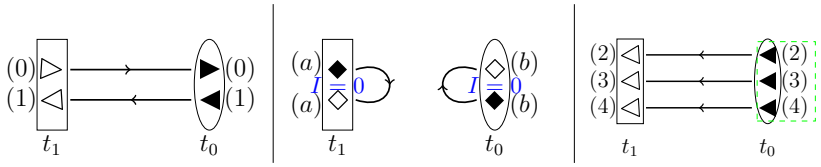

Figure 3.6: Diagrams needed in Single-Hadron Correlators

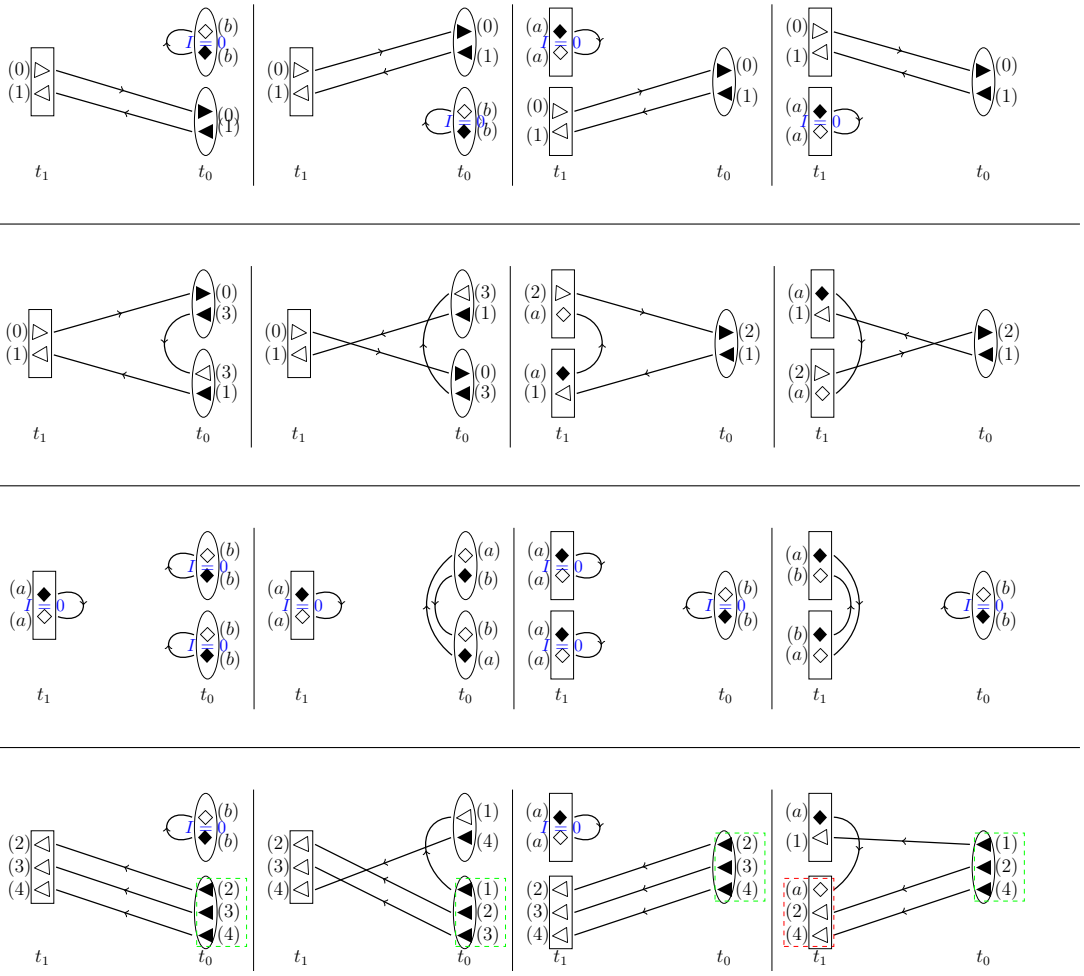

Figure 3.7: Diagrams needed in Single-Hadron-Two-Hadron Correlators

involving multi-hadron operators is different from that for diagrams which do not contain multi-hadron operators, it is useful to keep track of what kind of diagrams the combinations come from in order not to compute extra operators. The results are shown in Table 3.1 and Table 3.2.

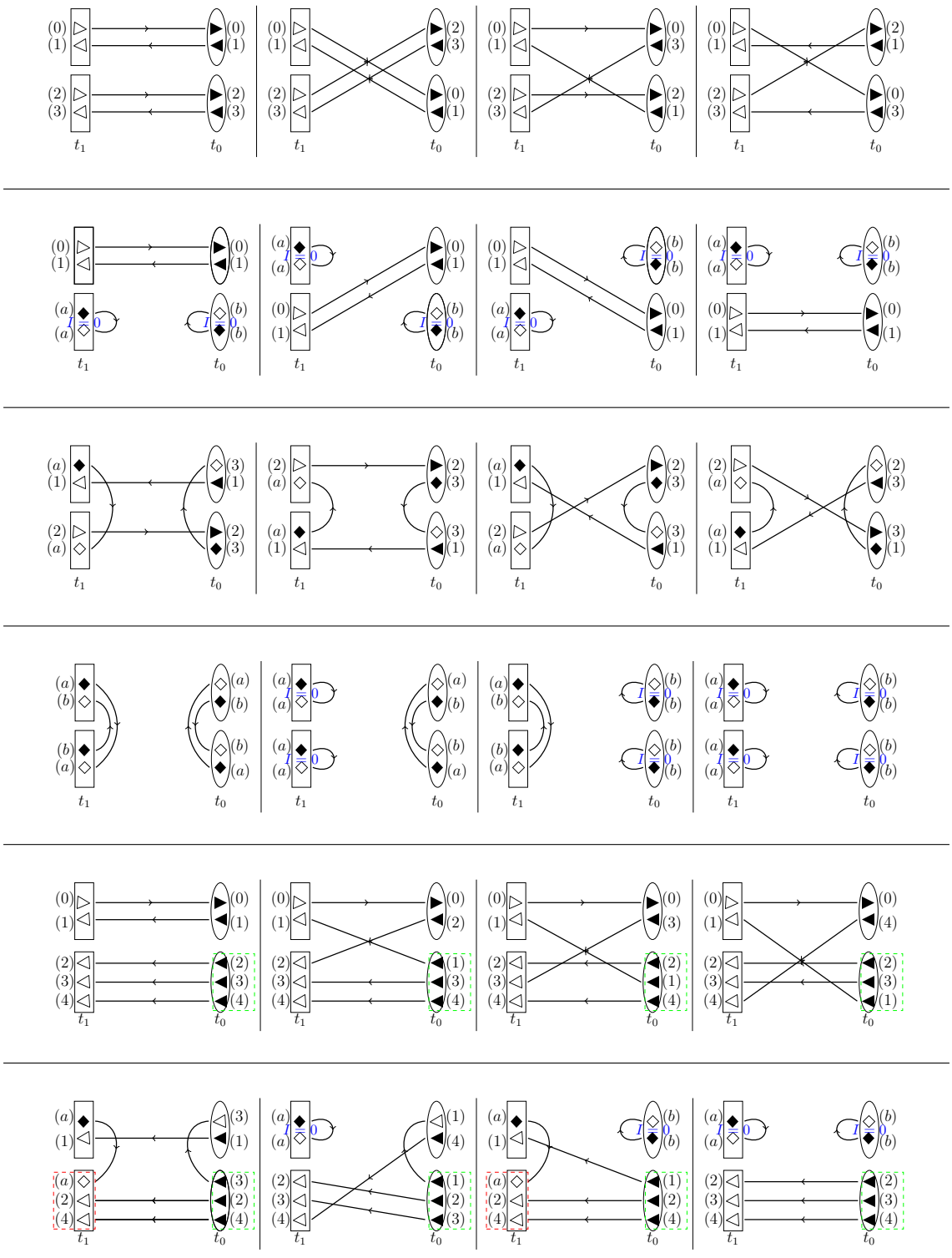

Figure 3.8: Diagrams needed in Two-Hadron-Two-Hadron Correlators

Table 3.1: The Minimal Set of Quarkline End Combinations of Mesons. The combinations required by diagrams consisting multi-hadron operators are marked as 'M' and those that are required by diagrams consisting of single-hadron operators only are marked as 'S'.

# of Time-slices	Quarkline Ends
$N_t^{(\mathrm{snk})}$	$\Phi[\bar{\varphi}_f, \varphi_f]$ 
	$\Phi[\bar{\varphi}_f, \varphi_r]$ 
	$\Phi[\rho_r, \varphi_f]$ 
$N_t^{(\mathrm{src})}$	$\bar{\Phi}[\bar{\rho}_f, \rho_f]$ 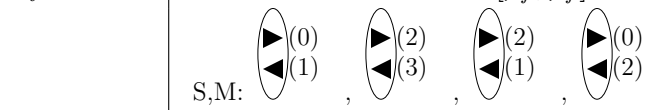
	$\bar{\Phi}[\varphi_f, \rho_f]$ 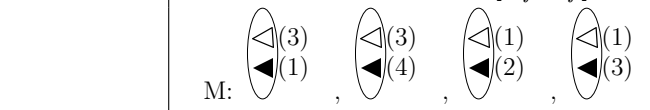
N_t	$\Phi[\rho_r, \varphi_r]$ 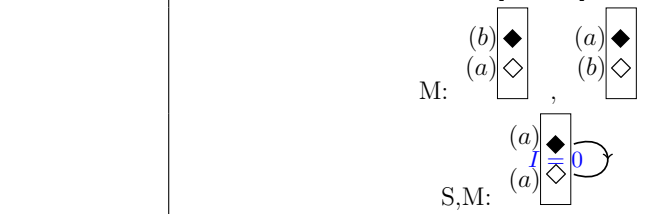
	$\bar{\Phi}[\varphi_r, \rho_r]$ 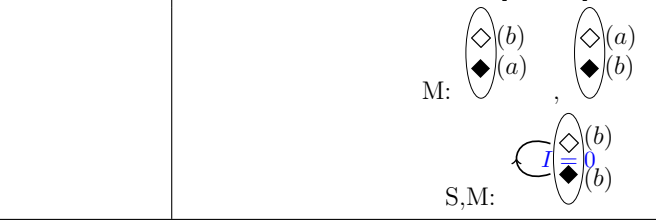

Table 3.2: The Minimal Set of Quarkline End Combinations of Baryons. The combinations required by diagrams consisting multi-hadron operators are marked as 'M' and those that are required by diagrams consisting of single-hadron operators only are marked as 'S'.

# of Time-slices	Quarkline Ends
$N_t^{(\mathrm{snk})}$	$\Phi[\varphi_f, \varphi_f, \varphi_f]$
	$\Phi[\varphi_f, \varphi_f, \varphi_r]$
	$\Phi[\varphi_f, \varphi_r, \varphi_f]$
	$\Phi[\varphi_r, \varphi_f, \varphi_f]$
$N_t^{(\mathrm{src})}$	$\bar{\Phi}[\rho_f, \rho_f, \rho_f]$ 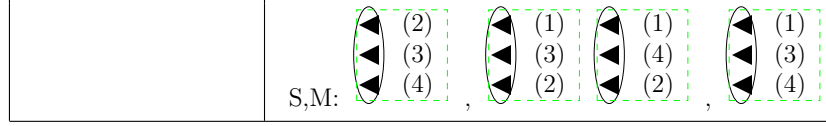

3.5 Implementation and Data Structure

The software in this work is written in C++ and links to the USQCD CHROMA suite based on QDP++ library [54]. Some parts of the computations must be done using the full four-dimensional lattice, but other parts are best handled time-slice by time-slice in three dimensions. QDP++ does not handle both three and four dimensional lattices simultaneously, so the different parts of the computations were done in separate runs using both 3D and 4D versions of the software. Special input/output routines were written to enable 4D QDP++ to read and write 3D time-slices of the lattice.

The computations are carried out as a sequence of tasks for each gauge configura-

tion in the Monte Carlo ensemble. The following quantities are generated and stored in disk in sequence:

- Smeared Gauge Field $\tilde{U}$
  The spatial links of the gauge configuration are smeared using the stout-link procedure. This task is done using a four-dimensional version of our software, but the smeared spatial links are written to disk as individual time-slices suitable for input into the three-dimensional version of our software.

- LapH Eigenvectors V_S^i
  The computation of the Laplacian eigenvectors is done time-slice by time-slice in three dimensions. They are evaluated using a Krylov-Spectral Restarted Lanczos (KSRL) method which is a modification of the thick restarted Lanczos method described in Ref. [55]. Let A denote a Hermitian matrix whose lowest-lying or highest-lying eigenvectors are sought. Given a starting vector u, the KSRL method begins by constructing a Krylov space spanned by vectors $u, Au, A^2u, \ldots, A^mu$. The submatrix of A defined in this basis is then diagonalized, and the eigenvalues and eigenvectors of this submatrix, known as the Ritz values and Ritz vectors, are approximations to those of the full matrix A. Convergence to the exact eigenpairs occurs as the Krylov space dimension increases, but a better procedure is to stop the growth of the Krylov space at some point, typically just above the number of desired eigenpairs, and restart the procedure using a different starting vector or vectors. The use of a certain number of Ritz vectors to restart the procedure is known as Krylov-Spectral restarting. Key issues in the method are determining how many Ritz vectors to use in restarting, determining the size of the Krylov space to use, and maintaining orthogonality of the Lanczos vectors in finite-precision mathematics.

  In this work, either a random vector or the vector whose components are all equal for the starting vector is used. Full global reorthogonalization is used at all steps. The decision to reorthogonalize multiple times is based on a simple criterion [56]: if the norm of the vector decreases by $1/\kappa$, where $\kappa = \sqrt{2}$, then further reorthgonalization is done. A maximum of four reorthogonalizations is enforced. Equation 5 in Ref. [57] is used to choose the number of Ritz vectors to keep, except that the number must be at least as large as the number of converged vectors and cannot exceed the dimension of the Krylov space minus

the number of converged and locked vectors minus twelve. For an approximate eigenvector x (with unit norm) and an estimate λ of its corresponding eigenvalue, the residual norm is defined by $r = ||Ax - \lambda x||$. An eigenpair is considered converged when $r < \texttt{tol}||A||$, where `tol` is the desired tolerance and the matrix 2-norm is defined by $||A|| = \max_{x \neq 0} ||Ax||/||x||$, and can be estimated by the largest absolute value of any Ritz value encountered in the computation.

In calculating the eigenvectors of $\widetilde{\Delta}$, Chebyshev acceleration is used. The eigenvalues of $-\widetilde{\Delta}$ are all real and lie between 0 and some maximum value denoted by λ_L. The goal here is to determine the eigenvectors corresponding to the lowest-lying eigenvalues lying between 0 and some cutoff λ_C. The rate of convergence to solution increases with the spacing between the levels. Convergence is much faster for widely spaced levels. Hence, convergence can be accelerated by transforming the spectrum so that the desired part of the spectrum is more widely spaced. The following transformation is applied first:

$$B = 1 + \frac{2}{(\lambda_L - \lambda_C)}\Big(\widetilde{\Delta} + \lambda_C\Big). \tag{3.42}$$

The above transformation maps the unwanted spectrum to the range $-1 \cdots 1$, and the desired part lies above 1. Chebyshev polynomials are then applied:

$$A = T_n(B). \tag{3.43}$$

Eigenvalues lying between -1 and 1 stay between $-1 \cdots 1$, and the desired eigenvalues above 1 get spaced out to large and widely-separated values above 1. The lowest-lying eigenvalue of $-\widetilde{\Delta}$ becomes the highest-lying eigenvalue of A. Transforming the desired levels to the region above 1 is most convenient since it allows the use of Chebyshev polynomials of any order, both even and odd. The Chebyshev polynomials are applied using the following recurrence relation:

$$\begin{aligned} T_0(x) &= 1, T_1(x) = x, \\ T_n(x) &= 2x\ T_{n-1}(x) - T_{n-2}(x). \end{aligned} \tag{3.44}$$

For calculations done on $\{24^3; 840\}$ and $\{24^3; 860\}$ ensembles, the lowest-lying

$N_v = 112$ eigenvectors are needed on each time-slice. A Krylov space dimension of 160 was found to work well, and $\lambda_L = 15$ and $\lambda_C = 0.5$ were appropriate. Chebyshev polynomials of order 8 were used, and the residual tolerance was set to 10^{-9}. Convergence of all N_v levels occurred within a dozen or less restarts.

The LapH eigenvectors are uniquely determined only to within an overall phase. Given the way in which Z_N noise is injected in the LapH subspace, one sees that a given quark line is not invariant under a change of the phase multiplying each eigenvector (due to the off-diagonal pieces not being exactly zero). It turns out that changing the phase is equivalent to changing the noise by a $U(1)$ phase. This is not a problem, but erroneous results can occur if the original eigenvector files used to determine the quark sinks get deleted and the eigenvectors have to be reconstructed for making the hadrons. With different run parameters, the eigensolver could produce a different phase. The introduction of a phase convention eliminates this potential problem.

The eigenvectors for the different time-slices are then reorganized into four-dimensional eigenvectors corresponding to the different eigenvalues.

- Quark Sinks φ

  Once the needed eigenvectors of the Laplacian are computed and stored, the next step is to compute the quark sinks. The inversions of the Dirac matrix must be done using the full four-dimensional lattice, but the results are written to disk once again as three-dimensional time-slices. Solving $\Omega\phi = V_S\rho^{[d_T SL]}$ (diluted version of Eq. 3.24) for ϕ is accomplished using a mixed-precision improved version of the biconjugate gradient method with even-odd preconditioning. This was found to be the fastest inverter available in Chroma. Occasionally convergence is not achieved, and a slower conjugate gradient solver is applied to the system $\Omega^\dagger\Omega\phi = \Omega^\dagger V_S\rho^{[d_T SL]}$. There are only $N_t N_v$ terms to store for each noise r and each dilution projector d_{TSL}, so storage of these quark propagation coefficients is modest. Disk storage is actually dominated by the LapH eigenvectors. Another nice feature is the fact that the quark propagation coefficients are gauge invariant, as long as the eigenvector phases are handled appropriately.

  It is observed that the correlator estimates and their variances are insensitive to the value of N used for the Z_N noise, as long as N is not too small. It is found that $N = 4$ produced results indistinguishable in quality from those of

larger N. Hence, we use Z_4 noise in this work. The Z_4 noise vector for an ensemble of gauge configurations is identified by a 16-bit unsigned integer s. To create a noise vector $\rho^{(s)}$ for a gauge configuration labeled by an RHMC trajectory number k (assumed to have a value ranging from 0 to $2^{16}-1$), a 32-bit unsigned integer m is first formed in a particular manner using the 16 binary digits of s and the 16 bits of k. Although the procedure of forming m is arbitrary, the same procedure must be used in every instance. The 32-bit unsigned integer m is then taken as a seed to the 32-bit Mersenne twister random number generator which is used to create the Z_4 noise $\rho^{(s)}(t,i,\alpha)$ for each LapH eigenvector, labeled by time t and level i, and for each spin index α. The elements of $\rho^{(s)}$ are generated in a particular order that is always the same. Each Z_4 element is chosen using the sequence of bits obtained from the current state of the Mersenne twister, taking two bits at a time. It was found that the linear congruential generator in QDP++/Chroma is not adequate for generating the Z_4 noise and leads to serious errors in some instances.

There is no need to store the quark sources ρ, since they are very cheap to regenerate. It is noted that $\bar{\varphi}$ and $\bar{\rho}$ can be computed from φ and ρ via Eq. 3.36 and therefore it is not necessary to store them.

- Hadron Operators Φ
  Quark Sinks and Sources are combined into hadron operators Φ using Eq. 3.39 and stored in disk. All hadron operators have definite three-momenta which involve summations over all spatial sites of the lattice, so the resulting hadron sources and sinks are no longer lattice-wide quantities.

- Correlators $C(t)$
  The hadron sinks and sources are assembled in an appropriate way to form the hadron correlation functions. At last the correlation matrices are formed and physical quantities can be extracted using variational method described in Sec. 2.5.1.

Although in principle it is not necessary to keep all the intermediate data before correlators, they are stored in case file corruptions or change of parameters occur.

3.6 Dilution Schemes determined by Small Lattice Simulations [11]

Sec. 2.4 has described the values of the parameters used in the lattices in this work and how they are obtained, summarized in Table 2.4. To implement the Stochastic LapH method, the dilution schemes to be used have to be determined. According to the previous discussion, it is believed that the dependence of the variance on lattice sizes is small. This assertion can be tested by studying the two-point correlators of simple hadron operators on two lattices of different sizes. Such a test on the algorithm using simple nucleon operators was done in previous works. In this work, it is repeated using a simple pion operator $\bar{u}\gamma_5 d$. Fig. 3.9 shows the relative variance in the correlator at time separations $t = 10a_t$ with respect to the gauge limit for different dilution schemes, characterized by the number of inversions per noise seed per source time, N_{inv}, on lattices of sizes $16^3 \times 128$ and $20^3 \times 128$($\{16^3; 840\}$ and $\{20^3; 840\}$ of Table 2.4) for various dilution schemes. Increasing the spatial lattice volume for a fixed eigenvalue cutoff and dilution scheme does lead to some increase in the statistical error. However, it is observed that the scaling behavior of the variance is mild for the dilution schemes under consideration and the difference in errors between the two volumes decreases with higher levels of dilution. It is thus reasonable to expect that the optimal dilution scheme found in a smaller lattice is very likely to be also the one for a larger one. Therefore, various interesting diagrams on the smaller lattice are performed to figure out the dilution schemes to be applied to other more realistic lattices in the next chapter. Since strange quark lines should behave similar to light quark lines as far as dilution schemes are concerned, the conclusions obtained here are assumed to also apply for strange quark lines.

3.6.1 Isovector Simulations

From the simulation of the pions, one can also determine an optimal Fixed Dilution Scheme to be used in the realistic runs. According to Fig. 3.9, the gauge noise limit is almost reached($\sigma/\sigma_g = 1.58$) at $N_{\text{inv}} = 32$, corresponding to dilution scheme [TF, SF, LI8] which is thus chosen to be the Fixed Dilution Scheme. Fig. 3.10 shows the pion correlator at this scheme. It is observed that there is almost no difference in variance between this scheme and the full dilution scheme. This conclusion coincides

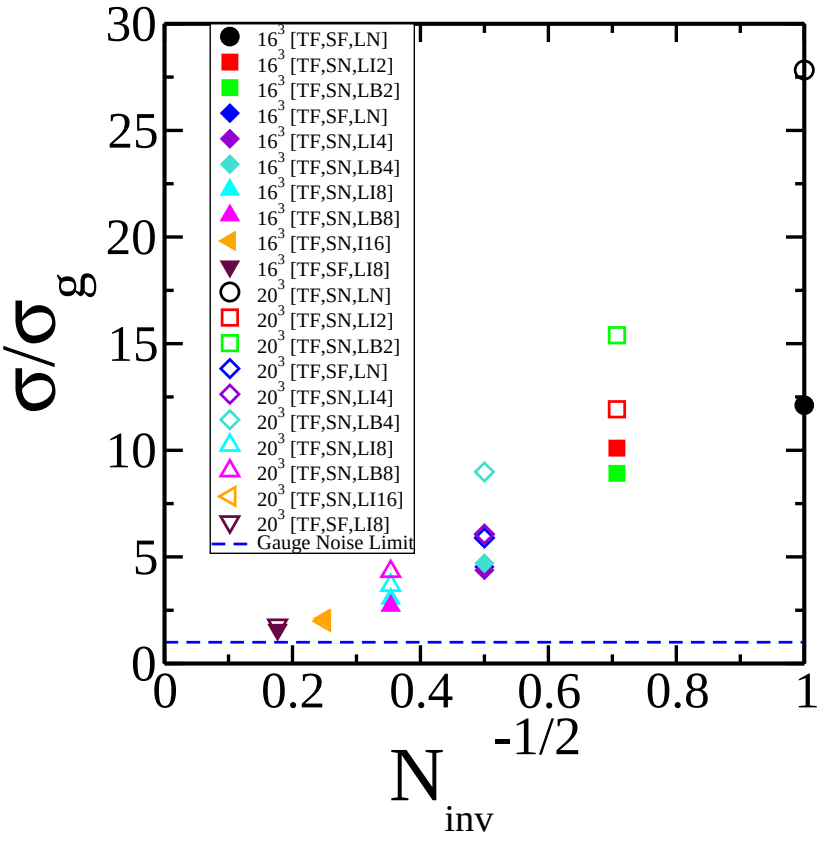

Figure 3.9: Comparison between lattices of two volumes $16^3 \times 128$(solid symbols) and $20^3 \times 128$(hollow symbols) at various dilution schemes. $N_v = 32$ for the former and $N_v = 64$ for the latter to keep the cutoff eigenvalues the same. It is observed that the blocked and interlaced dilution schemes with the same N_{inv} are comparable. In order to reduce correlations between consecutive dilution indices, an interlaced dilution scheme is more preferable to blocked ones. Therefore some blocked dilution schemes are not shown here.

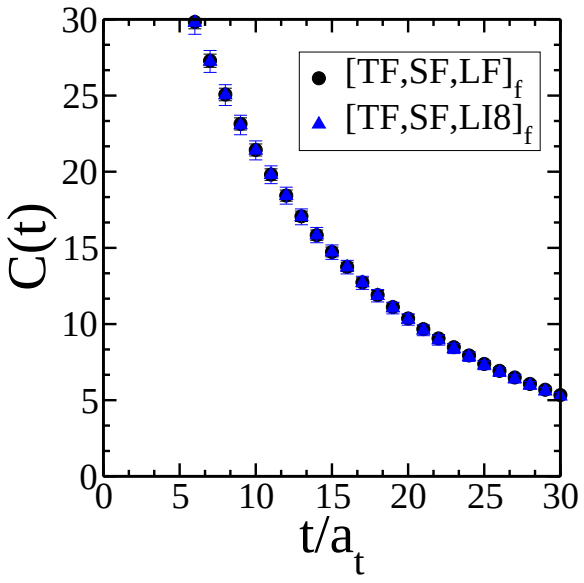

Figure 3.10: Pion Correlator at the chosen fixed dilution scheme

with the previous tests done with nucleons [10] and therefore the same Fixed Dilution Scheme is to be used in both mesons and baryons.

It is remarkable that the N_{inv} required in this scheme is only 8.33% of that in an exact treatment, in which $N_{\text{inv}} = N_v \times N_D \times N_c = 32 \times 4 \times 3 = 384$ is needed. The computational resources required are therefore dramatically reduced while keeping the variance comparable to the exact treatment. This reduction would become more dramatic if the lattice size is increased, in which case N_{inv} stays the same for the stochastic estimation due to the insensitivity of suitable dilution scheme to lattice sizes, while N_{inv} in the exact treatment scales linearly with lattice sizes.

3.6.2 Isoscalar Simulations

In order to determine an optimal Relative Dilution Scheme, a test on the light quark contribution of isoscalars is performed. Their 2-point (VEV subtracted) correlators

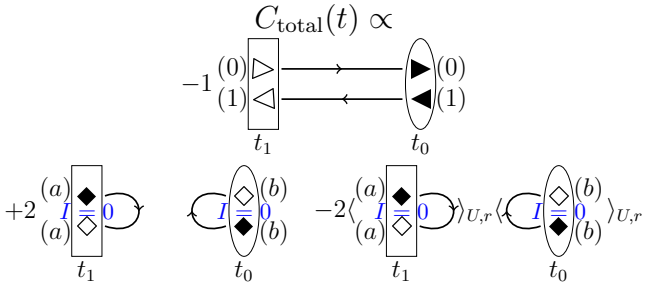

Figure 3.11: Diagrams in VEV subtracted Correlators of isoscalars(light quark contribution only). The first row corresponds to the 'Forward' Diagram $C_{\text{fwd}}(t)$ and the second row corresponds to the 'Same-time' diagram $C_{\text{smt}}(t)$.

consist of two parts after Wick contractions. Suppressing irrelevant indices,

$$
\begin{aligned}
C_{\text{total}}(t) &= (\bar{u}u + \bar{d}d)(t_1)(\bar{u}u + \bar{d}d)(t_0) - \text{VEV} \qquad (3.45)\\
&= \bar{u}u(t_1)\bar{u}u(t_0) + \bar{d}d(t_1)\bar{d}d(t_0) + \bar{u}u(t_1)\bar{d}d(t_0) + \bar{d}d(t_1)\bar{u}u(t_0) - \text{VEV}\\
&\propto \left\langle -\Phi^{\Lambda}[\bar{\varphi}_f^{l(r_0)}, \varphi_f^{l(r_1)}]_{d_0 d_1}(\vec{0}, t_1)\bar{\Phi}^{\bar{\Lambda}}[\bar{\rho}_f^{\bar{l}(r_0)}, \rho_f^{\bar{l}(r_1)}]_{d_0 d_1}(\vec{0}, t_0)\right\rangle_{U,r}\\
&+ \left\langle 2\Phi^{\Lambda}[\bar{\varphi}_r^{l(r_a)}, \varphi_r^{l(r_a)}]_{d_0 d_0}(\vec{0}, t_1)\bar{\Phi}^{\bar{\Lambda}}[\bar{\rho}_r^{\bar{l}(r_b)}, \rho_r^{\bar{l}(r_b)}]_{d_1 d_1}(\vec{0}, t_0)\right\rangle_{U,r}\\
&- 2\left\langle \Phi^{\Lambda}[\bar{\varphi}_r^{l(r_a)}, \varphi_r^{l(r_a)}]_{d_0 d_0}(\vec{0}, t_1)\right\rangle_{U,r}\left\langle \bar{\Phi}^{\bar{\Lambda}}[\bar{\rho}_r^{\bar{l}(r_b)}, \rho_r^{\bar{l}(r_b)}]_{d_1 d_1}(\vec{0}, t_0)\right\rangle_{U,r}\\
&\equiv C_{\text{fwd}}(t) + C_{\text{smt}}(t),
\end{aligned}
$$

in which the first diagram C_{fwd} without same-time quark lines is referred to as 'Forward' diagram and the second (VEV-subtracted) diagram C_{smt} that only involves same-time quark lines is referred to as 'Same-Time' diagram. Fig. 3.11 shows the diagrams involved. The first row corresponds to the $C_{\text{fwd}}(t)$ and the second row corresponds to $C_{\text{smt}}(t)$. Since the focus of this test is on the same-time quark lines but not the full correlator, $C_{\text{fwd}}(t)$ is ignored here. The pseudoscalar(PS) and scalar(S) channels are investigated.

The ground state of the pseudoscalar channel corresponds to the η meson in experiments. The operator used in this channel is a simple $\bar{l}\gamma_5 l$ operator(l is either u or d), which couples to the light quark portion of η as the lowest energy state. It is known that the RHMC algorithm suffers from a bias of sampling in topological sectors, resulting in a finiteness of topological charge [58]. Therefore a VEV is induced

in this channel, but it is also known to be small and is therefore ignored in this test. In serious computations, it has to be subtracted.

Fig. 3.12 shows the dilution scheme dependence of the relative variance with respect to the gauge noise limit in the same-time contribution of the PS correlator on $\{12^3; 743\}$ lattice. It is observed that most dilution schemes under consideration give acceptable results. Therefore the Relative Dilution Scheme can be any of them. In order to pin down a dilution scheme that also works for most isoscalar operators, the noisiest channel, the scalar channel, is computed.

In the scalar channel, a vacuum expectation value(VEV) exists in the correlator as described in Sec. 2.5.1. It is expected to be the noisiest channel because of the VEV subtraction that extracts relatively small values from large and fluctuating VEVs. It is thus believed that an applicable dilution scheme for the isoscalar scalars would work for most hadrons. The simple operator $\bar{l}l$ is used in this test. This operator couples to the light quark portion of f_0 (also called σ) meson as the lowest energy state. Fig. 3.14 shows the dilution scheme dependence of the relative variance with respect to the gauge limit in the same-time contribution of the VEV-subtracted S correlator on $\{12^3; 743\}$. It is observed that [FI12,SF,LI4] is an acceptable scheme.

Although [TI12,SF,LI4] is good enough on $\{12^3; 743\}$ lattice, the temporal size of larger lattices are not divisible by 12. Moreover, it is expected that the optimal LapH dilution scheme should be the same for both Fixed and Relative Schemes. After all, using a higher dilution scheme does more good than harm as long as computational resources allow. In conclusion, the Relative Dilution Scheme on larger lattices is taken to be [TI16,SF,LI8] in this work.

Fig. 3.13 and 3.15 show the correlators at [TI16,SF,LI8] compared with the gauge noise limit. It is found that the variance is not significantly increased, while the cost of computation is greatly reduced. For both channels, $N_{\text{inv}} = 16 \times 4 \times 8 = 512$ for the stochastic method, which is only 3.125% of $N_{\text{inv}} = 128 \times 4 \times 32 = 16384$ required by the exact treatment.

3.6.3 Multi-Hadron Simulations

Since one of the main motivations of computing same-time quark lines is to obtain correlators that consist of multi-hadron operators, it is essential to check if the dilution schemes chosen are also applicable to correlators with multihadron operators. Here

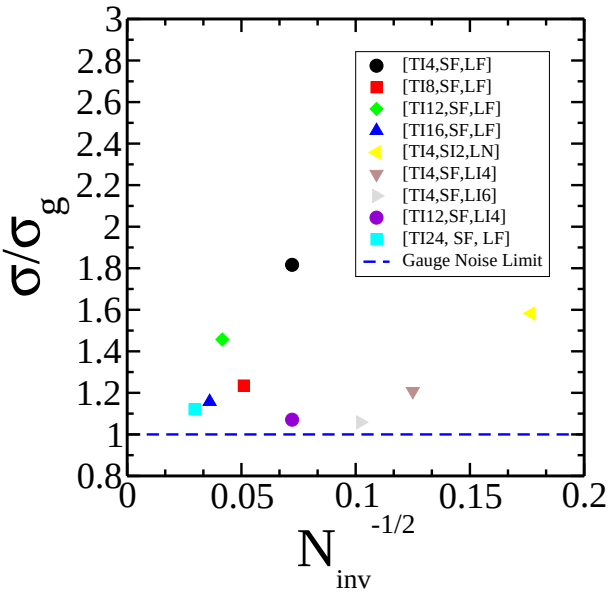

Figure 3.12: Isoscalar PS channel at different relative dilution schemes on $\{12^3; 743\}$ ensemble with $N_v = 12$. It is observed that the variance decreases with the number of dilution projectors.

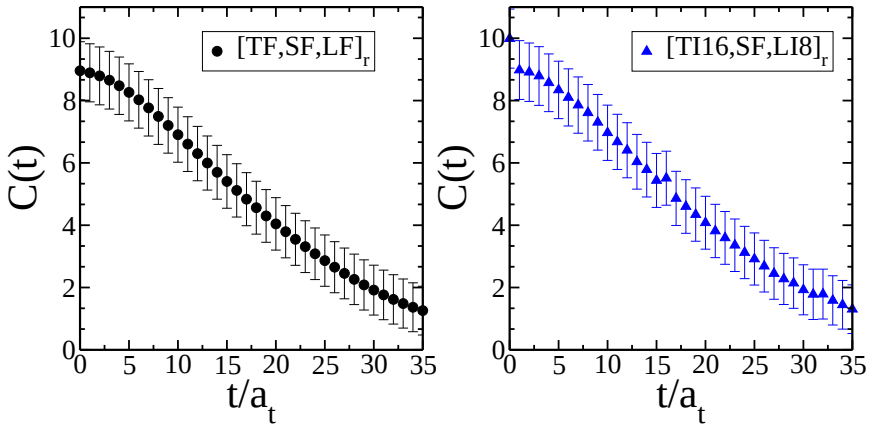

Figure 3.13: Same-time diagram contribution of PS channel Correlator at the chosen dilution scheme on $\{16^3; 840\}$ ensemble, compared with the gauge noise limit (left plot). There are 52 configurations with separation $n_{\text{sep}} = 40$ trajectories.

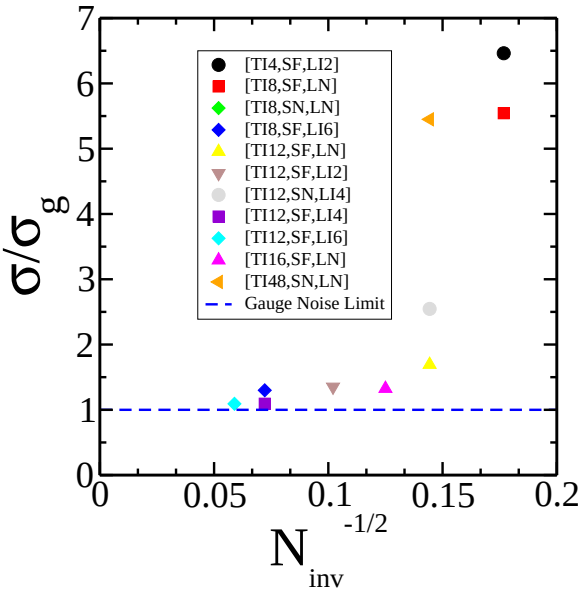

Figure 3.14: Isoscalar S channel at different dilution schemes on $\{12^3; 743\}$ ensemble.

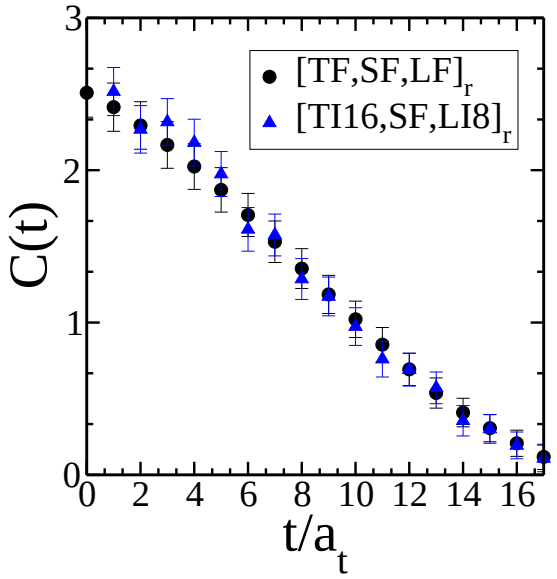

Figure 3.15: Same-time diagram Contribution of S channel Correlator at the chosen dilution scheme $\{16^3; 840\}$ ensemble, compared with the gauge noise limit. There are 52 configurations with separation $n_{\text{sep}} = 40$ trajectories.

two useful and interesting cases are considered to demonstrate the quality of the signals one can obtain from the algorithm using the chosen dilution schemes. The first case is a ρ meson correlated with two pions and the other case is a 4-point correlation function of pions.

These two correlators are interesting because the ρ meson decay width and two-pion scattering phase shifts can be obtained from them. Also, the states extracted from the diagonalization of the correlator matrix composed of these correlators are the simplest and lowest-lying ones that take into account the contributions of multi-hadron operators. It is the first step towards a full hadron spectrum with states that mix with multi-hadrons.

Since the quark masses of the light quarks are taken to be identical, isospin is conserved on the lattice. Therefore one can classify two-pion scatterings in terms of the value of the isospins. The channels that acquire the lowest few energies are the $I = 0, 1, 2$ channels. In this work only these channels are considered. Since the energy is the same for different I_3's within the same I, only one I_3 is used for each channel. The two-pion operators are defined as follows(suppressing the spin and displacement structure within the pions):

$$\bar{\pi}_+ \equiv \bar{u}d, \bar{\pi}_0 \equiv \frac{1}{\sqrt{2}}(\bar{d}d - \bar{u}u), \bar{\pi}_- \equiv -\bar{d}u, \tag{3.46}$$

$$\begin{aligned}
&I = 0: \\
&\quad \bar{O}^{I=0}_{\pi\pi} \equiv c^{\Lambda}_{I=0}(\vec{p}_0, \vec{p}_1)\left[\bar{\pi}_+(\vec{p}_0)\bar{\pi}_-(\vec{p}_1) - \bar{\pi}_0(\vec{p}_0)\bar{\pi}_0(\vec{p}_1) + \bar{\pi}_-(\vec{p}_0)\bar{\pi}_+(\vec{p}_1)\right] \\
&I = 1: \\
&\quad \bar{O}^{I=1}_{\pi\pi} \equiv c^{\Lambda}_{I=1}(\vec{p}_0, \vec{p}_1)\left[\bar{\pi}_+(\vec{p}_0)\bar{\pi}_0(\vec{p}_1) - \bar{\pi}_0(\vec{p}_0)\bar{\pi}_+(\vec{p}_1)\right] \\
&I = 2: \\
&\quad \bar{O}^{I=2}_{\pi\pi} \equiv c^{\Lambda}_{I=2}(\vec{p}_0, \vec{p}_1)\left[\bar{\pi}_+(\vec{p}_0)\bar{\pi}_+(\vec{p}_1)\right],
\end{aligned}$$

in which the multi-hadron operator coefficients $c^{\Lambda}_I(\vec{p}_0, \vec{p}_1)$ specify how different momenta are combined to give multi-hadron operators corresponding to the collective index Λ. In the following tests, these coefficients are taken to be simple S-Waves with zero relative momenta for $I = 0, 2$ and P-Wave with minimum back-to-back (on-axis)

momenta for $I = 1$, i.e.

$$
\begin{aligned}
c^{\Lambda}_{I=0}(\vec{p}_0, \vec{p}_1) &\equiv P^0(1)\delta_{\vec{p}_0,\vec{0}}\delta_{\vec{p}_1,\vec{0}} \\
c^{\Lambda}_{I=1}(\vec{p}_0, \vec{p}_1) &\equiv \frac{1}{3}\sum_{\hat{n}=\hat{x}_1,\hat{x}_2,\hat{x}_3} P^1(\hat{p}_0\cdot\hat{n})\delta_{\vec{p}_0,-\vec{p}_1}\delta_{|\vec{p}_1|,2\pi/N_s} \\
c^{\Lambda}_{I=2}(\vec{p}_0, \vec{p}_1) &\equiv P^0(1)\delta_{\vec{p}_0,\vec{0}}\delta_{\vec{p}_1,\vec{0}},
\end{aligned}
\tag{3.47}
$$

where $P^l(x)$ are the Legendre Polynomials.

In order to study two-pion scatterings, the 4-point correlator of pions(or equivalently, 2-point functions of $O^I_{\pi\pi}$'s) are needed and a lot of diagrams are involved.(Fig. 3.16) These diagrams are classified into three types: without same-time quark lines ('Forward'), with both types of quark lines ('Box'), and with same-time quark lines only('Same-Time'). As far as dilution schemes are concerned, the behavior of the first type should resemble that of isovectors while the behavior of the third type should resemble the isoscalars. Therefore the focus of this section is the 'Box' diagram. A more detailed and careful discussion of the full correlator will be discussed in Ch. 4.

Fig. 3.19 shows the contribution of the box diagram in the 4-point correlator of pions relatively at rest. It is found that $\sigma/\sigma_g \approx 1.08$(at $t = 10a_t$). It is remarkable that approximately the gauge noise limit is reached at 15.8% of the cost of exact inversions. $N_{\text{inv}} = (16+3)\times 4\times 8 = 608$ is required in the stochastic method while $N_{\text{inv}} = 30\times 4\times 32 = 3840$ (if $N_t^{(\text{snk})} = 30$) in the exact treatment.

The diagrams involved in the ρ-$\pi\pi$ system are shown in Fig. 3.17. In this test, a ρ_k meson is represented by a simple operator $-\bar{d}\gamma_k u$, in which $k = 1, 2, 3$ is the spatial direction. Due to the spatial isotropy of the lattice, the behaviors of all these three directions should be the same. In serious runs, the correlators should be averaged over these directions to boost statistics. However, since they are the same, it suffices to compute one of them in this test. The ρ_3 meson is chosen here.

Fig. 3.18 shows the correlator of a ρ_3 meson at t_0 correlated with a P-Wave $I = 1$ combination of two pions at t_1. Since different rows of an ireducible representation are orthogonal to one another, only the $\hat{n} = \hat{x}_3$ term in the P-Wave actually contributes. It is observed that the variance is significantly larger than the gauge noise limit, but still moderate. The ratio $\sigma/\sigma_g \approx 3.98$(at $t = 10a_t$) is still small compared with the cost reduction of 85% from $N_{\text{inv}} = 30\times 4\times 32 = 3840$(say $N_t^{(\text{snk})} = 30$ sink time-slices are needed) to $N_{\text{inv}} = (16+2)\times 4\times 8 = 576$.

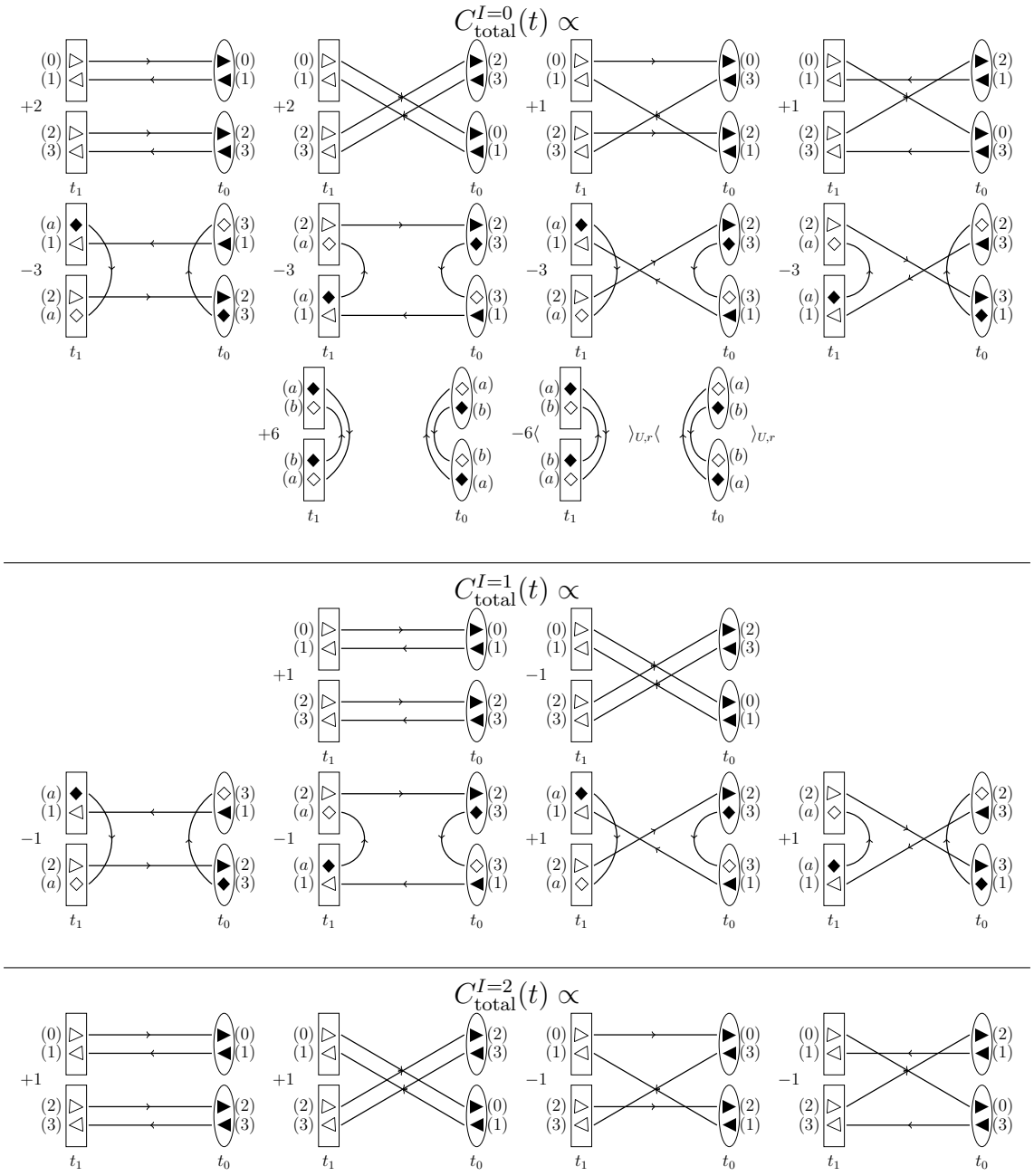

Figure 3.16: Diagrams in 4-point (VEV subtracted) correlators of pions in $I = 0, 1, 2$ channels. The combination of the first row corresponds to the 'Forward' contribution $C^I_{\text{fwd}}(t)$, that in the second row(if exists) corresponds to the 'Box' contribution $C^I_{\text{box}}(t)$ and that in the third row(if exists) corresponds to the 'Same-time' contribution $C^I_{\text{smt}}(t)$.

Strictly speaking, the comparison of computational resources above is not completely fair, since if same-time inversions on $\sim$ 30 time-slices were available in the exact method, the number of t_0's would have gone from 4 to 30 in order to fully utilize the available data without extra inversions. σ(and hence $\sigma_{\rm g}$) would then decrease by a factor of approximately $(4/30)^{1/2} = 36.5\%$, although the true factor would be slightly less than that due to the autocorrelation between time-slices within each configuration. This means one could have achieved a smaller absolute variance if the exact method could be employed. However, the same boost in statistics can be performed in the stochastic method as well, by increasing the number of t_0's from 4 to 30 in the same way. Even if such boost is performed in the stochastic method, the number of inversions required only increases by a factor of $30/4 \approx 7.5$. Since permutation of noise seeds can be employed to fully utilize the inversions so that some number of t_0's can be omitted (assuming the effect of 1 permutation is close to increasing t_0 by 1), this factor can be reduced by 2 in the ρ-$\pi\pi$ system and 4 in the two-pion 'Box' diagram. It is expected that after these boosts and improvements, the variance is again close to the new gauge noise limit because they share the same new reduced σ_g(36.5% of the original one). In this 'fair' comparison, the number of inversions required by the stochastic method is still much smaller than that in the exact method by $100\% - 15\% \times 7.5/2 = 43.75\%$ and $100\% - 15.8\% \times 7.5/4 = 70.4\%$ in these two cases respectively. More importantly, it is actually impractical to employ the exact method in larger lattices due to the limitation of computational resources. On those larger lattices, the stochastic estimation is the only plausible way to carry out such calculations.

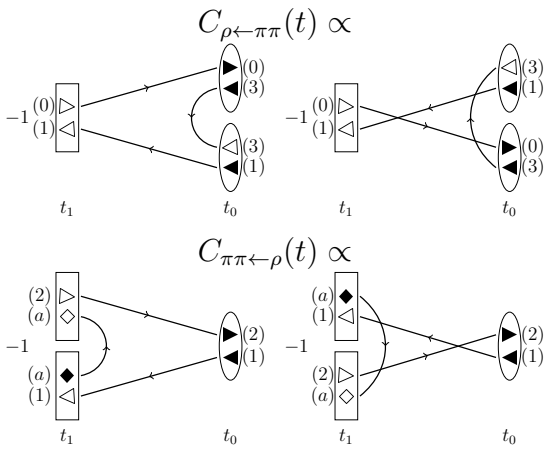

Figure 3.17: Diagrams involved in the ρ-$\pi\pi$ system

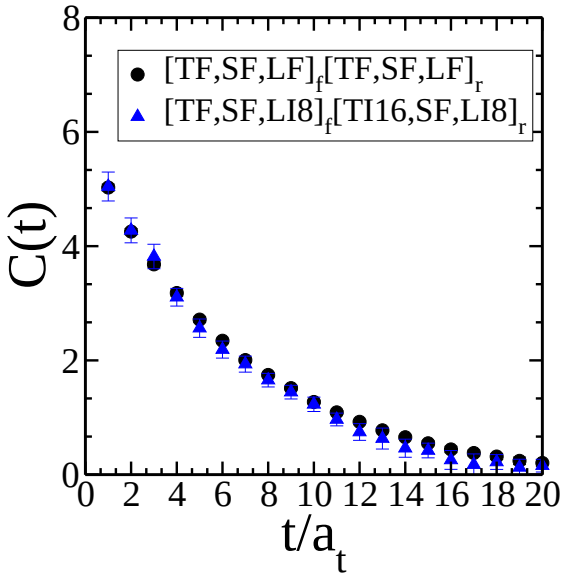

Figure 3.18: $\rho \to \pi\pi$ Correlator on $\{16^3; 840\}$ ensemble, compared with the gauge noise limit. There are 52 configurations with separation $n_{\text{sep}} = 40$ trajectories.

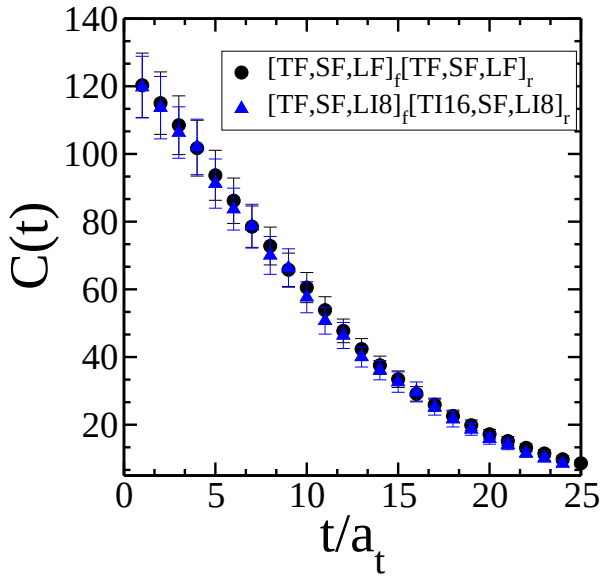

Figure 3.19: 'Box' diagram contribution that will be required by the correlator of the two-pion scattering in $I = 0, 1$ channels on $\{16^3; 840\}$ ensemble, compared with the gauge noise limit. There are 52 configurations with separation $n_{\rm sep} = 40$ trajectories.

Chapter 4

First Applications on Realistic Lattices [10]

Equipped with the optimal dilution schemes that are shown to work in small lattices, one can apply them to more realistic lattices. To prepare for the coming studies, some basic calculations are done on lattices with size $24^3 \times 128$, bare strange quark mass parameter $m_s = -0.0743$, and bare light quark mass parameters $m_l = -0.0840$ and $m_l = -0.0860$, i.e. $\{24^3; 840\}$ and $\{24^3; 860\}$ in Table 2.4. These include scale determinations, simulations of simple hadrons and a revisit of isoscalars and multi-hadron systems.

4.1 Scale Determination

As described in Sec. 2.4, one needs to determine the lattice sizes on the lattice in order to make claims about physical quantities in physical units. This is done by investigating the mass of Ω. Thus this particle is computed to set such scale. Fig. 4.1 shows the results of ensembles $\{24^3; 840\}$ and $\{24^3; 860\}$. There are 551 configurations in $\{24^3; 840\}$ ensemble and 584 configurations in $\{24^3; 860\}$ ensemble. Consecutive configurations are separated by $n_{\text{sep}} = 20$ RHMC trajectories. Four widely-separated t_0's are used on each configuration. The first column shows the correlators $C(t)$, the second column shows the corresponding effective masses m_{eff} and the third one shows the t_{min} plots. The blue lines and points are the chosen range of fit. The experimental mass of Ω is found to be $m_\Omega^{\text{exp}} = 1.67245(29)$ GeV. By equating $m_\Omega = m_\Omega^{\text{exp}}$, it is found that $a_t^{-1} = 5.661(17)$ GeV and $a_t^{-1} = 6.015(17)$ GeV

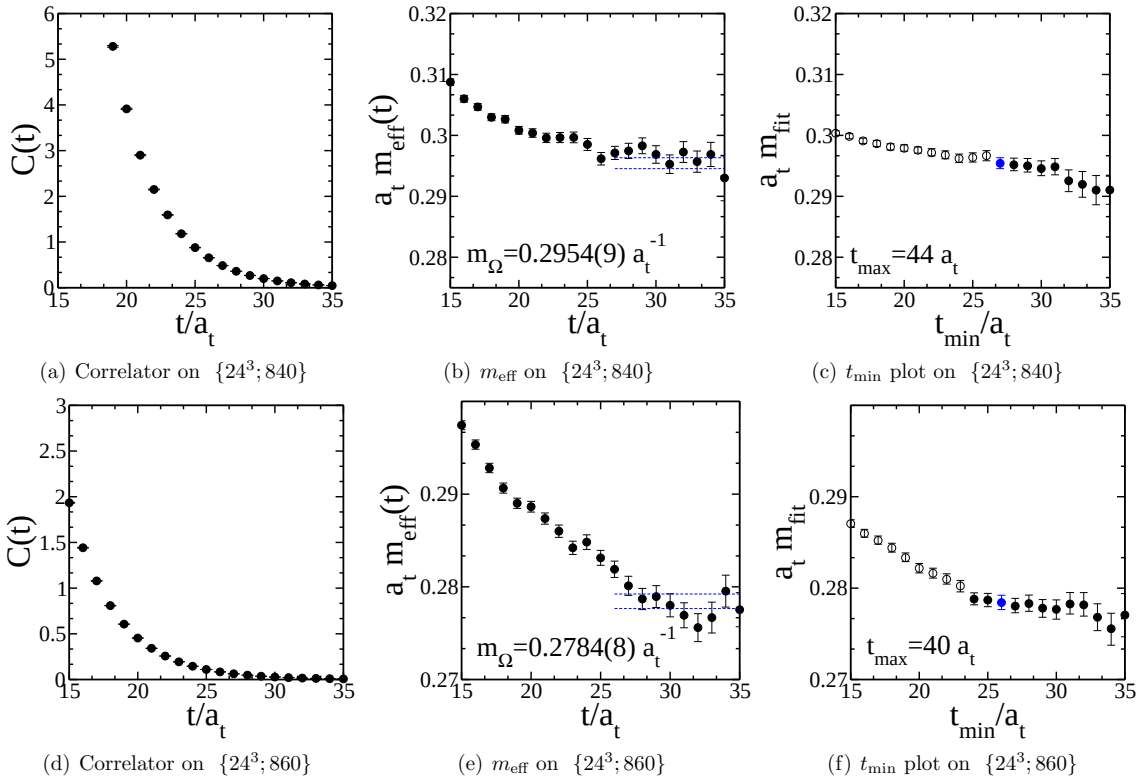

(a) Correlator on $\{24^3; 840\}$ (b) m_{eff} on $\{24^3; 840\}$ (c) $t_{\min}$ plot on $\{24^3; 840\}$

(d) Correlator on $\{24^3; 860\}$ (e) m_{eff} on $\{24^3; 860\}$ (f) $t_{\min}$ plot on $\{24^3; 860\}$

Figure 4.1: Ω Simulation on $\{24^3; 840\}$ and $\{24^3; 860\}$ ensembles. There are 551 configurations in $\{24^3; 840\}$ ensemble and 584 configurations in $\{24^3; 860\}$ ensemble. Consecutive configurations are separated by $n_{\text{sep}} = 20$ RHMC trajectories. Four widely-separated t_0's are used on each configuration. $\Delta t = 3a_t$ in the m_{eff} plots.

for $\{24^3; 840\}$ and $\{24^3; 860\}$ respectively. According to Sec. 2.2, the anisotropy parameter $\xi \approx 3.5$. Therefore, using 1 GeV$^{-1}\hbar c = 0.197$fm, $a_s \approx 0.12$fm and $a_s \approx 0.11$fm correspondingly.

4.2 Pions and Nucleons

The simplest hadrons that can be obtained are the pions and nucleons. As the first step towards more complicated operators, the 2-point correlators of them are computed to study the quality of the best signals.

Figs. 4.2 and 4.3 show the results of nucleons and pions respectively. The correlators give accurate signals and the $t_{\min}$ plots show stable plateaus. Using the a_t^{-1} found in previous section, it is found that $m_N = 1.1781(58)$ GeV and $m_\pi = 0.3911(14)$ GeV

on $\{24^3; 840\}$ ensemble and $m_N = 1.048(14)$ GeV and $m_\pi = 0.2439(20)$ GeV on $\{24^3; 860\}$ ensemble.

The $\{24^3; 840\}$ ensemble was examined in previous works [15, 17] using the exact treatment of inversions. The masses of Ω, π and N obtained in this work not only resembles the results in those works, but also maintains a comparable variance. It is remarkable that the computational resources used in this work is only a tiny fraction of the latter. This again verifies that the stochastic estimation is an important trick in making the calculation much more efficient.

Fig. 4.4 shows the nucleon and Ω masses against $(m_\pi/m_\Omega)^2$ together with results from previous works. It is encouraging that fitting the three leftmost Ω points to a form linear in $(m_\pi/m_\Omega)^2$ and fitting the three leftmost nucleon points to an empirical form linear in m_π/m_Ω yields $m_N/m_\Omega \approx 0.556$ at the physical value of m_π/m_Ω, which compares well with the observed 0.561 value.

4.3 Isoscalars

In this section, the full correlators of simple isoscalars are calculated to demonstrate that good signals can be obtained on realistic lattices. Again, the goal here is only to test the feasibility of the algorithm. Only the simple single-site operators used on $\{16^3; 840\}$ are used and strange quark contributions are ignored. Therefore the masses from the fits here are only preliminary values and do not necessarily correspond to the ground state of the specified channels.

Pseudoscalar (PS) Channel

Fig. 4.5 shows the results of the pseudoscalar channel. The operator used here is $\bar{l}(1-\gamma_4)\gamma_5 l$, which couples to the light quark portion of η as the lowest energy state. As mentioned before, it is known that the topological sectors may not be properly sampled in Monte Carlo simulations. This gives rise to a finite VEV in this channel but it vanishes with increasing lattice sizes [59, 60]. This VEV is found to be small so is ignored in this test. However, in serious computations, it has to be taken into account to get an accurate estimation.

The 'Forward'('fwd') diagram $C_{\text{fwd}}(t)$ corresponds to the isovector counterpart, i.e. pions. Since the mass of pion has already been estimated with higher statistics in last section, it is not estimated again here. The mass of (light-quark-only) η is found

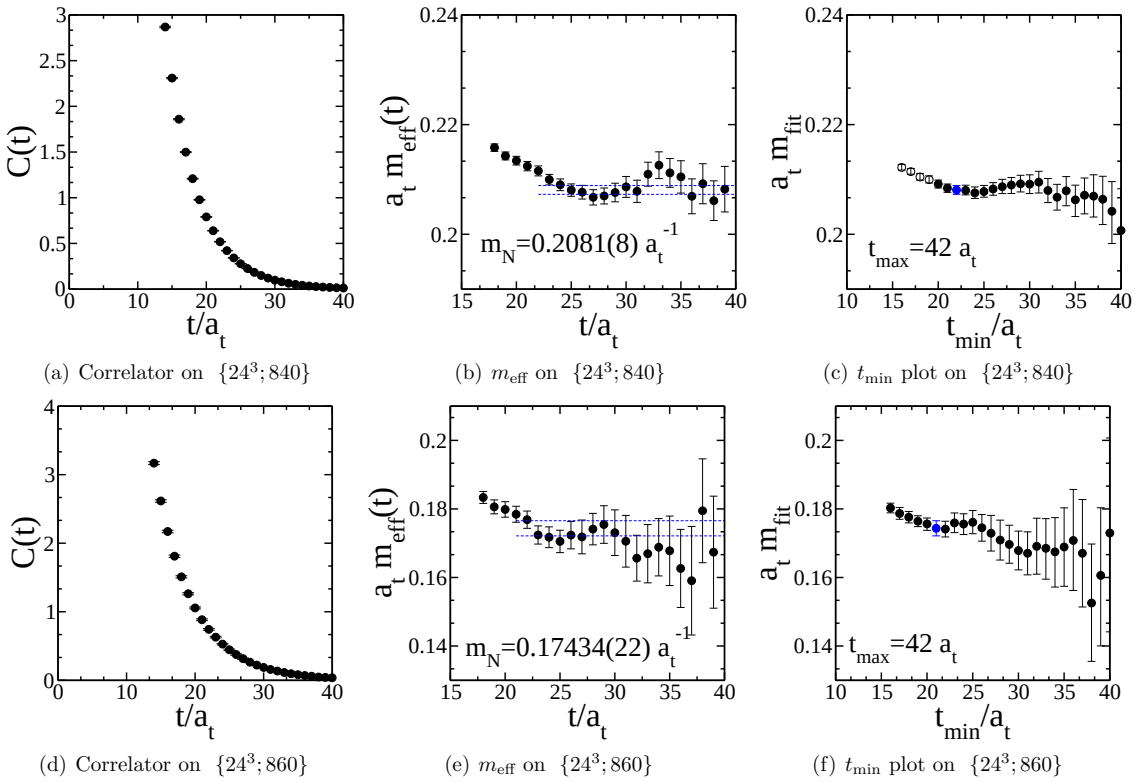

(a) Correlator on $\{24^3; 840\}$ (b) m_{eff} on $\{24^3; 840\}$ (c) t_{min} plot on $\{24^3; 840\}$

(d) Correlator on $\{24^3; 860\}$ (e) m_{eff} on $\{24^3; 860\}$ (f) t_{min} plot on $\{24^3; 860\}$

Figure 4.2: Nucleon on $\{24^3; 840\}$ and $\{24^3; 860\}$ ensembles. There are 551 configurations in $\{24^3; 840\}$ ensemble and 584 configurations in $\{24^3; 860\}$ ensemble. Consecutive configurations are separated by $n_{\text{sep}} = 20$ RHMC trajectories. Four widely-separated t_0's are used on each configuration. $\Delta t = 3a_t$ in the m_{eff} plots.

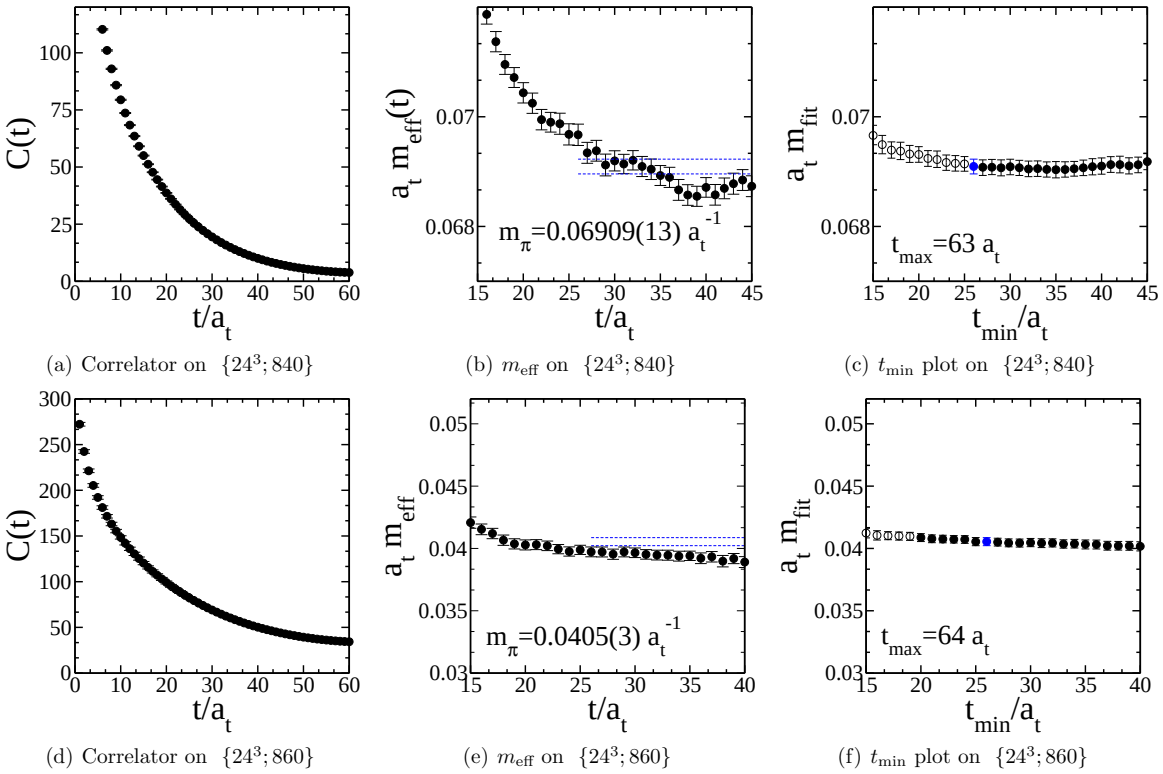

(a) Correlator on $\{24^3; 840\}$ (b) m_{eff} on $\{24^3; 840\}$ (c) t_{min} plot on $\{24^3; 840\}$

(d) Correlator on $\{24^3; 860\}$ (e) m_{eff} on $\{24^3; 860\}$ (f) t_{min} plot on $\{24^3; 860\}$

Figure 4.3: π on $\{24^3; 840\}$ and $\{24^3; 860\}$ ensembles. There are 551 configurations in $\{24^3; 840\}$ ensemble and 584 configurations in $\{24^3; 860\}$ ensemble. Consecutive configurations are separated by $n_{\text{sep}} = 20$ RHMC trajectories. Four widely-separated t_0's are used on each configuration. $\Delta t = 3a_t$ in the m_{eff} plots.

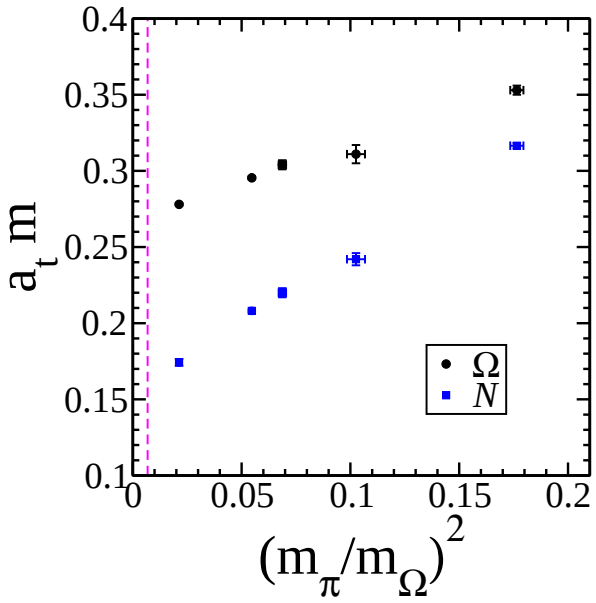

Figure 4.4: Nucleon and Ω masses against $(m_\pi/m_\Omega)^2$ for fixed $\beta = 1.5$, $m_s = -0.0743$ and varying m_l. The two leftmost points for each baryon are from this work and the others are from Ref. [17]. The vertical dashed line indicates the physical value of $(m_\pi/m_\Omega)^2$.

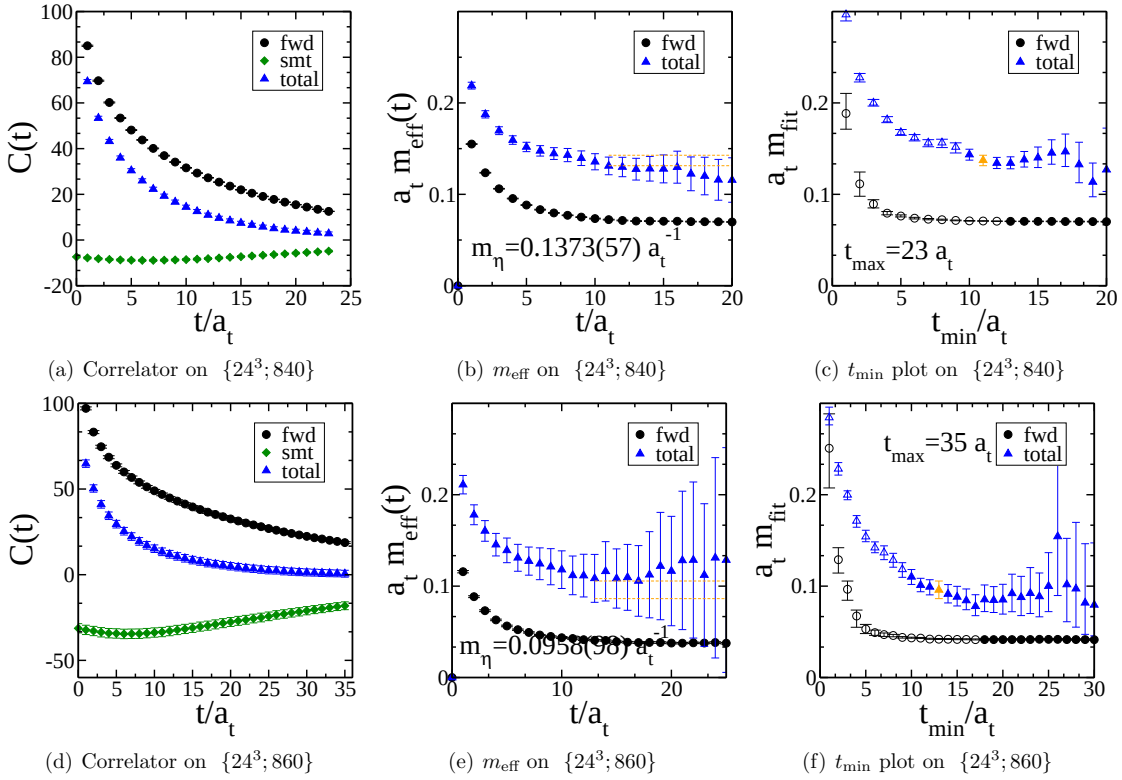

(a) Correlator on $\{24^3;840\}$ (b) m_{eff} on $\{24^3;840\}$ (c) t_{min} plot on $\{24^3;840\}$

(d) Correlator on $\{24^3;860\}$ (e) m_{eff} on $\{24^3;860\}$ (f) t_{min} plot on $\{24^3;860\}$

Figure 4.5: PS channel on $\{24^3;840\}$ and $\{24^3;860\}$ ensembles. There are 210 configurations for $\{24^3;840\}$ ensemble and 198 configurations for $\{24^3;860\}$ ensemble, both with $n_{\text{sep}} = 40$ trajectories. 'fwd' represents the Forward diagram and 'smt' represents the Same-Time diagram. $\Delta t = 3a_t$ in the m_{eff} plots.

to be $m_\eta = 777(42)$ MeV and $m_\eta = 576(59)$ MeV on $\{24^3;840\}$ and $\{24^3;860\}$ ensembles respectively. Although the operators used here do not contain the strange quark field, the fact that the value on $\{24^3;860\}$ is consistent with the experimental value of $m_\eta^{\text{exp}} = 547.853(24)$ MeV is encouraging.

Scalar (S) Channel

Fig. 4.6 shows the result of the scalar channel. The operator used is a single hadron operator $\bar{l}l$, which is experimentally known as f_0 (or σ). However, it is believed that the lowest-lying level is mixed with an $I = 0$ channel S-wave two-pion state in experiments. The lattices under consideration are large enough to allow such mixing to occur. This means a single-hadron operator can only poorly couple to the ground state, resulting in a noisy signal with heavy contamination from first excited state even at large time separation as seen in the figure. Since this test is not intended to

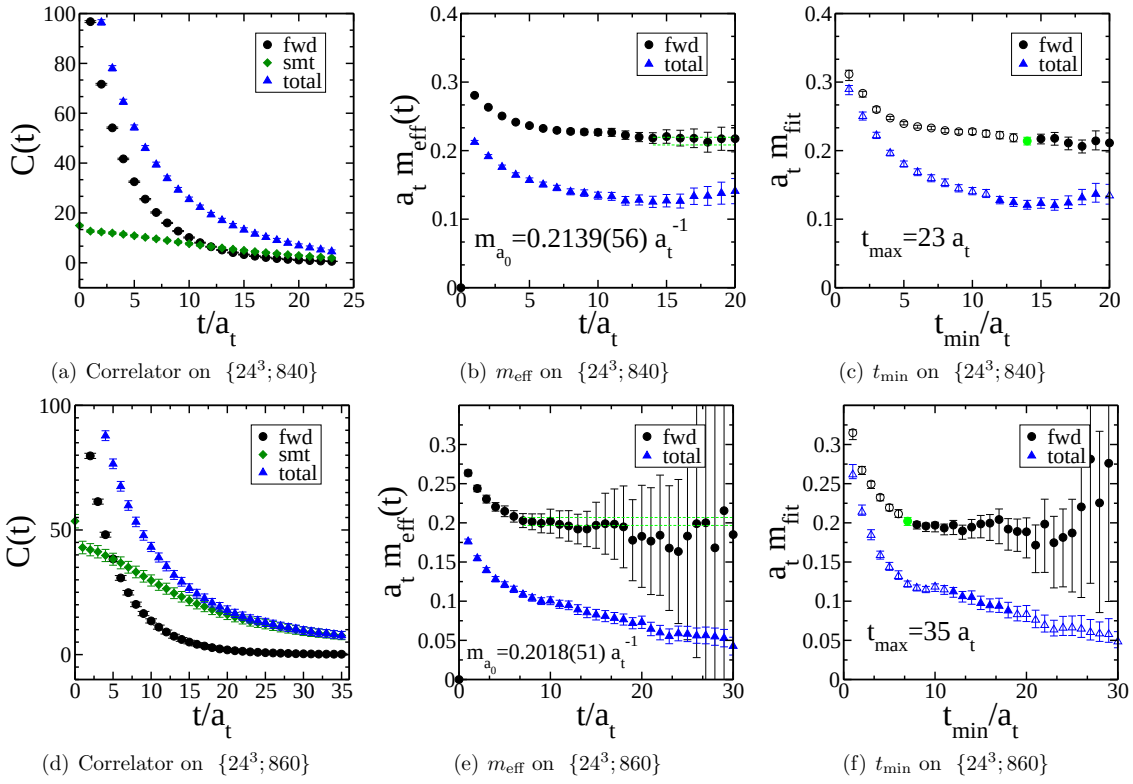

(a) Correlator on $\{24^3;840\}$ (b) m_{eff} on $\{24^3;840\}$ (c) t_{min} on $\{24^3;840\}$

(d) Correlator on $\{24^3;860\}$ (e) m_{eff} on $\{24^3;860\}$ (f) t_{min} on $\{24^3;860\}$

Figure 4.6: S channel on $\{24^3;840\}$ and $\{24^3;860\}$ ensembles (VEV-subtracted). There are 135 configurations for $\{24^3;840\}$ ensemble and 198 configurations for $\{24^3;860\}$ ensemble, both with $n_{\text{sep}} = 40$ trajectories. 'fwd' represents the Forward diagram and 'smt' represents the Same-Time diagram. $\Delta t = 3a_t$ in the m_{eff} plots.

extract an accurate ground energy level, the energy is not fitted here.

However, it is remarkable that the correlator is obtained after a large VEV subtraction but still gives a signal which is acceptably quiet. The Forward('fwd') diagram $C_{\text{fwd}}(t)$ again corresponds to the isovector counterpart, i.e. a_0 meson. The masses are found to be $m_{a_0} = 1.211(32)$ GeV and $m_{a_0} = 1.214(31)$ GeV on $\{24^3;840\}$ and $\{24^3;860\}$ ensembles respectively. Experimentally, $m_{a_0}^{\text{exp}} = 980(20)$ MeV.

Vector (V) Channel

Fig. 4.7 shows the result of the vector channel. Experimentally the isovector (ρ) and isoscalar (ω) vector mesons have very close masses($m_\rho^{\text{exp}} = 775.49(34)$ MeV and $m_\omega = 782.65(12)$ MeV). On the lattice they also show a similar feature. The Same-time diagram contribution $C_{\text{smt}}(t)$ is found to be very insignificant. The masses are

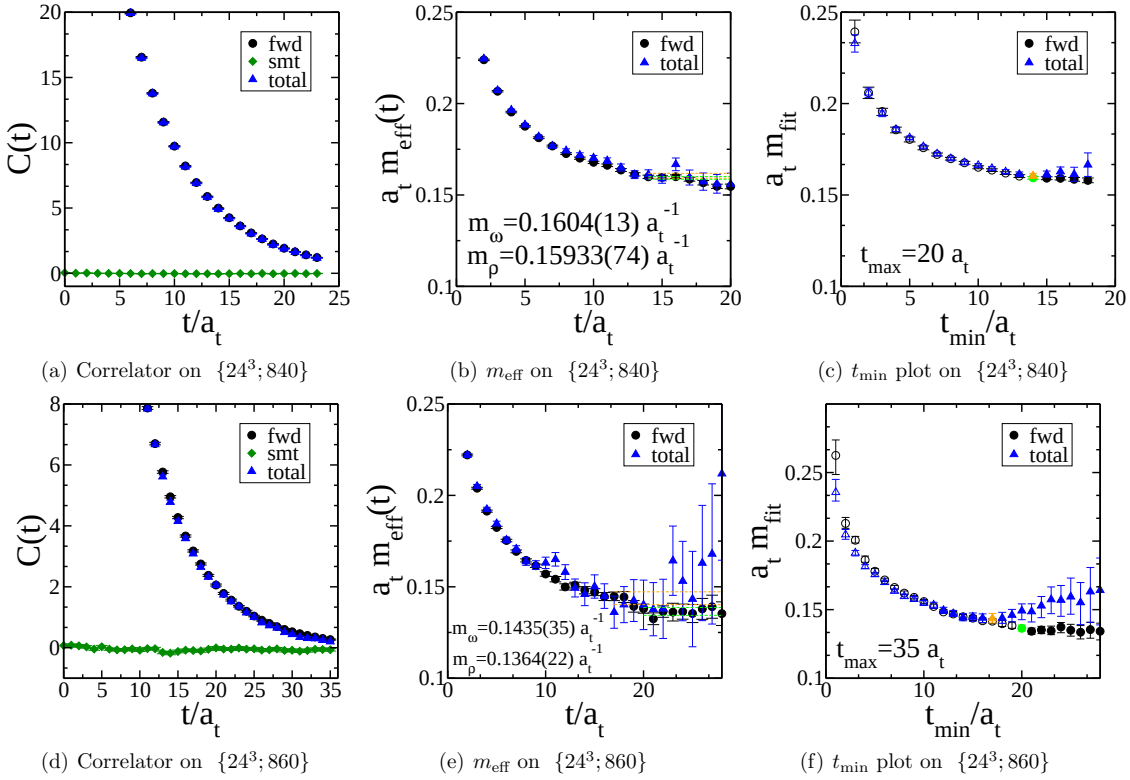

(a) Correlator on $\{24^3;840\}$ (b) m_{eff} on $\{24^3;840\}$ (c) t_{min} plot on $\{24^3;840\}$

(d) Correlator on $\{24^3;860\}$ (e) m_{eff} on $\{24^3;860\}$ (f) t_{min} plot on $\{24^3;860\}$

Figure 4.7: V channel on $\{24^3;840\}$ and $\{24^3;860\}$ ensembles. There are 210 configurations for $\{24^3;840\}$ ensemble and 198 configurations for $\{24^3;860\}$ ensemble, both with $n_{\text{sep}} = 40$ trajectories. 'fwd' represents the Forward diagram and 'smt' represents the Same-Time diagram. $\Delta t = 3a_t$ in the m_{eff} plots.

found to be $m_\rho = 902(5)$ MeV and $m_\omega = 908(8)$ MeV on the $\{24^3;840\}$ ensemble, while $m_\rho = 820(13)$ MeV and $m_\omega = 863(21)$ MeV on the $\{24^3;860\}$ ensemble.

4.4 Multi-hadrons

As previously discussed, the correlators of ρ-$\pi\pi$ system and two-pion scattering can be used as a test for multi-hadron computations. This is a preliminary examination of them on the realistic lattices. The fitting form of the correlator is different from cosh because of the interaction between a wrap-around pion and an original pion. If the pion operator is symmetric under time reversal, the correlator is in the form of

$$a_0 \cosh(E_{\text{fit}} t - N_t/2) + a_1 \tag{4.1}$$

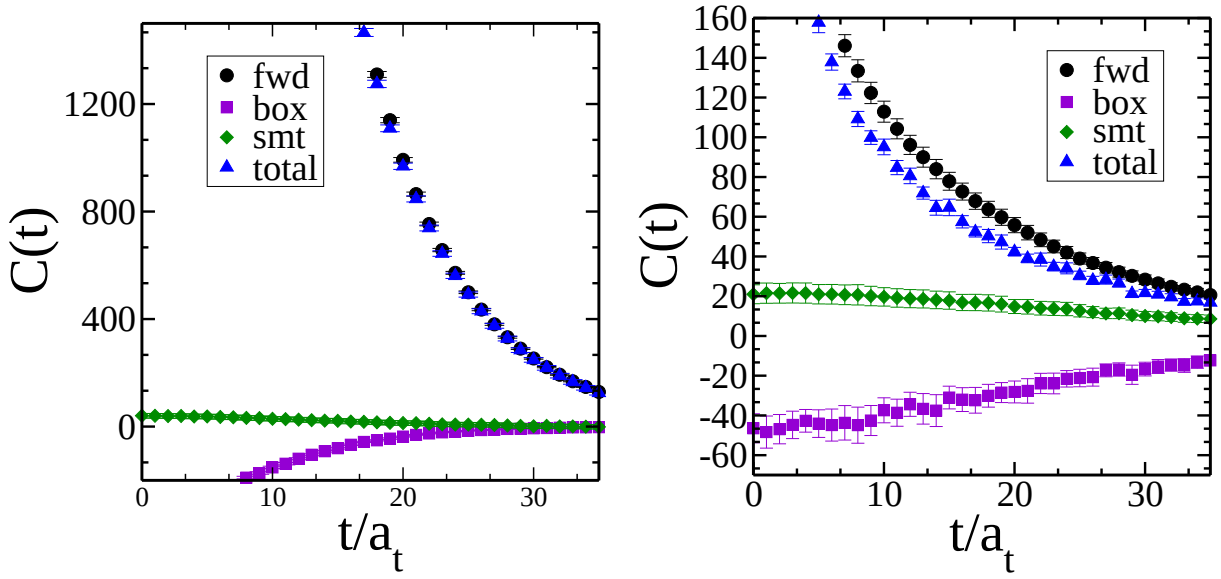

(a) Correlator on $\{24^3; 840\}$ ensemble

(b) Correlator on $\{24^3; 860\}$ ensemble

Figure 4.8: $I = 0$ channel two-pion scattering on $\{24^3; 840\}$ and $\{24^3; 860\}$ ensembles. There are 551 and 584 configurations with separation $n_{\text{sep}} = 20$ trajectories respectively.

with fitted energy E_{fit} and fitting parameters a_0 and a_1. However, the pion operators used in this section are not symmetric under time reversal, therefore the correct fit form is

$$a_0 \exp(-E_{\text{fit}} t) + a_1 \exp(-E_{\text{fit}}(N_t - t)) + a_2. \tag{4.2}$$

Since the wrap-around effect is not very significant and the main goal of this section is not to precisely calculate the energy shifts, the a_1 term is omitted. In the case of $I = 0$, it is found that a_2 term is also consistent with 0, and thus omitted.

4.4.1 $I = 0$ Channel

Fig. 4.8 shows the (VEV subtracted) correlators of the $I = 0$ channel two-pion scattering. It is found that $C_{\text{fwd}}(t)$ dominates the correlator, but the other diagrams also contribute significantly. The energy is found to be lower than the total of free non-interacting pions in Fig. 4.9, i.e. attractive. This matches the prediction from chiral perturbation theory [61].

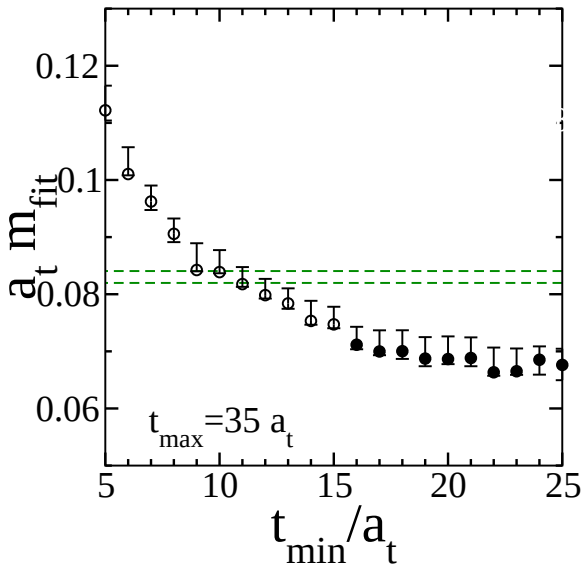

Figure 4.9: Fitted energies of $I = 0$ channel two-pion scattering on the $\{24^3; 860\}$ ensemble. There are 584 configurations with separation $n_{\text{sep}} = 20$ trajectories respectively. The range between the green lines indicate the energy of two free non-interacting pions computed from single-pion correlators. The fit form ignores the constant term because it is found to be consistent with zero.

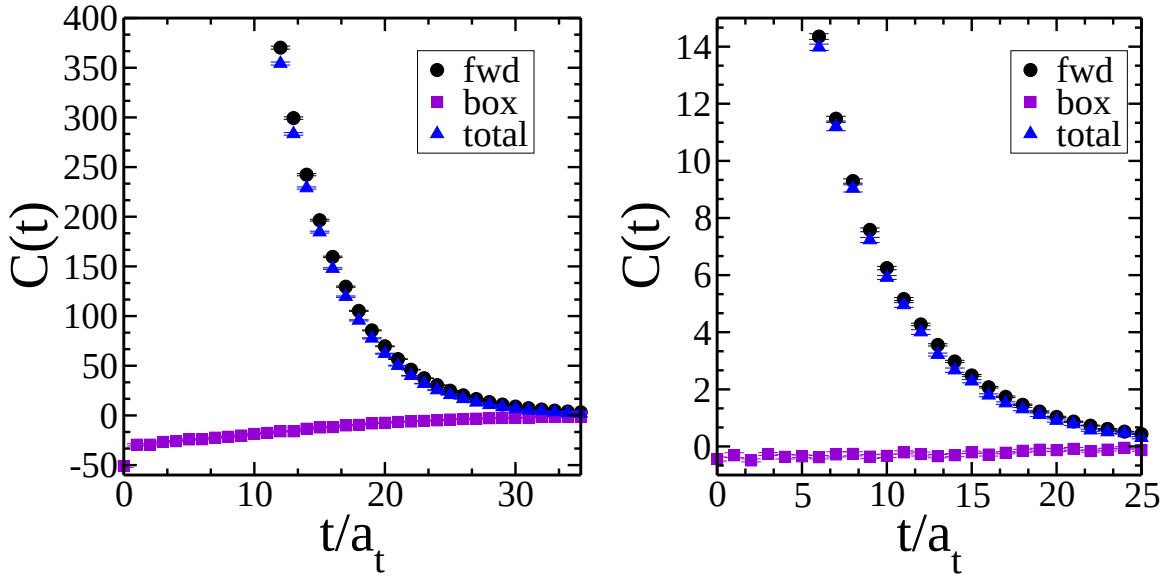

(a) Correlator on $\{24^3; 840\}$ ensemble.

(b) Correlator on $\{24^3; 860\}$ ensemble.

Figure 4.10: $\pi\pi \to \pi\pi$ $I = 1$ channel two-pion scattering on $\{24^3; 840\}$ and $\{24^3; 860\}$ ensembles. There are 551 and 584 configurations with separation $n_{\text{sep}} = 20$ trajectories respectively.

4.4.2 $I = 1$ Channel

Fig. 4.10 shows the results of $I = 1$ two-pion scattering channel averaged over the three $\hat{n}$'s in Eq. 3.47. Since it is expected that ρ meson is a lower-lying energy level, it has to be included in order to extract the ground energy level. Since the test is not to extract the energy, a fit of the energy of the two-pion scattering is not performed.

In order to mix ρ with the two-pion operators, the off-diagonal elements of the correlator matrix are necessary. Fig. 4.11 shows the quality of the corresponding signals obtained. It is observed that there is significant mixing between the ρ and $\pi\pi$ operators. After diagonalization on $\{24^3; 860\}$ ensemble, two clean levels can be obtained(Fig. 4.12). The ground level is ρ dominated and the first excited state is $\pi\pi$ dominated. It should be noted that the errors in both levels are smaller than the energy levels determined by ρ operator alone or two-pion operator alone. This shows the importance of having more than one operators to extract the energy levels. In a more serious calculation, more operators of both types have to be included to give an acceptably good signal.

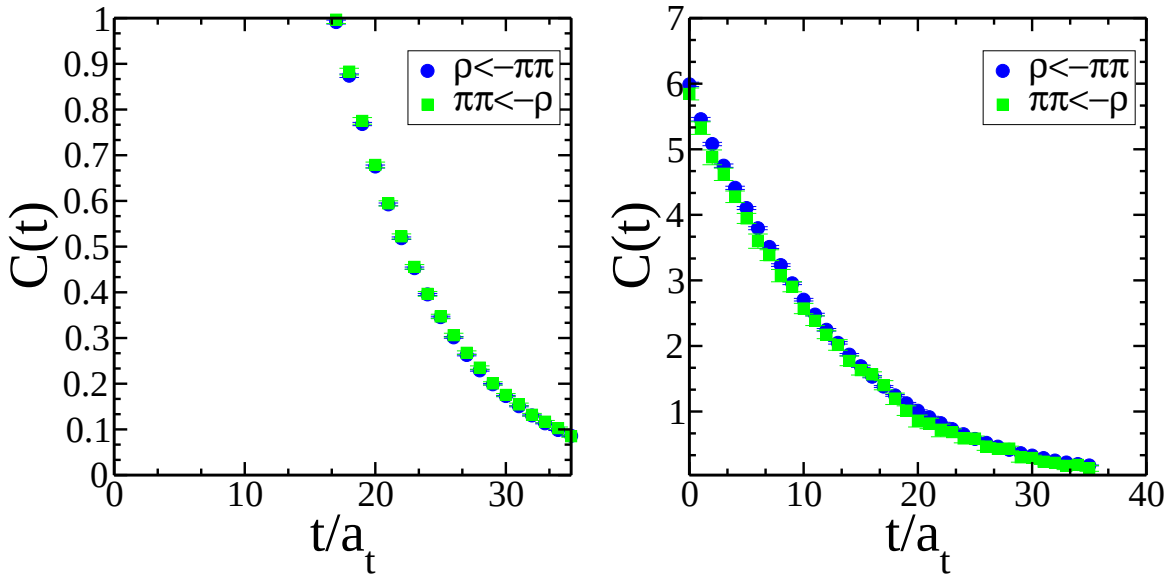

(a) Correlators on $\{24^3; 840\}$ ensemble.

(b) Correlators on $\{24^3; 860\}$ ensemble.

Figure 4.11: ρ-$\pi\pi$ Correlators on $\{24^3; 840\}$ and $\{24^3; 860\}$ ensembles. There are 551 and 584 configurations with separation $n_{\text{sep}} = 20$ trajectories respectively. The correlators are averaged over all three directions.

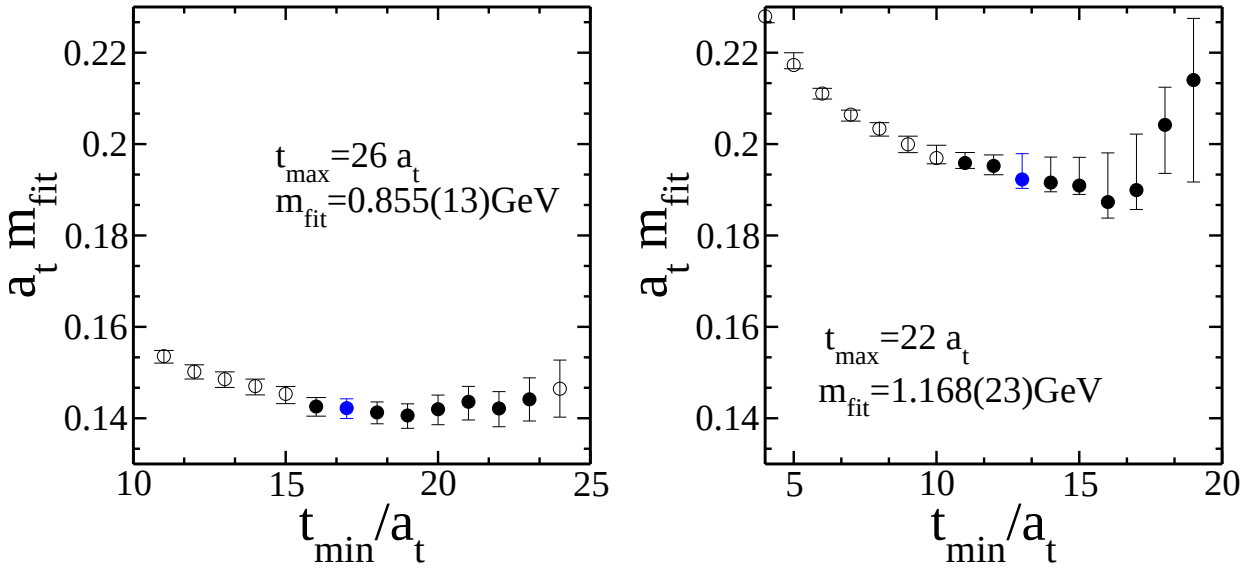

(a) Level 0

(b) Level 1

Figure 4.12: Diagonalized $I = 1$ channel on $\{24^3; 860\}$ ensembles. There are 551 and 584 configurations with separation $n_{\text{sep}} = 20$ trajectories respectively.

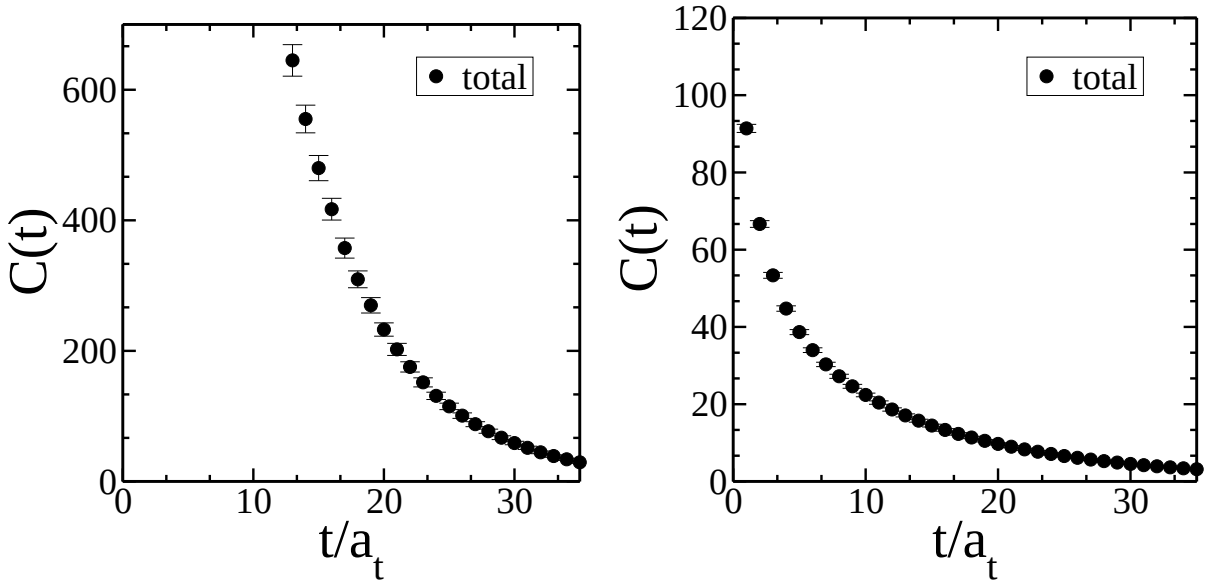

(a) Correlator on $\{24^3; 840\}$ ensemble

(b) Correlator on $\{24^3; 860\}$ ensemble

Figure 4.13: $I = 2$ channel two-pion scattering on $\{24^3; 840\}$ and $\{24^3; 860\}$ ensembles. There are 551 and 584 configurations with separation $n_{\text{sep}} = 20$ trajectories respectively.

4.4.3 $I = 2$ Channel

Fig. 4.13 shows the result of $I = 2$ channel two-pion scattering. The energy tends to be higher than the total of free non-interacting pions in Fig. 4.14, i.e. repulsive. This matches the prediction from chiral perturbation theory [61]. However, if an accurate energy shift is to be determined, the variance is clearly not small enough. This indicates that better operators have to be employed to achieve this goal.

4.5 Conclusion

In this section, the results of some first applications of the Stochastic LapH algorithm were presented. These include the simulation of simple hadrons, isoscalars and multi-hadron systems. Energies are extracted from the corresponding correlators and the accuracy is remarkably high compared with previous works. The results obtained are very promising and demonstrate the fact that the algorithm has allowed a manageable and feasible way of computing all diagrams one needs for extracting the spectrum.

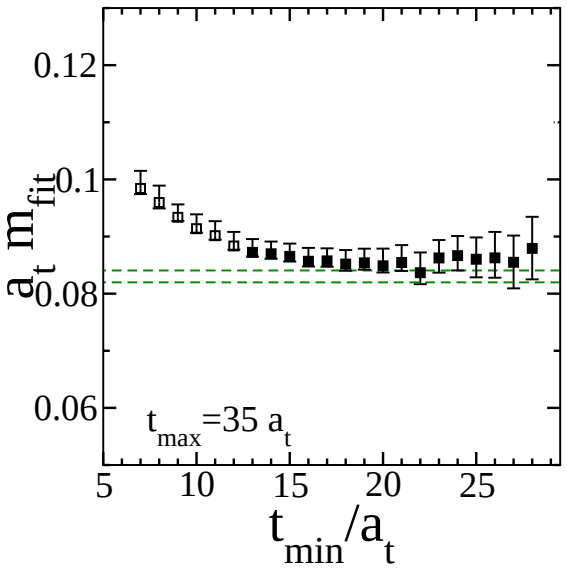

Figure 4.14: Fitted energies of $I = 2$ channel two-pion scattering on $\{24^3; 860\}$ ensemble. There are 584 configurations with separation $n_{\rm sep} = 20$ trajectories respectively.

Chapter 5

Summary and Outlook

Monte Carlo path integration with spacetime (lattice) discretization provides a powerful approach of obtaining non-perturbative predictions from QCD, the theory that successfully describes the strong interactions among quarks and gluons. Our long-term goal is to obtain the lowest-lying stationary-state energy levels of QCD in all symmetry channels. Since most of the excited states are above multi-hadron thresholds, multi-hadron operators have to be included to properly capture these states. The main problem of computing multi-hadron correlators is the inclusion of same-time quark lines which begin and end in the same sink time-slice. The evaluation of such correlator functions is exceedingly difficult with standard point-to-all methods, especially in lattices with large spatial volumes and light pion masses.

The Stochastic LapH algorithm was developed to facilitate computing excited state and multi-hadron correlations in lattice QCD. Its development began in Ref. [62] and additional needed features, mainly the crucial time dilution, were introduced in this work. It provides a very efficient way of computing quark propagators, especially the same-time quark lines. It makes use of Laplacian-Heaviside quark-field smearing and solves the large volume problems by introducing dilution-improved stochastic techniques. The LapH smearing suppresses the contamination from unwanted high-lying modes, while the stochastic approach makes use of the fact that exact inversions are unnecessary due to the dominance of intrinsic noise coming from the link variables. The dilution technique greatly reduces the variance introduced by putting in stochastic noise. We managed to find a dilution scheme that produces a variance near that of the gauge noise limit. Dilution in the LapH subspace tames the linear spatial-volume scaling behavior, while dilution in time allows computation of same-time quark lines

for many values of time without sacrificing accuracy. Two extra bonuses were obtained from this algorithm. The algorithm provides the scalar glueball operator for free. Also, it restores factorization of source and sink hadron operators in the correlators. This provides the flexibility and convenience in the computation of correlator matrices that involve many different hadron operators.

The Stochastic LapH algorithm was shown to work well in both small and large lattices, at both light and heavy pion masses. Suitable dilution schemes were found by looking at the correlators of η, ρ-$\pi\pi$ and two-pion systems (box diagram contribution) on the $\{16^3; 840\}$ ensemble. A new glueball operator was also computed to show that it is comparable to traditional smeared plaquette operators. The algorithm was then applied to larger lattices $\{24^3; 840\}$ and $\{24^3; 860\}$. The correlators of the lightest meson π and lightest baryon N were computed and the corresponding ground state energies were extracted. The energy of the Ω baryon was also extracted in order to set the scale of the lattice spacing. The correlators of isoscalar mesons, which consist of same-time diagrams, were computed. The pseudoscalar, scalar and vector channels were studied. The correlators of the two-pion system in $I = 0, 2$ channels were also computed. The $I = 1$ channel was studied together with ρ-$\pi\pi$ system. Energies were extracted from the above correlators with good accuracy.

Our results to date are very encouraging and suggest that accurate extractions of excited-state hadrons taking multi-hadron into full account will be possible. In the future, more operators and better operators will be included to further improve the results. The algorithm also provides a convenient tool for other related studies such as the determination of phase shifts in multi-hadron scatterings and decay widths of unstable hadrons.

In the near future, intensive studies will be carried out on the $\{24^3; 860\}$ and $\{32^3; 860\}$ ensembles. These include the determination of the spectra of all channels and analysis based on them. The phase shift of two-pion scattering and decay widths of ρ will also be investigated. The method is very general and will eventually be used for 3-point correlators and structure functions.

Appendix A

Construction of Hadron Operators [10, 12]

As mentioned in Ch. 3, it is very important to use well-constructed hadron operators in order to extract the hadron spectra. The hadron operators used in this work are constructed by considering the representations that obey the symmetries on a lattice, including spatial rotations, reflections, isospins and charge conjugation(G-parity) for mesons. [10, 12] Besides, one needs to consider the symmetries associated with the momentum the hadron acquires. Given a momentum p, the transformations that leave it unchanged define the little groups of p. The gauge-invariant hadron operators that transform according to the rows of the irreps of the combinations of the little groups with the groups corresponding to the other lattice symmetries are the operators used in this work.

For each irrep, there are infinitely many ways to construct the corresponding operators using the building blocks described in the main text. For simplicity, only several types of operators are used in this work and the displacement lengths are fixed to be 3. They are classified in terms of the displacements in the constituent quarks and defined in Tables A.1 and A.2. Each operator constructed in this way was labeled by this "spatial type" and an "ID" number. $d_i = 0, \pm 1, \pm 2, \pm 3$ correspond to no displacement and displaced in $\pm x$-($\pm y$-, $\pm z$-) directions. For mesons, d_0 corresponds to the displacement direction of the anti-quark, while d_1 and d_2 correspond to the directions of the displacements of the quark. For baryons, d_i corresponds to the displacement direction of quark i.

Visualization	Name(Abbreviation)	d_1	d_2	d_3
	Single-Site(SS)	0	0	0
	Singly-Displaced(SD)	0	0	k
	Doubly-Displaced-L(DDL)	i	0	k
	Triply-Displaced-U(TDU)	i	j	i
	Triply-Displaced-O(TDO)	i	j	k

Table A.1: Spatial Types of Meson Operators ($|i| \neq |j| \neq |k|$) For mesons with momenta, the spatial type SD is split into Longitudinal-Singly-Displaced(LSD) and Transverse-Singly-Displaced(TSD). The former have momenta parallel with the displacement, while the latter are the rest.

Visualization	Name(Abbreviation)	d_1	d_2	d_3
	Single-Site(SS)	0	0	0
	Singly-Displaced(SD)	0	0	k
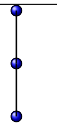	Doubly-Displaced-I(DDI)	0	k	k
	Doubly-Displaced-L(DDL)	i	0	k
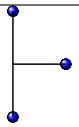	Triply-Displaced-T(TDT)	i	j	$-i$
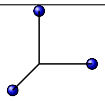	Triply-Displaced-O(TDO)	i	j	k

Table A.2: Spatial Types of Baryon Operators($|i| \neq |j| \neq |k|$) For baryons with momenta, the spatial type SD is split into Longitudinal-Singly-Displaced(LSD) and Transverse-Singly-Displaced(TSD). The former have momenta parallel with the displacement, while the latter are the rest.

Appendix B

Hadron Operator Selection

Although only several spatial types of operators are considered in this work, one can still construct a lot of possible operators. However, not all constructed operators are independent from one another. Moreover, not all operators are intrinsically quiet. It is a waste of resources to compute dependent or noisy operators. Therefore it is impractical, and also not necessary, to take all possible operators into account as long as the lowest lying energy levels in the spectra are concerned. This results in the need of constructing an optimal set of operators, or 'pruning'.

The objective of the pruning is to construct two sets of operators for each channel of each sector. The first one is used for the computation of the basic spectrum that comes from single-hadron operators. Since all rows of each irrep give statistically identical mass, only one row of each irrep is used. The second set is used to construct the multi-hadron operators to be mixed with the single-hadron ones. All rows of each irrep are used in this set. The single-hadron set is obtained before the multi-hadron one. The following sections describe the details of this process. All simulations mentioned are done in $\{16^3; 840\}$ and $\{20^3; 840\}$ ensembles in 2.4.

B.1 Operator Sets for Single-Hadron computations

The optimal set of operators to be used must satisfy the following conditions:

- The operators have to be as independent as possible. This is reflected in the condition number of the correlator matrix formed. The closer to 1 this quantity is, the more independent the operators are.

- The intrinsic noise in the operators have to be small in order to obtain a clear signal.

The actual procedures of the pruning process in each channel of each sector can be summarized as follows.

For Mesons, the procedures are straightforward:

1. Compute the correlator matrix with all available operators for all spatial types.
2. Construct the largest set of operators with acceptably small variances. This can be determined from the effective masses obtained from individual operators.
3. Construct the largest subset of operators from the previous one, keeping a good condition number.

The results are shown in Tables B.4 to B.5.

For Baryons, there are too many operators to be considered all together at the same time. Therefore the procedure is slightly more complicated:

1. Compute the correlator matrix with all available operators for each spatial type.
2. Construct the largest set of operators with acceptably small variances for each spatial type.
3. Construct the largest set of operators from the previous pre-pruned one, keeping a good condition number.

The results are shown in Tables B.6 to B.10.

B.2 Operator Sets for Multi-Hadron computations

After the pruning of operators used for single-hadron computations, one can construct the basic spectrum by diagonalizing the correlator matrices and fit the effective masses. By subduction of O_h into the little groups(Tables B.1 to B.3), one can estimate how energy levels will emerge from the O_h channels when momenta are introduced into those states. Therefore one is only interested in the energy levels below a certain energy E_{max}(in this work, $E_{\text{max}} \approx 2.5\text{G}e\text{V}$ is chosen), one can estimate how many energy levels will be relevant in each channel using the naive spectra obtained

$\Lambda(O_h)$	$\Lambda(O_h) \downarrow C_{2v}$
A_{1g}	A_1
A_{1u}	A_2
A_{2g}	B_2
A_{2u}	B_1
E_g	$A_1 \oplus B_2$
E_u	$A_2 \oplus B_1$
T_{1g}	$A_2 \oplus B_1 \oplus B_2$
T_{1u}	$A_1 \oplus B_1 \oplus B_2$
T_{2g}	$A_1 \oplus A_2 \oplus B_1$
T_{2u}	$A_1 \oplus A_2 \oplus B_2$
$G_{1g/u}$	G
$G_{1g/u}$	G
$H_{g/u}$	$2G$

Table B.1: Subduction of C_{2v}

from the single-hadron operators. Note that the maximum interested energy here refers to the total energy that ends up in the spectra. Therefore, to construct the operator sets used for multi-hadron computations, the energy cutoff for a hadron operator with momentum $\vec{p}$ has to be E_{max} subtracted by the lightest hadron with opposite momentum, i.e. π with momentum $-\vec{p}$. Therefore the operator sets for multi-hadron computations only need to have a size large enough for extracting the amount of energy levels below such energy.

Another complication comes into play for these operator sets. Baryon operators are significantly more costly to be displaced than mesons. Since there are a lot of rows and directions of momenta to be computed, the difference between the computation costs of displaced operators and those of Single-Site(SS) ones is huge. Therefore SS operators are much more preferred for these sets of baryons. To compensate for the possible adverse effect of this bias in choices, many(if not all) SS operators are generated as long as the numbers of independent operators are at least the required ones.

To conclude, there are two additional conditions for these operator sets to satisfy:

- The size has to be at least the number of required levels deduced by subduction so that the desired levels can be obtained after diagonalization of the correlator matrix.

$\Lambda(O_h)$	$\Lambda(O_h) \downarrow C_{3v}$
A_{1g}	A_1
A_{1u}	A_2
A_{2g}	A_2
A_{2u}	A_1
E_g	E
E_u	E
T_{1g}	$A_2 \oplus E$
T_{1u}	$A_1 \oplus E$
T_{2g}	$A_1 \oplus E$
T_{2u}	$A_2 \oplus E$
$G_{1g/u}$	G
$G_{1g/u}$	G
$H_{g/u}$	$F_1 \oplus F_2 \oplus G$

Table B.2: Subduction of C_{3v}

$\Lambda(O_h)$	$\Lambda(O_h) \downarrow C_{4v}$
A_{1g}	A_1
A_{1u}	A_2
A_{2g}	B_1
A_{2u}	B_2
E_g	$A_1 \oplus B_1$
E_u	$A_2 \oplus B_2$
T_{1g}	$A_2 \oplus E$
T_{1u}	$A_1 \oplus E$
T_{2g}	$B_2 \oplus E$
T_{2u}	$B_1 \oplus E$
$G_{1g/u}$	G_1
$G_{1g/u}$	G_2
$H_{g/u}$	$G_1 \oplus G_2$

Table B.3: Subduction of C_{4v}

- For Baryons, the Single-Site(SS) operators are more desirable for the multi-hadron sets due to the computational constraints described above.

The results are shown in Tables B.11 to B.17.

Table B.4: Isovector, $\bar{d}u$, Operators used in Single-Hadron computations

Group	Irrep	Spatial Type	Operator IDs
O_h	A_{1g}^+	SS	0
		DDL	3
		TDU	1, 2
		TDO	0
	A_{1g}^-	SD	2
		DDL	1
		TDO	2, 3, 6
	A_{1u}^+	SD	0
		TDU	0, 1
		TDO	0, 3
	A_{1u}^-	DDL	2
		TDO	0, 1, 5, 9
	A_{2g}^+	TDO	0, 1, 5, 7, 8, 9
	A_{2g}^-	DDL	3
		TDU	0, 2
		TDO	1, 2
	A_{2u}^+	DDL	2, 3, 5
		TDO	2, 3, 4
	A_{2u}^-	DDL	1
		TDU	1, 5
		TDO	0, 2
	E_g^+	DDL	6, 7
		TDU	7
		TDO	6, 7
	E_g^-	SD	0
		DDL	2
		TDU	1, 4, 5
		TDO	9, 15

continued in the next page

Group	Irrep	Spatial Type	Operator IDs
	E_u^+	DDL	$3, 4, 5$
		TDU	0
		TDO	5
	E_u^-	SD	$0, 1$
		DDL	5
		TDU	10
		TDO	7
	T_{1g}^+	SS	0
		DDL	$5, 7$
		TDU	0
		TDO	7
	T_{1g}^-	SS	0
		TDU	$8, 9$
		TDO	$6, 13$
	T_{1u}^+	SS	$0, 1$
		DDL	$2, 8$
		TDO	3
	T_{1u}^-	SD	1
		DDL	$0, 3$
		TDU	$2, 4$
	T_{2g}^+	DDL	$6, 7$
		TDU	$5, 9$
		TDO	$0, 7, 9$
	T_{2g}^-	DDL	$2, 7$
		TDU	$3, 5, 6, 7, 10$
		TDO	$5, 21, 24$
	T_{2u}^+	SD	$1, 2$
		TDU	$5, 7$
		TDO	$4, 5$
	T_{2u}^-	DDL	$0, 2, 11$

continued in the next page

Group	Irrep	Spatial Type	Operator IDs
		TDU	$2, 4, 8$
		TDO	$14, 25$

Table B.5: Kaon K , $\bar{s}s$, Operators used in Single-Hadron computations

Group	Irrep	Spatial Type	Operator IDs
O_h	A_{1g}	SS	1
		SD	0
		TDU	5
		TDO	$3, 8$
	A_{1u}	SS	1
		SD	$2, 3$
		TDU	0
		TDO	12
	A_{2g}	DDL	7
		TDU	$5, 6$
		TDO	$4, 6, 14$
	A_{2u}	DDL	$3, 6$
		TDO	$8, 10, 11, 12$
	E_g	SD	3
		DDL	$4, 15$
		TDU	10
		TDO	13
	E_u	SD	2
		DDL	12
		TDU	$5, 12$
		TDO	30
	T_{1g}	SS	0
		SD	5
		DDL	6
		TDU	$18, 21$
		TDO	29
	T_{1u}	SS	1
		DDL	$1, 5, 13$

continued in the next page

Group	Irrep	Spatial Type	Operator IDs
		TDO	42
	T_{2g}	DDL	$0, 22$
		TDU	18
		TDO	$1, 36, 41$
	T_{2u}	SD	$0, 1$
		DDL	13
		TDU	20
		TDO	47

Table B.6: Nucleon N, uud, Operators used in Single-Hadron computations

Group	Irrep	Spatial Type	Operator IDs
O_h	G_{1g}	SS	$0, 2$
		SD	12
		DDI	$9, 5$
		DDL	$47, 54$
		TDT	$29, 42, 45$
	G_{1u}	SS	1
		SD	$1, 18$
		DDI	$5, 16$
		DDL	$24, 33, 63$
		TDT	$10, 23, 27, 37$
	G_{2g}	SD	7
		DDI	$1, 2, 6$
		DDL	$14, 17, 54$
		TDT	$16, 23, 29, 30, 31$
	G_{2u}	SD	$2, 3$
		DDI	$5, 6$
		DDL	$35, 56, 33$
		TDT	$35, 21, 19$
	H_g	SS	0
		SD	$29, 18$
		DDI	10
		DDL	$88, 90, 100, 104$
		TDT	$94, 99, 113, 127$
	H_u	SS	0
		SD	30
		DDI	$1, 21, 26$
		DDL	$58, 68, 70$
		TDT	$58, 70$

Table B.7: Delta Δ, uud, Operators used in Single-Hadron computations. The same Operator set is used in the Single-Hadron computation for $Omega$, sss,since the mass of uud is the same as that of uuu, which is the same set of operators for sss except that a heavier quark mass is used. However it should be noted that this argument does not apply to Multi-Hadron computations due to the difference in symmetrization of the uuu(thus sss) and uud operators.

Group	Irrep	Spatial Type	Operator IDs
O_h	G_{1g}	SD	$4, 8, 9$
		DDI	$0, 1, 7$
		DDL	$8, 28, 31$
		TDT	$1, 12$
	G_{1u}	SD	$4, 8, 13$
		DDI	$6, 7$
		DDL	$10, 28, 31$
		TDT	26
	G_{2g}	SD	$0, 2, 3, 4$
		DDL	$7, 8, 21, 28$
		TDT	$10, 13, 18$
	G_{2u}	SD	$2, 3$
		DDL	$8, 11, 19, 29$
		TDT	$3, 13, 30$
	H_g	SS	0
		SD	17
		DDI	3
		DDL	$19, 44$
		TDT	$24, 25, 34$
	H_u	SS	$0, 1$
		DDI	$9, 13$
		DDL	$30, 62$
		TDT	$29, 30, 48, 52$

Table B.8: Lambda Λ, uds, Operators used in Single-Hadron computations

Group	Irrep	Spatial Type	Operator IDs
O_h	G_{1g}	DDL	3
		TDT	$5, 8, 28, 38$
		SD	21
		DDI	$6, 21, 22$
	G_{1u}	DDL	82
		TDT	$16, 20$
		SD	$21, 31$
		DDI	$10, 16$
	G_{2u}	DDL	91
		TDT	$33, 94, 95$
		DDI	$4, 7$
	G_{2g}	DDL	7
		TDT	$22, 23, 24, 59$
	H_g	DDL	$46, 120$
		TDT	$134, 158$
		DDI	$9, 17, 29, 45$
	H_u	DDL	166
		TDT	$5, 66$
		SD	23
		DDI	$16, 27$

Table B.9: Sigma Σ, uds, Operators used in Single-Hadron computations

Group	Irrep	Spatial Type	Operator IDs
O_h	G_{1g}	DDL	$55, 89$
		TDT	$77, 65, 72, 12, 19$
		SD	9
		DDI	$0, 34, 22, 12$
	G_{1u}	DDL	$34, 78$
		TDT	$4, 91$
		SD	5
		DDI	13
	G_{2g}	DDL	$36, 24, 91, 54$
		TDT	$28, 43, 29, 79$
		DDI	$11, 8, 2$
	G_{2u}	DDL	35
		TDT	$32, 33, 78$
		DDI	10
	H_u	DDL	$3, 156$
		TDT	$41, 5, 65, 184, 190$
		DDI	$15, 3, 10$
	H_g	DDL	$54, 108, 94$
		TDT	$3, 156, 135$
		SD	47
		DDI	$1, 31, 42, 29$

Table B.10: Cascade Ξ, ssu, Operators used in Single-Hadron computations

Group	Irrep	Spatial Type	Operator IDs
O_h	G_{1g}	SS	$0, 2$
		SD	6
		DDI	$0, 6, 7, 9$
		DDL	88
		TDT	$20, 65$
	G_{1u}	SS	3
		SD	$3, 30$
		DDI	$1, 20$
		DDL	34
		TDT	$9, 23, 17, 31$
	G_{2g}	SD	$0, 1, 2, 4, 5$
		DDI	0
		DDL	$26, 32, 46, 47, 55, 89$
		TDT	$42, 66, 67$
	G_{2u}	SD	$1, 2, 4, 6$
		DDI	$4, 7, 8$
		DDL	$69, 74$
		TDT	$32, 33, 44, 51, 86, 95$
	H_g	SS	$1, 2$
		DDI	$4, 6, 7, 15, 16, 18, 28, 29, 41, 44$
		DDL	$108, 174$
		TDT	2
	H_u	SS	0
		SD	3
		DDI	$3, 5, 10, 15, 16, 17, 18, 19$
		TDT	$8, 19$

Table B.11: Isovector , $\bar{d}u$, Operators used in Multi-Hadron computations

Group	Irrep	Spatial Type	Operator IDs
O_h	A_{1g}^+	TDO	0
	A_{1g}^-	SD	2
		TDO	2
	A_{1u}^+	-	-
	A_{1u}^-	TDO	$0, 1, 9$
	A_{2g}^+	-	-
	A_{2g}^-	TDO	2
	A_{2u}^+	-	-
	A_{2u}^-	TDO	2
	E_g^+	-	-
	E_g^-	TDU	4
		TDO	9
	E_u^+	TDU	0
	E_u^-	DDL	5
	T_{1g}^+	SS	0
		TDO	7
	T_{1g}^-	SS	0
		TDO	13
	T_{1u}^+	SS	$0, 1$
		DDL	8
		TDO	3
	T_{1u}^-	DDL	0
	T_{2g}^+	-	-
	T_{2g}^-	DDL	7
		TDO	$5, 24$
	T_{2u}^+	SD	$1, 2$
	T_{2u}^-	DDL	11
C_{2v}	A_1^+	SS	1

continued in the next page

Group	Irrep	Spatial Type	Operator IDs
		LSD	$0, 1$
		TSD	1
	A_1^-	LSD	$6, 7$
		TSD	$1, 2$
	A_2^+	LSD	$5, 6$
		TSD	1
	A_2^-	SS	0
		LSD	$5, 7$
		TSD	$3, 4, 5$
	B_1^+	LSD	$0, 1$
		TSD	1
	B_1^-	LSD	$4, 5$
		TSD	2
	B_2^+	LSD	$1, 2, 3, 7$
		TSD	$4, 5$
	B_2^-	LSD	$6, 7$
		TSD	1
C_{3v}	A_1^+	SS	1
		SD	$0, 2$
	A_1^-	SS	0
		SD	7
	A_2^+	SD	7
	A_2^-	SS	$0, 2$
	E^+	SS	0
		SD	$6, 8, 12$
	E^-	SS	0
		SD	$7, 11, 13$
C_{4v}	A_1^+	LSD	$1, 3$
		TSD	$1, 2$
	A_1^-	LSD	$0, 3$

continued in the next page

Group	Irrep	Spatial Type	Operator IDs
		TSD	1
	A_2^+	LSD	$0, 1$
	A_2^-	SS	0
		TSD	$0, 2, 3, 4, 5$
	B_1^+	TSD	3
	B_1^-	TSD	$1, 2, 3$
	B_2^+	TSD	$0, 1$
	B_2^-	TSD	$1, 2$
	E^+	SS	$0, 2$
		TSD	$3, 6, 7$
	E^-	LSD	$0, 1, 3$
		TSD	1

Table B.12: Kaon K, $\bar{s}s$, Operators used in Multi-Hadron computations

Group	Irrep	Spatial Type	Operator IDs
O_h	A_{1g}	SS	1
		SD	0
		TDO	3
	A_{1u}	SS	1
		TDU	0
	A_{2g}	DDL	7
	A_{2u}	TDO	10
	E_g	SD	3
	E_u	SD	2
		TDU	5
	T_{1g}	SS	0
		SD	5
		DDL	6
		TDO	29
	T_{1u}	SS	1
		DDL	5, 13
		TDO	42
	T_{2g}	TDO	36, 41
	T_{2u}	DDL	13
		TDU	20
		TDO	47
C_{2v}	A_1	SS	1, 2, 3
		LSD	0, 9
		TSD	6
	A_2	SS	0, 1, 2
		LSD	6, 13
		TSD	6
	B_1	LSD	6, 9, 11, 14, 15

continued in the next page

Group	Irrep	Spatial Type	Operator IDs
		LSD	4
	B_2	SS	$0, 1, 2, 3$
		TSD	$6, 7$
C_{3v}	A_1	SS	$0, 1, 2, 3$
	A_2	SS	$0, 1$
		SD	$8, 14$
	E	SS	$0, 1$
		SD	$3, 10, 15, 18, 24$
C_{4v}	A_1	SS	$0, 3$
		TSD	$1, 2$
	A_2	SS	$1, 2$
		LSD	$1, 7$
		TSD	$0, 3$
	B_1	TSD	$4, 6, 7$
	B_2	TSD	$2, 4, 6, 7$
	E	SS	$0, 3$
		LSD	$2, 4, 5$
		TSD	$7, 8$

Table B.13: Nucleon N, uud, Operators used in Multi-Hadron computations

Group	Irrep	Spatial Type	Operator IDs
O_h	G_{1g}	SS	$0, 1, 2$
	G_{1u}	SS	$0, 1, 2$
	G_{2g}	SD	7
	G_{2u}	SD	3
	H_g	SS	0
		SD	$18, 29$
	H_u	SS	0
		SD	$30, 31$
C_{2v}	G	SS	$0, 1, 2, 3, 4, 5, 6, 7, 8, 9$
C_{3v}	F_1	SS	$0, 1$
	F_2	SS	$0, 1$
	G	SS	$0, 1, 2, 3, 4, 5, 6, 7$
C_{4v}	G_1	SS	$0, 1, 2, 3, 4, 5, 6, 7$
	G_2	SS	$0, 1$
		LSD	$3, 7$

Table B.14: Delta Δ, uud, Operators used in Multi-Hadron computations

Group	Irrep	Spatial Type	Operator IDs
O_h	G_{1g}	SS	0
		SD	8
	G_{1u}	SS	0
		SD	13
	G_{2u}	SD	2
	G_{2g}	SD	$0, 3, 4$
	H_g	SS	$0, 1$
		SD	$11, 13, 15, 17$
	H_u	SS	$0, 1$
C_{4v}	G_1	SS	$0, 1, 2, 3, 4, 5$
	G_2	SS	$0, 1, 2, 3$
C_{2v}	G	SS	$0, 1, 2, 3, 4, 5, 6, 7, 8, 9$
C_{3v}	F_1	SS	$0, 1, 2, 3$
	F_2	SS	$0, 1, 2, 3$
	G	SS	$0, 1, 2, 3, 4, 5$

Table B.15: Lambda Λ, *uds*, Operators used in Multi-Hadron computations

Group	Irrep	Spatial Type	Operator IDs
O_h	G_{1g}	SS	$0, 1, 2, 3$
	G_{1u}	SS	$0, 1, 2, 3$
	G_{2g}	SD	$3, 8$
	G_{2u}	SD	9
	H_g	SS	0
		SD	$29, 30, 42$
	H_u	SS	0
		SD	$37, 38, 43$
C_{2v}	G	SS	$0, 1, 2, 3, 4, 5, 6, 7, 8, 9, 10, 11$
C_{3v}	F_1	SS	$0, 1$
	F_2	SS	$0, 1$
	G	SS	$0, 1, 2, 3, 4, 5, 6, 7, 8, 9$
C_{4v}	G_1	SS	$0, 1, 2, 3, 4, 5, 6, 7, 8, 9$
	G_2	SS	$0, 1$
		LSD	$1, 3, 7, 9$

Table B.16: Sigma Σ, *uds*, Operators used in Multi-Hadron computations

Group	Irrep	Spatial Type	Operator IDs
O_h	G_{1g}	SS	$0, 1, 2, 3$
	G_{1u}	SS	$0, 1, 2, 3$
	G_{2g}	SD	12
	G_{2u}	SD	8
	H_g	SS	$0, 1, 2$
		SD	35
	H_u	SS	$0, 1, 2$
		SD	44
C_{2v}	G	SS	$0, 1, 2, 3, 4, 5, 6, 7, 8, 9, 10, 11, 12, 13, 14, 15, 16, 17, 18, 19$
C_{3v}	F_1	SS	$0, 1, 2, 3, 4, 5$
	F_2	SS	$0, 1, 2, 3, 4, 5$
	G	SS	$0, 1, 2, 3, 4, 5, 6, 7, 8, 9, 10, 11, 12, 13$
C_{4v}	G_1	SS	$0, 1, 2, 3, 4, 5, 6, 7, 8, 9, 10, 11, 12, 13$
	G_2	SS	$0, 1, 2, 3, 4, 5$

Table B.17: Cascade Ξ, ssu, Operators used in Multi-Hadron computations

Group	Irrep	Spatial Type	Operator IDs
O_h	G_{1g}	SS	$0, 1, 2, 3$
	H_g	SS	$0, 1, 2$
	G_{1u}	SS	$0, 1, 2, 3$
	H_u	SS	$0, 1, 2$
	G_{2u}	SD	2
C_{2v}	G	SS	$0, 1, 2, 3, 4, 5, 6, 7, 8, 9, 10, 11, 12, 13, 14, 15, 16, 17, 18, 19$
C_{3v}	F_1	SS	$0, 1, 2, 3, 4, 5$
	F_2	SS	$0, 1, 2, 3, 4, 5$
	G	SS	$0, 1, 2, 3, 4, 5, 6, 7, 8, 9, 10, 11, 12, 13$
C_{4v}	G_1	SS	$0, 1, 2, 3, 4, 5, 6, 7, 8, 9, 10, 11, 12, 13$
	G_2	SS	$0, 1, 2, 3, 4, 5$

Bibliography

[1] S. Bethke, "The 2009 world average of α_s", *The European Physical Journal C - Particles and Fields* **64** (2009) 689–703. 10.1140/epjc/s10052-009-1173-1.

[2] M. Luscher and U. Wolff, "How to Calculate the Elastic Scattering Matrix in Two-Dimensional Quantum Field Theories by Numerical Simulation", *Nucl.Phys.* **B339** (1990) 222–252.

[3] B. S. DeWitt, "Transition from discrete to continuous spectra", *Phys.Rev.* **103** (1956) 1565–1571.

[4] K. Rummukainen and S. A. Gottlieb, "Resonance scattering phase shifts on a nonrest frame lattice", *Nucl.Phys.* **B450** (1995) 397–436, `arXiv:9503028 [hep-lat]`.

[5] **Hadron Spectrum** Collaboration, M. Peardon, J. Bulava, J. Foley, C. Morningstar, J. Dudek, R. G. Edwards, B. Joó, H.-W. Lin, D. G. Richards, and K. J. Juge, "Novel quark-field creation operator construction for hadronic physics in lattice QCD", *Phys. Rev. D* **80** no. 5, (Sep, 2009) 054506, `arXiv:0905.2160 [hep-lat]`.

[6] J. Foley, K. J. Juge, A. . Cais, M. Peardon, S. M. Ryan, and J.-I. Skullerud, "Practical all-to-all propagators for lattice QCD", *Computer Physics Communications* **172** no. 3, (2005) 145 – 162.

[7] V. Crede and C. Meyer, "The Experimental Status of Glueballs", *Prog.Part.Nucl.Phys.* **63** (2009) 74–116, `arXiv:0812.0600 [hep-ex]`.

[8] D. S. Carman, "Experimental status of exotic mesons and the GlueX experiment", *J.Phys.Conf.Ser.* **69** (2007) 012011, `arXiv:0612027 [hep-ex]`.

[9] S. Weinberg, "The U(1) Problem", *Phys.Rev.* **D11** (1975) 3583–3593.

[10] C. Morningstar, J. Bulava, J. Foley, K. J. Juge, D. Lenkner, *et al.*, "Improved stochastic estimation of quark propagation with Laplacian Heaviside smearing in lattice QCD", *Phys.Rev.* **D83** (2011) 114505, arXiv:1104.3870 [hep-lat].

[11] J. Foley, C. H. Wong, J. Bulava, K. J. Juge, D. Lenkner, *et al.*, "A novel method for evaluating correlation functions in lattice hadron spectroscopy", *PoS* **LATTICE2010** (2010) 098, arXiv:1011.0481 [hep-lat].

[12] S. Basak, R. Edwards, G. T. Fleming, U. Heller, C. Morningstar, *et al.*, "Group-theoretical construction of extended baryon operators in lattice QCD", *Phys.Rev.* **D72** (2005) 094506, arXiv:0506029 [hep-lat].

[13] **Lattice Hadron Physics (LHPC)** Collaboration, S. Basak *et al.*, "Clebsch-Gordan construction of lattice interpolating fields for excited baryons", *Phys.Rev.* **D72** (2005) 074501, arXiv:0508018 [hep-lat].

[14] S. Basak, R. Edwards, G. Fleming, K. Juge, A. Lichtl, *et al.*, "Lattice QCD determination of patterns of excited baryon states", *Phys.Rev.* **D76** (2007) 074504, arXiv:0709.0008 [hep-lat].

[15] **Hadron Spectrum** Collaboration, H.-W. Lin *et al.*, "First results from 2+1 dynamical quark flavors on an anisotropic lattice: Light-hadron spectroscopy and setting the strange-quark mass", *Phys.Rev.* **D79** (2009) 034502, arXiv:0810.3588 [hep-lat].

[16] J. M. Bulava, R. G. Edwards, E. Engelson, J. Foley, B. Joo, *et al.*, "Excited State Nucleon Spectrum with Two Flavors of Dynamical Fermions", *Phys.Rev.* **D79** (2009) 034505, arXiv:0901.0027 [hep-lat].

[17] J. Bulava, R. Edwards, E. Engelson, B. Joo, H.-W. Lin, *et al.*, "Nucleon, Δ and Ω excited states in $N_f = 2 + 1$ lattice QCD", *Phys.Rev.* **D82** (2010) 014507, arXiv:1004.5072 [hep-lat].

[18] C. Morningstar, A. Bell, C. Chen, D. Lenkner, C. Wong, *et al.*, "The excited hadron spectrum in lattice QCD using a new variance reduction method", *PoS* **ICHEP2010** (2010) 369, arXiv:1011.6573 [hep-lat].

[19] **Hadron Spectrum** Collaboration, J. Bulava *et al.*, "Phase Shift with LapH Propagators", *PoS* **LATTICE2010** (2010) 110, arXiv:1011.5277 [hep-lat].

[20] C. Morningstar, A. Bell, J. Bulava, J. Foley, K. Juge, *et al.*, "Excited-State Hadrons using the Stochastic LapH Method", *AIP Conf.Proc.* **1354** (2011) 97–103, arXiv:1101.5398 [hep-lat].

[21] C. Morningstar, A. Bell, J. Bulava, J. Foley, K. Juge, *et al.*, "Progress Report on Computing Excited-State Hadron Masses in Lattice QCD", arXiv:1103.2783 [hep-lat].

[22] K. G. Wilson, "Confinement of quarks", *Phys. Rev. D* **10** no. 8, (Oct, 1974) 2445–2459.

[23] N. Metropolis, A. Rosenbluth, M. Rosenbluth, A. Teller, and E. Teller, "Equation of State Calculations by Fast Computing Machines", *J. Chem. Phys.* **21** (1953) 1087.

[24] W. Hastings, "Monte Carlo sampling methods using Markov chains and their applications", *Biometrika* (1970) 97–109.

[25] A. Markov, "Extension of the Limit Theorems of Probability Theory to a Sum of Variables Connected in a Chain", in *Dynamic Probabilistic Systems (Volume I: Markov Models)*, R. Howard, ed., ch. Appendix B, pp. 552–577. John Wiley & Sons, Inc., New York City, 1971.

[26] M. Clark, "The Rational Hybrid Monte Carlo Algorithm", *PoS* **LAT2006** (2006) 004, arXiv:0610048 [hep-lat].

[27] S. Duane, A. D. Kennedy, B. J. Pendleton, and D. Roweth, "Hybrid Monte Carlo", *Phys. Lett.* **B195** (1987) 216–222.

[28] I. Montvay and G. Munster, *Quantum Fields on a Lattice*. Cambridge University Press,Cambridge, 1994.

[29] H. B. Nielsen and M. Ninomiya, "No Go Theorem for Regularizing Chiral Fermions", *Phys.Lett.* **B105** (1981) 219.

[30] K. Symanzik, "Continuum Limit and Improved Action in Lattice Theories. 1. Principles and ϕ^4 Theory", *Nucl.Phys.* **B226** (1983) 187.

[31] C. Morningstar and M. J. Peardon, "Analytic smearing of SU(3) link variables in lattice QCD", *Phys.Rev.* **D69** (2004) 054501, arXiv:0311018 [hep-lat].

[32] G. Lepage and P. B. Mackenzie, "On the viability of lattice perturbation theory", *Phys.Rev.* **D48** (1993) 2250–2264, arXiv:9209022 [hep-lat].

[33] C. J. Morningstar and M. J. Peardon, "The Glueball spectrum from an anisotropic lattice study", *Phys.Rev.* **D60** (1999) 034509, arXiv:9901004 [hep-lat].

[34] K. G. Wilson, *New Phenomena in Subnuclear Physics.* A. Zichichi, Plenum Press, New York, 1977.

[35] J. B. Kogut and L. Susskind, "Hamiltonian Formulation of Wilson's Lattice Gauge Theories", *Phys.Rev.* **D11** (1975) 395.

[36] L. Susskind, "Lattice Fermions", *Phys.Rev.* **D16** (1977) 3031–3039.

[37] H. Sharatchandra, H. Thun, and P. Weisz, "Susskind Fermions on a Euclidean Lattice", *Nucl.Phys.* **B192** (1981) 205.

[38] D. B. Kaplan, "A Method for simulating chiral fermions on the lattice", *Phys.Lett.* **B288** (1992) 342–347, arXiv:9206013 [hep-lat].

[39] V. Furman and Y. Shamir, "Axial symmetries in lattice QCD with Kaplan fermions", *Nucl.Phys.* **B439** (1995) 54–78, arXiv:9405004 [hep-lat].

[40] H. Neuberger, "Exactly massless quarks on the lattice", *Phys.Lett.* **B417** (1998) 141–144, arXiv:9707022 [hep-lat].

[41] H. Neuberger, "More about exactly massless quarks on the lattice", *Phys.Lett.* **B427** (1998) 353–355, arXiv:9801031 [hep-lat].

[42] M. Hasenbusch and K. Jansen, "Speeding up lattice QCD simulations with clover improved Wilson fermions", *Nucl.Phys.* **B659** (2003) 299–320, arXiv:0211042 [hep-lat].

[43] R. G. Edwards, B. Joo, and H.-W. Lin, "Tuning for Three-flavors of Anisotropic Clover Fermions with Stout-link Smearing", *Phys.Rev.* **D78** (2008) 054501, arXiv:0803.3960 [hep-lat].

[44] C. Morningstar, "The Monte Carlo method in quantum field theory", arXiv:0702020 [hep-lat].

[45] M. Hasenbusch, "HMC algorithm for two-flavour lattice QCD: Schwarz-preconditioning with a one-dimensional domain decomposition", *PoS* **LAT2007** (2007) 033, arXiv:0710.0066 [hep-lat].

[46] C. Urbach, K. Jansen, A. Shindler, and U. Wenger, "HMC algorithm with multiple time scale integration and mass preconditioning", *Comput.Phys.Commun.* **174** (2006) 87–98, arXiv:0506011 [hep-lat].

[47] A. Stathopoulos and K. Orginos, "Computing and deflating eigenvalues while solving multiple right hand side linear systems in quantum chromodynamics", arXiv:0707.0131 [hep-lat].

[48] E. Y. Remez, "Sur la détermination des polynômes d'approximation de degré donnée ", *Comm. Soc. Math. Kharkov* **10** (1934) 41.

[49] I. P. Omelyan, I. M. Mryglod, and R. Folk, "Symplectic analytically integrable decomposition algorithms: classification, derivation, and application to molecular dynamics, quantum and celestial mechanics simulations", *Computer Physics Communications* **151** no. 3, (2003) 272 – 314.

[50] M. Luscher, R. Narayanan, P. Weisz, and U. Wolff, "The Schrodinger functional: A Renormalizable probe for nonAbelian gauge theories", *Nucl.Phys.* **B384** (1992) 168–228, arXiv:9207009 [hep-lat].

[51] B. Efron, *The Jackknife, the Bootstrap, and Other Resampling Plans (CBMS-NSF Regional Conference Series in Applied Mathematics).* Society for Industrial Mathematics, Jan., 1987.

[52] H. Flyvbjerg and H. G. Petersen, "Error estimates on averages of correlated data", *J. Chem. Phys.* **91** (1969) 461.

[53] D. Lenkner ,unpublished.

[54] R. G. Edwards and B. Joo, "The Chroma Software System for Lattice QCD", *Nuclear Physics B (Proc. Suppl.)* **140** (2005) 832–834.

[55] K. Wu and H. Simon, "Thick-Restart Lanczos Method for Large Symmetric Eigenvalue Problems",
SIAM Journal on Matrix Analysis and Applications **22** no. 2, (2000) 602–616. `http://link.aip.org/link/?SML/22/602/1`.

[56] H. Rutishauser, *Description of Algol 60: Handbook for Automatic Computation*. Springer Verlag, 1967.

[57] K. Wu and H. Simon, "Dynamic Restarting Schemes for Eigenvalue Problems", *Lawrence Berkeley National Laboratory Technical Report LBNL-42982* (1999) .

[58] M. Luscher, "Topology, the Wilson flow and the HMC algorithm", *PoS* **LATTICE2010** (2010) 015, `arXiv:1009.5877 [hep-lat]`.

[59] R. Brower, S. Chandrasekharan, J. W. Negele, and U. Wiese, "QCD at fixed topology", *Phys.Lett.* **B560** (2003) 64–74, `arXiv:0302005 [hep-lat]`.

[60] **CP-PACS** Collaboration, S. Aoki *et al.*, "Lattice QCD Calculation of the ρ Meson Decay Width", *Phys.Rev.* **D76** (2007) 094506, `arXiv:0708.3705 [hep-lat]`.

[61] G. R. Allcock and A. N. Kamal, "The S Wave Pion-Pion Interaction", *Proceedings of the Physical Society* **77** no. 2, (1961) 278.

[62] J. Bulava, "An Improved Variance Reduction Technique for Stochastic All-to-All Quark Propagators in Lattice QCD Spectrum Computations",. Ph. D Thesis, Carnegie Mellon University, Pittsburgh, PA, proQuest ID 1894144241.